2

MASTER

GJBX-169 '79

SCIENCE APPLICATIONS, INC.

DISTRIBUTION OF THIS DOCUMENT IS UNLIMITED

DISCLAIMER

This report was prepared as an account of work sponsored by an agency of the United States Government. Neither the United States Government nor any agency Thereof, nor any of their employees, makes any warranty, express or implied, or assumes any legal liability or responsibility for the accuracy, completeness, or usefulness of any information, apparatus, product, or process disclosed, or represents that its use would not infringe privately owned rights. Reference herein to any specific commercial product, process, or service by trade name, trademark, manufacturer, or otherwise does not necessarily constitute or imply its endorsement, recommendation, or favoring by the United States Government or any agency thereof. The views and opinions of authors expressed herein do not necessarily state or reflect those of the United States Government or any agency thereof.

DISCLAIMER

Portions of this document may be illegible in electronic image products. Images are produced from the best available original document.

SAI-78-997-LJ
Vol. 3

ANALYSIS OF AIRBORNE RADIOMETRIC DATA
VOLUME 3
TOPICAL REPORTS

DISCLAIMER

This book was prepared as an account of work sponsored by an agency of the United States Government. Neither the United States Government nor, any agency thereof, nor any of their employees, makes any warranty, express or implied, or assumes any legal liability or responsibility for the accuracy, completeness, or usefulness of any information, apparatus, product, or process disclosed, or represents that its use would not infringe privately owned rights. Reference herein to any specific commercial product, process, or service by trade name, trademark, manufacturer, or otherwise, does not necessarily constitute or imply its endorsement, recommendation, or favoring by the United States Government or any agency thereof. The views and opinions of authors expressed herein do not necessarily state or reflect those of the United States Government or any agency thereof.

Prepared for:

U. S. Energy Research and Development Administration
Grand Junction, Colorado 81501

By:

J. H. Reed
D. C. Shreve
M. Sperling
W. A. Woolson

Science Applications, Inc.
P. O. Box 2351
La Jolla, California 92037

Work performed, in part, under
Bendix Field Engineering Corporation, Grand Junction Operations
Subcontract No. 77-041-L

SCIENCE APPLICATIONS, LA JOLLA, CALIFORNIA
ALBUQUERQUE • ANN ARBOR • ARLINGTON • ATLANTA • BOSTON • CHICAGO • HUNTSVILLE
LOS ANGELES • McLEAN • PALO ALTO • SANTA BARBARA • SUNNYVALE • TUCSON

P.O. Box 2351, 1200 Prospect Street, La Jolla, California 92037

DISTRIBUTION OF THIS DOCUMENT IS UNLIMITED

"This report was prepared as an account of work sponsored in part by the United States Government. Neither the United States nor the United States Department of Energy, nor any of their employees, nor any of the contractors, subcontractors, or their employees, makes any warranty, express or implied, or assumes any legal liability or responsibility for the accuracy, completeness, or usefulness of any information, apparatus product or process disclosed, or represents that its use would not infringe privately owned rights."

PREFACE

This third volume of the report "Analysis of Airborne Radiometric Data" consists of four topical reports generated during the performance of subcontract 77-041-L. These reports cover a general discussion of the philosophy of unfolding spectra with continuum and discrete components, a mathematical treatment of the effects of various physical parameters on the uncollided gamma-ray spectrum at aircraft elevations, a discussion of the application of the unfolding code MAZNAI to airborne data, and a discussion of the effects of the nonlinear relationship between energy deposited and pulse height in NaI(Tl) detectors.

THIS PAGE

WAS INTENTIONALLY

LEFT BLANK

TABLE OF CONTENTS

THIS PAGE

WAS INTENTIONALLY

LEFT BLANK

UNFOLDING OF SPECTRA WITH CONTINUUM AND DISCRETE COMPONENTS

Presented at

American Nuclear Society
Topical Conference

Computers in Activation
Analysis and Gamma-
Ray Spectroscopy

Mayagues, Puerto Rico

By

M. Sperling

May, 1978

THIS PAGE
WAS INTENTIONALLY
LEFT BLANK

ABSTRACT

The purpose of unfolding is to determine the existence of discrete spectral compoments, their energies and intensities, as well as the shape and intensity of the spectral continuum. Codes implementing these and related ancillary processes share joint needs for vector algebra and scaler, vector, and matrix I/O, storage, and graphic display, and possess an interrelated description vocabulary. DELPHI is an interactive English language command system which maintains basic data structures and alters them by activating sequences of basic utilities. MAZNAI is a gamma-ray spectral unfolding code for NaI data with discrete and continuum componennts, with extremely powerful peak recognition and resolution enhancement capabilities. MAZAS is a high speed line-strength estimation code for NaI data with pre-determined line energies.

THIS PAGE
WAS INTENTIONALLY
LEFT BLANK

1.1 INTRODUCTION

The receptor system consisting of a radiation source and spectrometer communicating into an unfolding processor, produces a flow of information that can be diagrammed as in Figure 1. The object spectrum, or energy distribution of radiation from the source, can be continuous, discrete, or mixed. It is viewed by the spectrometer, which produces a multi-channel data vector. This observed data has passed through a complex detection process and suffers from loss of energy resolution, from particle recoil effects, and from noise due to statistical fluctuations in the discrete counting process. The function of the unfolding processor is to minimize the effects of spectrometer response and counting fluctuations, constructing from the data an image spectrum that corresponds as closely as possible to the true object.

Spectrometers are usually linear in thier behavior. They produce expected data sets related to object spectra by an integral equation of the form

$$D_i = N \int K(E_+,E_-) \, \bar{\phi} \, (E) \; dE; \qquad (1)$$

where

$$E_+ = \tfrac{1}{2}(E_i + E)$$

is the average of the incident particle energy, E, and the energy deposited in the spectrometer when an event is detected in its i-th channel, E_i; where

$$E_- = E_i - E$$

is the difference between these two energies; where $K(E_+,E_-)$, the spectrometer response, is the probability of a count being detected in the i-th channel when a quantum of radiation is incident on

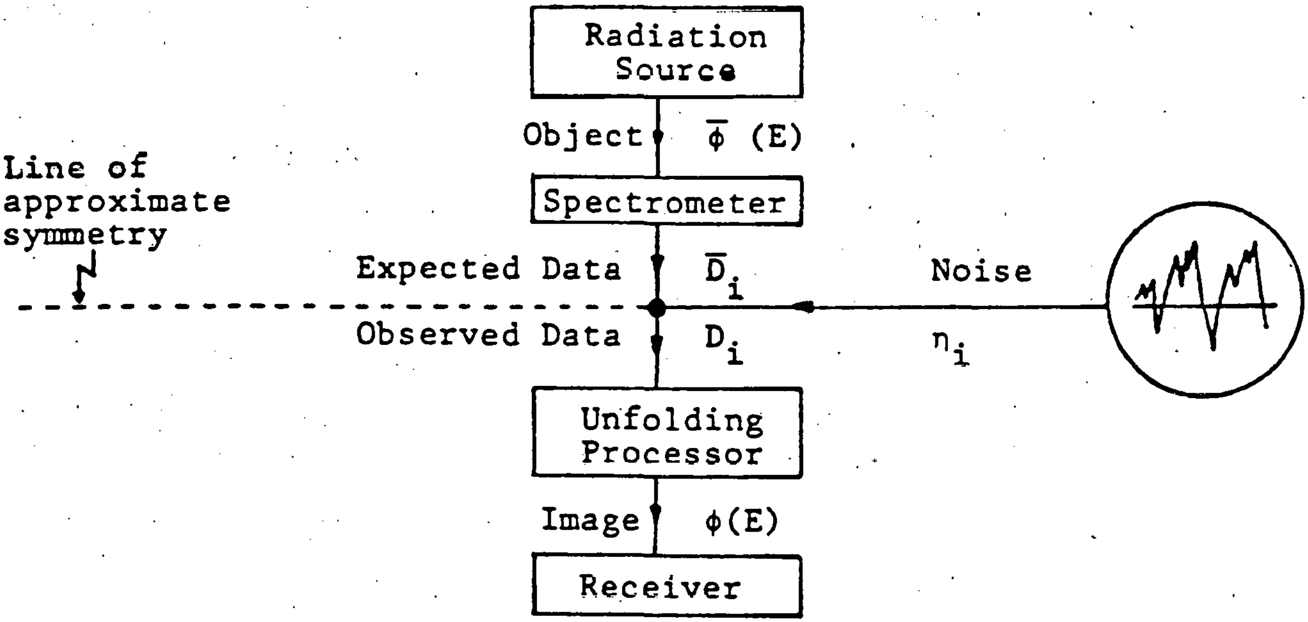
Radiation Source
Object
$\overline{\phi}$ (E)
Spectrometer
Line of approximate symmetry
Expected Data
$\overline{D}_i$
Noise
Observed Data
D_i
n_i
Unfolding Processor
Image
ϕ(E)
Receiver

Figure 1.

the spectrometer; and where N is the total number of events detectable over the full range of deposition energies, from zero to infinity. Generally the dependence of K on E_+ is slow, so that over a sufficiently narrow energy interval, K may be approximated as dependent on E_- alone. In this case, the integral relating object and data becomes a convolution integral, the so-called folding integral. The German name for convolution, "faltung", is the origin of the terms "folding" and "unfolding".

The conceptualization of unfolding as a process of deconvolution is in error in two regards: first, as we have already seen, the folding integral has a dependence on E_+, and is therefore not a convolution in the strictest sense. Second, the introduction of noise into the sequence of information flow makes the sequence irreversible, destroying perfect symmetry between the spectrometer and the unfolding processor, separating the values of the expected and the observed data and making the image spectrum only an estimate of the object. Consequently, the most accurate inverse of the folding integral does not compute the most accurate unfolded spectrum.

1.2 DELPHI: AN ENGLISH LANGUAGE INTERACTIVE COMMAND AND UTILITY SYSTEM FOR SPECTRAL UNFOLDING

Whatever the method of unfolding, its purpose is to determine the existence of discrete spectral components, their energies and intensities, as well as the shape and intensity of the spectral continuum. Codes implementing the requisite active and ancillary processes such as data reduction, data and response simulation, and response construction, share joint needs for vector algebra and scalar, vector, and matrix I/O, storage, and graphic display, and posses an interrelated descriptive vocabulary. From the user's viewpoint, this type of software is most efficient when integrated into a single interactive system from which common use can be made of algebraic, I/O and display utilities commanded in the operator's native language.

The nature of an interactive unfolding system is illustrated in Figure 2. "State" refers to stored data in many forms: for example, in memory buffers, in peripheral devices, as CRT displays and hard copy. Commands initiate alterations in this data, either by transmission as when data is read from a peripheral device into random access memory, or by active transformations such as response generation or unfolding. Computations specified in this manner are chained into a temporal sequence, although when commands are queued properly by the operating system, there need be no pause in execution. The function of DELPHI is to interpret commands stated in a subset of English, to maintain data structures appropriate for unfolding, and to activate sequences of basic operations or utilities necessary for satisfying recognized commands.

At the present time, DELPHI is implemented in FORTRAN on a DEC-10 computer. Operator interaction is by means of a Tektronix graphics terminal, primarily a Tektronix 4006. However, modular architecture has been utilized with microcomputer applications in view. This is illustrated in Figure 3. In addition to DELPHI itself, the major functional components are as follows:

1. INPUT: Six routines for altering the command vocabulary. Four routines for transfering vectors and matrices. Three routines for altering control parameters. One routine for disk transfer.

2. OUTPUT: Seven routines for grapphical displays of vectors, including discrete line spectra. Five routines for graphical displays of matrices, including columsn as vector sequences, and surfaces with hidden line suppression. Two routines for displaying control parameters. One routine for displaying the command vocabulary. One routine for disk transfer.

3. UNFOLD: Thirteen routines for analyzing data with admixtures of continuum and discrete components.

4. SIMULATION: Thirteen routines for simulating response matrices and data.

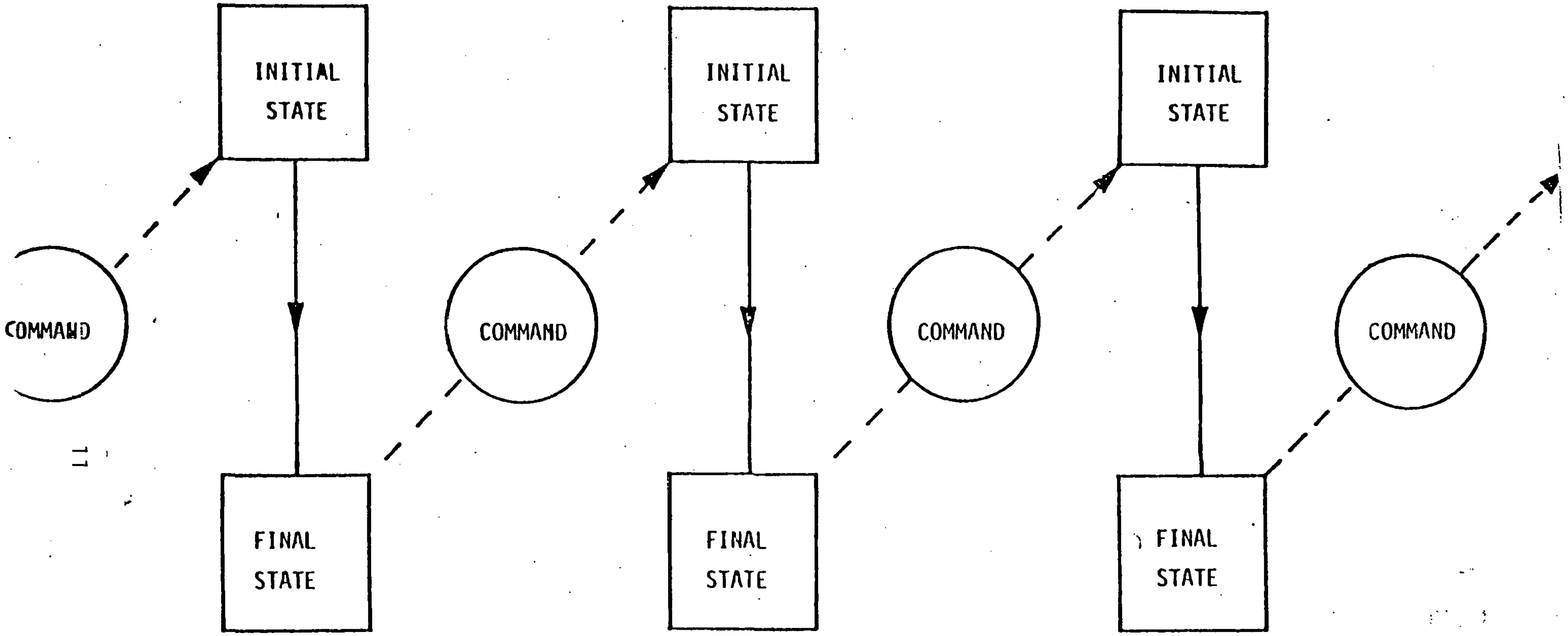

Figure 2. Interactive Unfolding

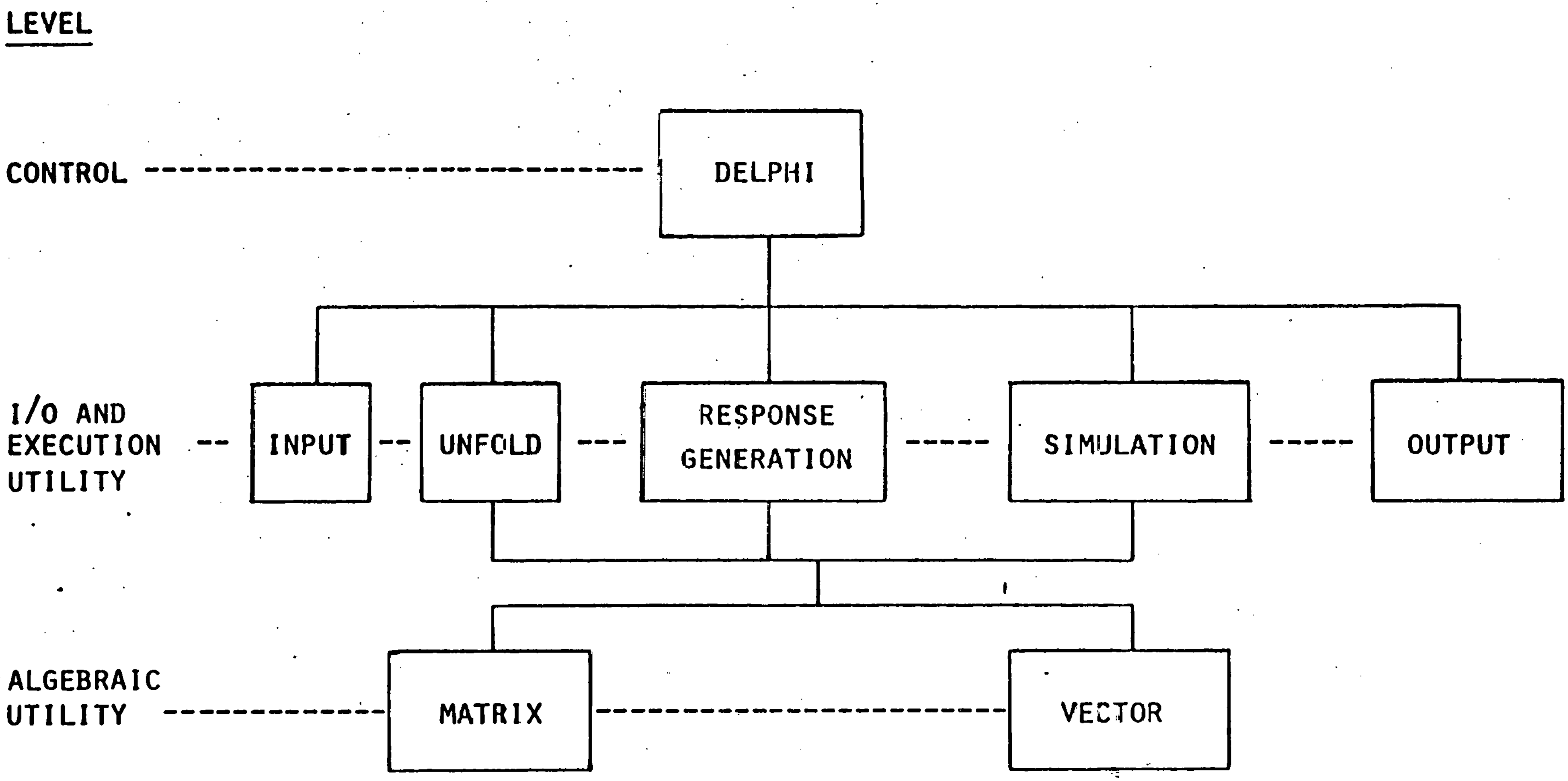

Figure 3. Program File Structure

5. GENERATION: Presently empty file, but allocated for routines under separate development for expenditious construction of actual spectrometer responses.

6. VECTOR: Eleven short, fast routines for vector algebra.

7. MATRIX: Five routines for matrix algebra, including Gram-Schmidt orthogonalization.

DELPHI contains six routines, four for command interpretation, one for interpretation of switch parameters (explained below), and one for command recognition and initiation of utility sequences.

The hierarchy of data structures is illustrated in Figure 4. Processes are initiated by commands, and commands are sequences or vectors of vocabulary entries, their proper order being deciperable by grammatic considerations. However, even when a process is specified, it can have many variants, depending upon values assumed by parameters that are either scalars or vectors of low dimensionality. Four types of parameters are distinguished in DELPHI, as follow:

1. Transfer Parameters: Specifications relevant to I/O operations, such as the name of the input file.

2. Display Parameters: Specifications relevant to output graphics, such as the perspective for viewing a matrix surface.

3. Unfold Parameters: Specifications relevant for employment of the data reduction algorithms, such as the number of data channels.

4. Simulation Parameters: Specifications relevant for construction of data and responses, such as the assumed detector size.

Within each parameter block, there are eight sixteen-position switches capable of altering modes of operation such as the functionally active unfolding algorithm. In practice, these switches have been better used for distinguishing between binary states, and they should perhaps be reconfigured to permit 32 (or actually 35-36 with the DEC-10 36 bit word) binary positions.

The command structure of DELPHI is reflexive in that is permits insertion or deletion of vocabulary data, including the definition of synonyms. For example, to display the part of the detector response matrix associated with discrete spectral lines, one might command

DISPLAY THE DISCRETE RESPONSE

However, if it were first commanded

MAKE 'K' SYNONYMOUS WITH 'RESPONSE'

an equivalent display command could be stated as

DISPLAY K(DISCRETE)

The number of lines represented in the discrete response is not stated explicitly, but rather is implicit in the parameter structure, which can also be changed by command. Hence, the viewpoint that the data architecture if hierarchical.

Command sentences are organized into phrases as follows: (1) verb, (2) object phrase, (3) adverbial phrase, (4), and (5) two prepositional phrases. The verb is always the first word reading from left to right whose vocabulary information permits interpretation as a verb. The adverbial and prepositional phrases are located by their being preceded with an adverb or preposition. The object phrase is then found by a process of elimination. A phrase consists of an identifier, either an adverb or preposition, a noun object, and an adjective modifier; except for the object phrase itself, which can consist of two noun-adjective pairs jointed by a conjunction. This structure was arrived at by writing down as many potential commands as could be invented, and then devising the minimum syntactical range capable of containing them. While hardly infinite, or even literate by human standards, it has proved quite flexible for man to machine communication within the scope of the unfolding problem.

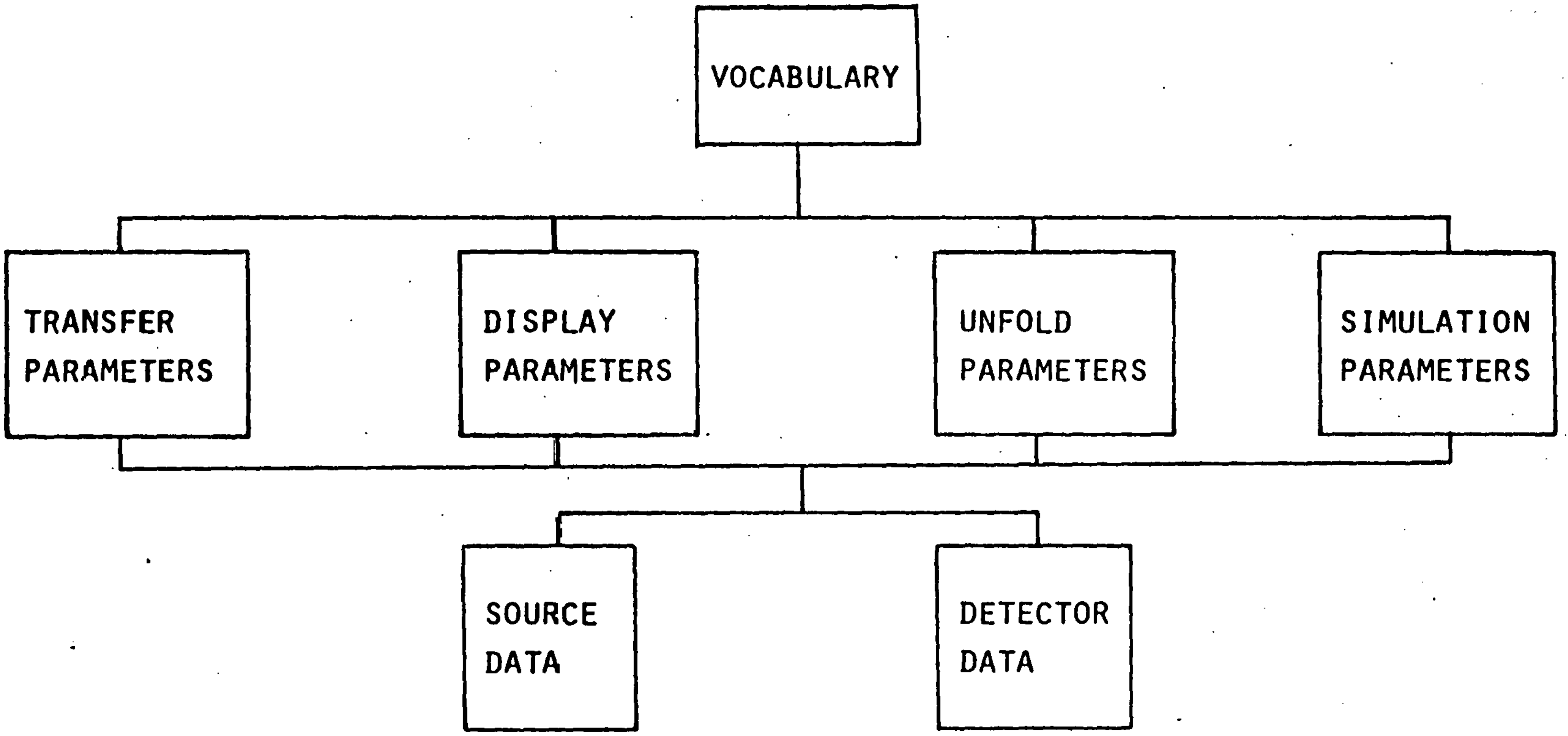

FIGURE 4. DATA BUFFERS

Interpretation is initiated by a carriage return. The words of the command sentence are first examined and categorized by parts of speech. Numbers are translated into their appropriate floating point or integer form. The sentence is then parsed according to the grammatical rules described in the preceding paragraph. If the object phrase is the word "it" or "them", it is replaced by the object phrase of the previous command. Synonums are replaced by "root words", the first word of the synonym group to have been entered into the vocabulary. Upon completion of these steps, there exists a fourteen-word vector (some of whose locations may be blank), which is passed through a decision tree to initiate action.

The structure of the software is such that action is usually initiated by a single subroutine call. This subroutine may be at an executive level, in turn calling lower level routines. For unfolding, the "bottom level", the level at which more than 99% of the CPU time is spent, is the level of vector algebra. Consequently, the subroutines in the VECTOR module are short--usually two or three FORTRAN lines--making them readily implementable in assembly language, microcode, or by any means that permits taking advantage of fast arithmetic circuitry.

1.3 OPTIMIZATION UNFOLDING

The approach to spectral unfolding in which a function is optimized as the spectral estimate is varied, is based on Bayesian statistics. In brief, the expectation value of the spectrum is given by the integral

$$\phi(E) = {}_{\mathrm{all}\,\bar{\phi}}\bar{\phi}\ f\ (\bar{\phi}|D)\ d\bar{\phi}, \qquad (2)$$

where $f(\bar{\phi}|D)$ is the condition probability that the spectral vector assumes the value $\bar{\phi}$ when the data vector assumes the observed value D, and where the range of integration is over all physically allowable spectra. This solution is an impractical one, however, because of the high dimensionality of the integral as determined by the number of degrees of freedom of the spectrum. Fortunately, $f(\bar{\phi}|D)$ tends to have a maximum in $\bar{\phi}$ closely localized at the expectation value. Therefore, optimization techniques can be applied to approximately that vector value.

It is difficult to formulate $f(\bar{\phi}|D)$ directly, because doing so requires thinking backward from the observed data to the object spectrum. Thinking forward requires use of the equivalent formulation

$$f(D|\bar{\phi})\ f(\bar{\phi})/f(D) = f(\bar{\phi}|D), \qquad (3)$$

where $f(D|\bar{\phi})$ is the conditional probability of observing data D when the object spectrum $\bar{\Phi}$ is measured, and where $f(\bar{\phi})$ and $f(D)$ are the <u>a priori</u> probability distributions of spectrum and data, respectively. Since the optimization is one in which the spectrum is varied, the $f(D)$ denominator behaves as an arbitrary constant which can be omitted without affecting the final result.

Another practical matter is that probabilities are awkward to work with, primarily because of their extreme numerical range are consequently sudden gradients. Liklihoods, defined as the logarithms of probabilities, have been useful in this regard, the Bayesian liklihood having the form

$$L(\bar{\phi}|D) = L_{\text{a posteriori}}(D|\bar{\phi}) + L_{\text{a priori}}(\phi). \qquad (4)$$

Optimizing the <u>a posteriori</u> term corresponds to what is conventionally known as the maximum liklihood technique, while inclusion of the <u>a priori</u> term generally regularizes the solution in the presence of statistical counting fluctuations and poorly conditioned response matrices. This formulation was applied to nuclear physics many years ago by Fermi, and was described in Jay Orear's <u>Notes on Statistics for Physicists</u> (Ref. 1). Analogous formulations have been suggested by A. N. Tikhonov (Ref. 2) and by D. L. Phillips (Ref. 3).

The negative of the likelihood is sometimes referred to as the information, information function, or information functional, and it decomposes into an analogous sum of a posteriori and a priori terms:

$$W(\phi|D) = W_{\text{a posteriori}}(D|\bar{\phi}) + W_{\text{a priori}}(\bar{\phi}). \quad (5)$$

The rationale behind this alternate definition is that liklihood has remained an isolated and ad hoc construct, while the concept of information is interwoven into a rich theory with many related insights and applications. This usage of the term information might be questioned by some purists, who would insist that information is a statistical concept only, attributable to a communication channel but not to a specific message, and measurable only in terms of entropy. However, as long as there do in fact exist two separate words, "information" and "entropy", and as long as it is understood that entropy is the expectation value of information, which itself is a random variable, the technical vocabulary is enriched and no confusion can arise. Furthermore, this technical usage is in good accord with colloquial practice.

1.4 MAZNAI: A SUPER-RESOLVING GAMMA-RAY SPECTRAL UNFOLDING CODE FOR NaI DATA WITH DISCRETE AND CONTINUUM COMPONENTS

In unfolding NaI data with discrete and continuum spectral components, the problem naturally arises of determining the presence and energy of all resolveable gamma-ray lines. Two methods immediately suggest themselves: (1) perform a peak search on the NaI data using a peak search algorithm; or, (2) unfold the data using one of the conventional unfolding algorithms, incorporating the spectrometer energy resolution into the response matrix and stressing the algorithm toward maximum resolution, then apply the peak search algorithm or read the spectral graph manually. These methods have serious limitations. Peak strength algorithms are notoriously poor at resolving doublets and triplets aggregated within data by energy spacings small with respect to intrinsic resolution. This problem is aggravated by the presence of Compton edges and above 1 Mev by single and double escape peaks. Unfolding the data before searching removes the competing edges and escape peaks but in practice does little or nothing to improve resolution beyond the limit set by intrinsic detector characteristics. Attempts to exceed this limit generally result in the appearance of paradoxical oscillations, readily mistaken for actual peaks.

These oscillations are a consequence of the contrastingly different frequency contents of signal and noise (frequency content" referring to the presence in data of wavelength components as revealed by Fourier analysis). Signal bandwidth is limited by spectrometer resolution, narrowing in frequency as intrinsic resolution broadens in energy. In the vicinity of the limiting bandwidth, the signal power spectrum falls rapidly to small values. Noise represented by statistical counting fluctuations holds its power virtually unchanged to arbitrarily high frequencies. Consequently, any attempt to improve the spectral resolution by linear techniques produces a corresponding upward weighting of all high frequency components, with increased dominance of noise over signal. This is a characteristic of linear systems, not a fundamental information theoretic limitation: If, for example, all peaks sit on a continuum-free zero baseline, the resolution limit can readily be exceeded by the spectr-m that minimizes an information function in the form of Equation (5), with a positively constrained estimation space. This non-linear technique is effective for super-resolution because paradoxical oscillations about a zero baseline have a much stronger tendency to swing positive and negative than to remain strictly positive, resulting from involvement of lower frequencies in the latter case. Consequently, a weak regularization function, $W_{a\ priori}$ is able to suppress oscillations without degrading algorithmic resolution.

In the MAZNAI implementation, a non-zero baseline or continuum is incorporated by treating the spectral estimate in the j-th image energy channel as the superposition of a continuum and a discrete component,

$$Q_j = Q_j^C + Q_j^D \tag{6}$$

The solution is interative, with a low-pass Lengendre filter used to keep high frequency oscillations from building up in the continuum estimate. Derivation of the (m+1)-th estimate is illustrated in Figure 5. Initialization at a large continuum/discrete ratio, and convergence of the continuum only from the overestimate side, ensures the continuing presence of a zero-baseline discrete structure.

Examples of MAZNAI spectral enhancement are shown in Figures 6 and 7. The existence of all enhanced lines has been verified by separate GeLi experiments. Accuracy will be studied in detail in a future paper, but in general, peaks with the greatest intensities tend to have accuracies consistent with statistics and resolution capabilities. Peaks with the smallest intensities tend to be systematically underestimated, and peaks below some recognition threshold are absent from the discrete component but may in groups influence the continuum. Simulation studies have shown MAZNAI capable of resolving doublets, triplets, and quadruplets. The absence of subsidiary oscillations is characteristic of this technique.

1.5 MAZAS: A LINE-STRENGTH ESTIMATION CODE FOR NaI DATA WITH DISCRETE AND CONTINUUM COMPONENTS

Complete specification of an unbroadened discrete spectrum consists of listing two quantities per line, energy and intensity. These quantities are quite different conceptually and in the construction of efficient algorithms for their estimation. Energies can be determined by a variety of techniques

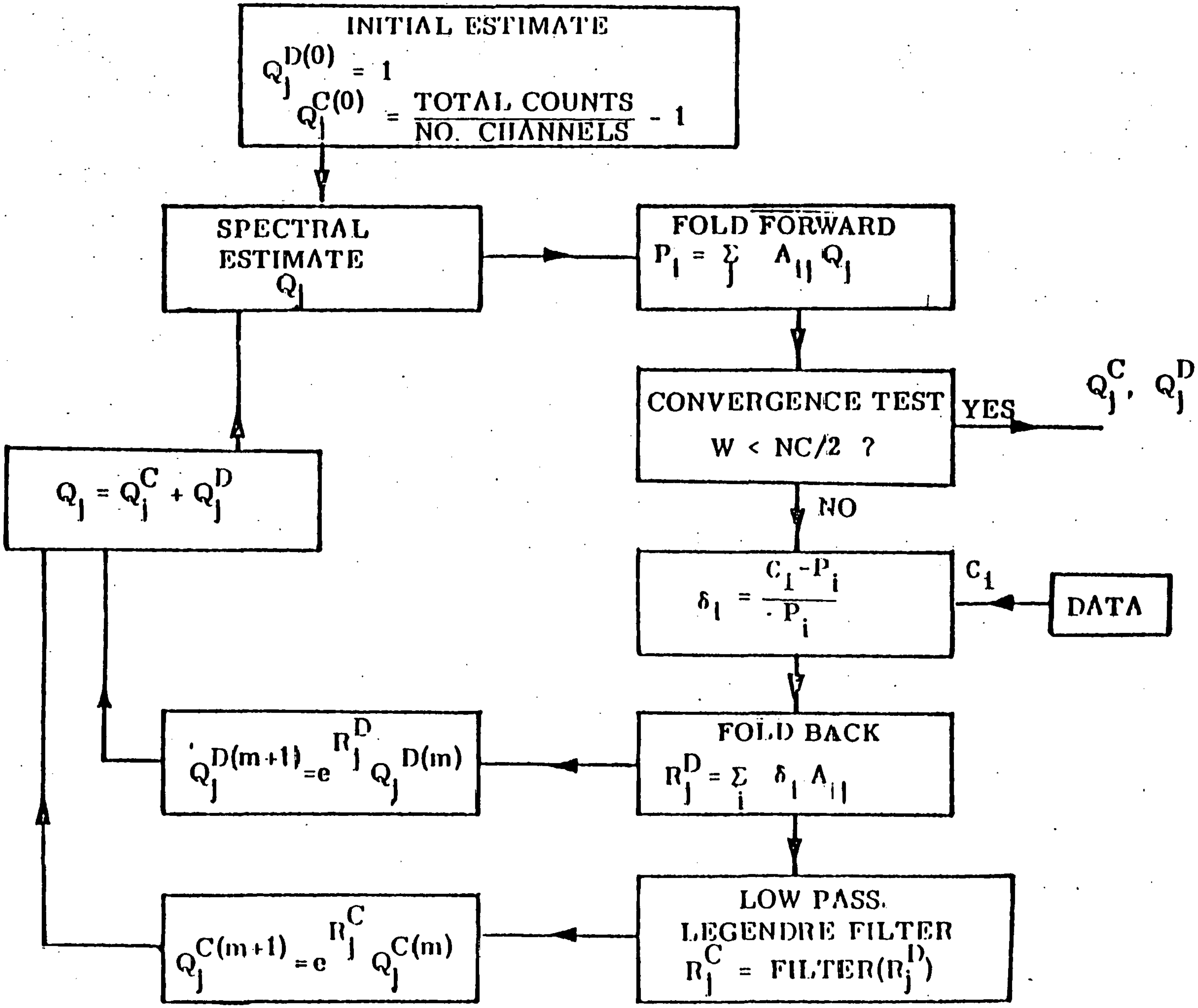

Figure 5. Simplified MAZNAI Block Diagram

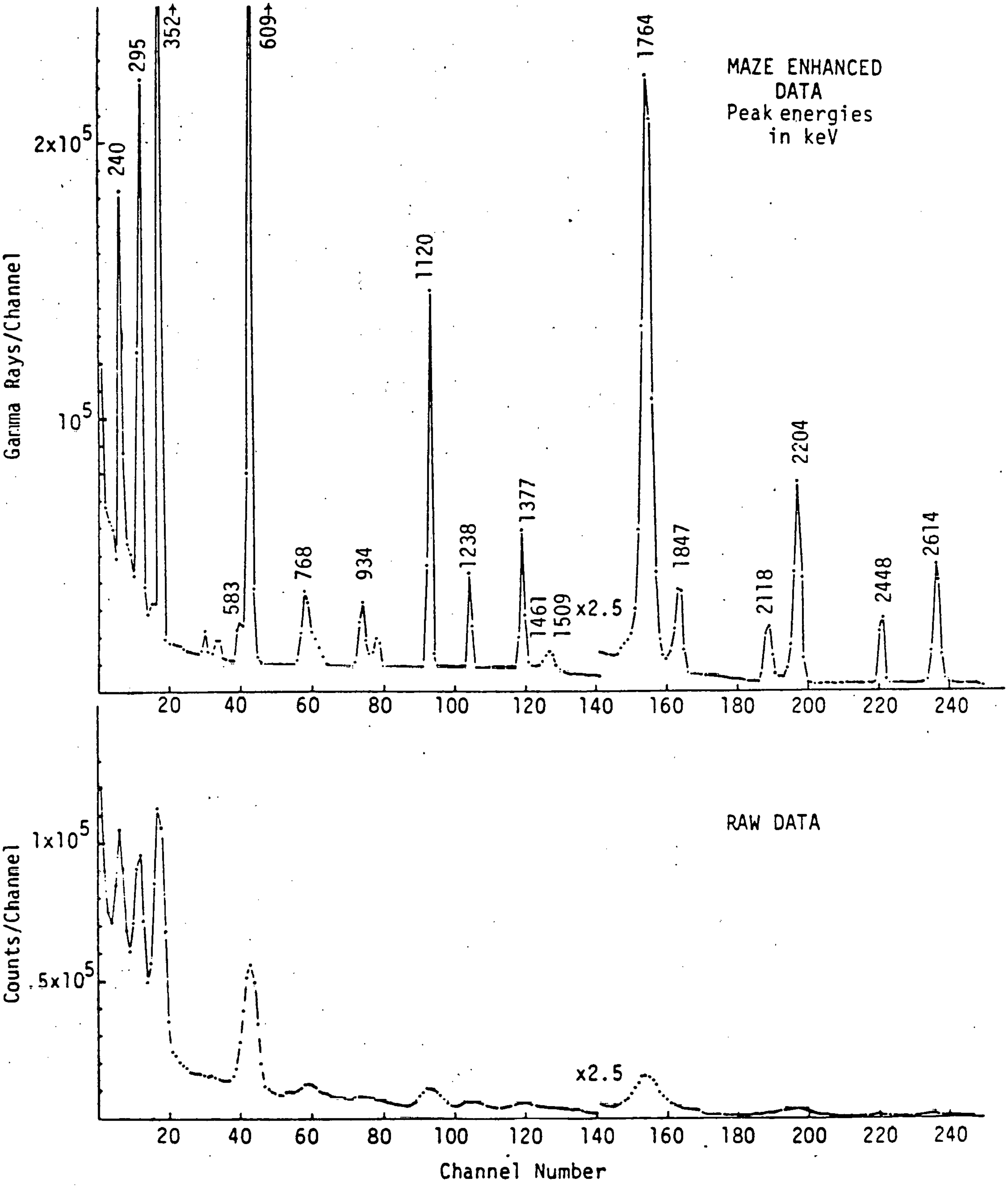

Figure 6. Example of MAZNAI Unfolding (Uranium Ore with 3-by-3 inch NaI Detector)

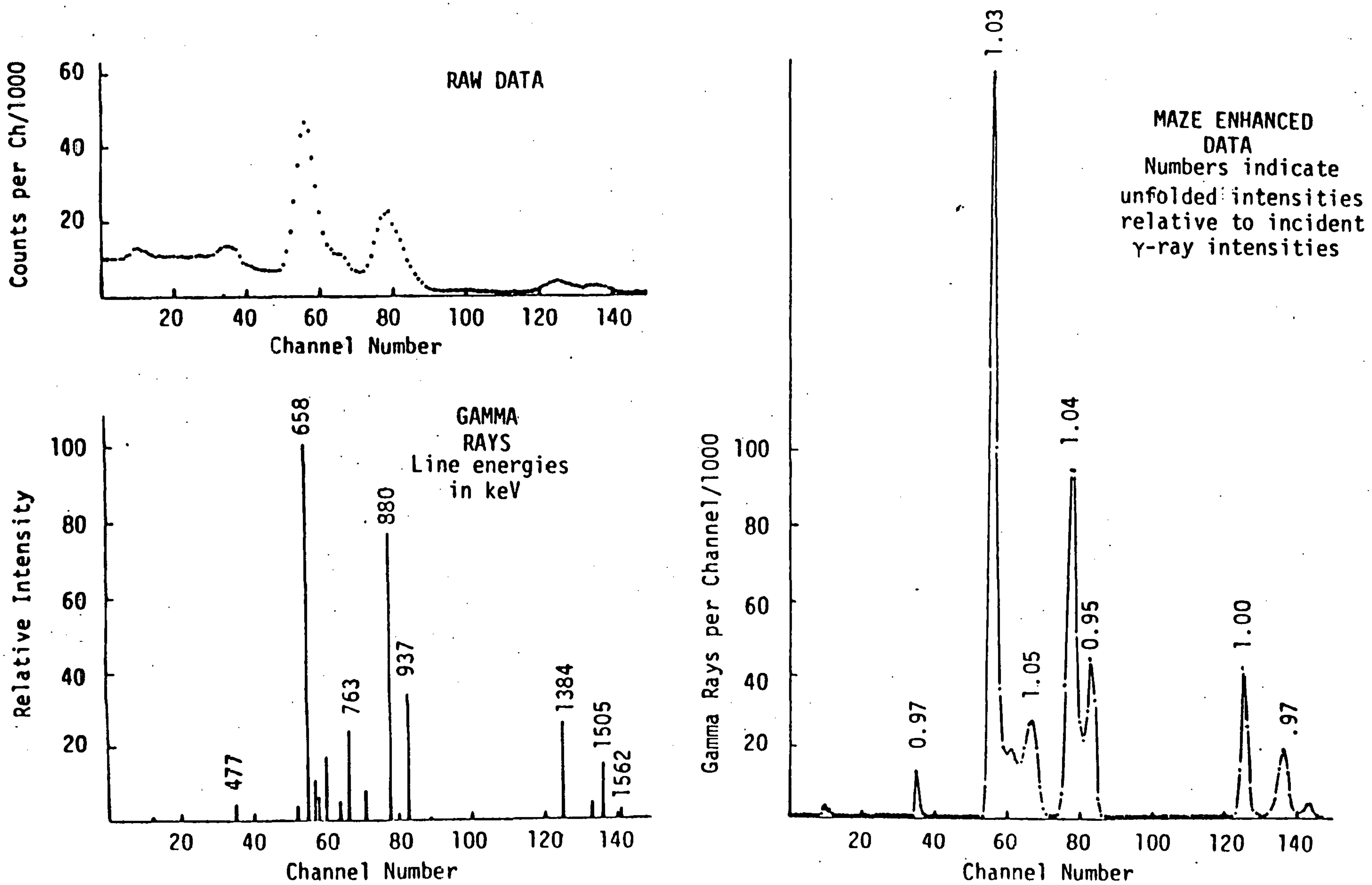

Figure 7. MAZNAI Unfolding with Source Spectrum (Silver-110 with 3-by-3 inch NaI Detector Source from GeLi Data). Values above MAZE Enhanced Peaks are Ratios of Image to Object Line Intensities. with Ratio at 1384 kev

but with the limited intrinsic resolution of NaI spectrometers a degree of super-resolution is likely to be required. Such computations tend to contain non-linear elements and in the high performance limit to be relatively time consuming. Intensity estimation is more straightforward and algorithms can be more linear. Extremely high speeds are possible.

With known line energies, "windowing", or the integration of counts over full energy peaks, is a rapid technique readily extended for continuum subtraction, but is subject to errors from continuum anomalies like Compton edges and from overlapping peaks. Reconditioning with an unfolding code improves this situation, but is time-consuming and never fully removes peak overlaps even when the energies of all participating lines are accurately known. By modeling the spectrum as a superposition of continuum and discrete analytic functions;

$$\phi(E) = \sum_{\lambda=1}^{n\ \text{continuum}} \phi_\lambda^C f_\lambda(E) + \sum_{\lambda=1}^{n\ \text{discrete}} \phi_\lambda^D \delta(E-E_\lambda), \quad (7)$$

where ϕ^C and ϕ^D and the continuum and discrete intensity parameters, where $f_\lambda(E)$ is the λ-th order continuum basis function, and where $\lambda(E)$ is the Dirac delta function; an optimization algorithm can be derived for direct estimation of the model parameters. This process, while accurate, is also relatively time-consuming in its exact form, because the non-quadricity of the information function leads to a non-linear, i.e., interative solution, and because each iterative stage requires matrix inversion or solution of coupled linear equations.

For MAZAS, an algorithm was developed which is close to windowing in speed and to analytic modeling in accuracy. To make this analogy more precise, the mathematical form of the windowing technique can be represented as

$$\phi_\lambda^D = \Sigma\omega_\lambda^i D_i, \quad (8)$$

where the weight factors for the λ-th line are unity over the full energy peak and zero elsewhere. When background subtraction is necessary, the weight factors can assume a range of real values. The same form holds in MAZAS, but the weights are determined by approximately optimizing an information function dependent on the continuum can discrete model parameters.

The specific approximations are as follows:

1. The information function is expanded to a second order Taylor series about its minimum.
2. Data variance is assumed to have the energy dependence of a specific Laplace superposition fitted to the average-true data variance.
3. The continuum basis functions are assumed to be modified Laguerre polynomials, pretreated to be orthogonal within the spectrometer energy window.

These assumptions plus the assumed line energies permit determination of the line intensities by setting to zero the first derivative of the information function with respect to the model parameters, and solving the resulting linear equations. In MAZAS, this solution is achieved by Gram-Schmidt orthogonalization. Unfolding times with the resulting weight factors are on the order of .1 second for 256-channel data with 20 lines, in the DEC-10 FORTRAN implementation. There appears to be considerable room for improvement in this figure by truncating small weight elements to zero.

THIS PAGE

WAS INTENTIONALLY

LEFT BLANK

REFERENCES

1. Orear, J. 1958 Notes on Statistics for Physicists. University of California Radiation Laboratory Report UCRL-8417.

2. Tikhonov, A. N. 1963. "The Solution of Incorrectly Posed Problem and the Method of Regularization". Doklady Akad, Nauk SSSR. IJI, No. 3: 501-504.

3. Phillips, D. L. 1962. J. Assoc. Comp. Mach. 9:87.

THIS PAGE
WAS INTENTIONALLY
LEFT BLANK

EFFECTS OF OVERBURDEN, SNOW COVER SOIL POROSITY AND FLIGHT ALTITUDE ON SIGNAL RADIATION DURING AIRBORNE RECONNAISSANCE FOR URANIUM

Submitted to

Bendix Field Engineering Corporation

By

W. A. Woolson

July, 1977

THIS PAGE
WAS INTENTIONALLY
LEFT BLANK

To construct, deploy and calibrate an airborne reconnaissance system for uranium exploration and to interpret the data obtained from such a system, it is necessary to understand the sensitivity of the reconnaissance parameters on the system performance. By reconnaissance parameters, we mean such items as flight altitude, flight speed, terrain, ground composition, ground cover, air density, relative humidity and detector construction. In addition to reconnaissance parameters, other items such as overburden thickness and extent of ore field effect the interpretation of the nature of the ore body from the data taken during flight.

One cannot construct calibration facilities to experimentally determine the effect of all these important parameters. One could analyze parametric variations for most of the items mentioned above with a well-planned set of detailed radiation transport calculations. In lieu of both experimental data or extensive transport calculations, a methodology exists to enable an investigation of these effects on the signal radiation. We use the term signal radiation or signal flux to mean the uncollided (unscattered) radiation field from the emission of discrete energy photons from radioactive nuclides. This approach can be used for analysis of emission lines of all energies of interest but specifically does not include the single and multi-scattered radiation background. This methodology is useful for the following cases or problems.

- The ratio of line strengths are used to extract information.
- Usually the signal line(s) is larger than the scattered background.
- Estimation of background effects when experimental or calculational data is just not available.

- Designing of detector arrangements or collimator systems to maximize signal contribution.
- Analysis of flight speed effects on detection of small bodies of ore.
- Analysis of relative contribution of signal from ground compared to airborne source signal as a function of altitude, atmospheric density and humidity and airborne concentration.
- Effects of terrain, ground cover, overburden, soil porosity, rain saturation, ground composition, ore extent on signal strength.

The following discusses some preliminary analysis with this approach. This preliminary analysis incorporates some simplifications which could easily be removed in a more detailed but relatively straightforward analysis. Specifically, simplifying assumptions used here which are not required to apply the basic approach include:

- flat ground plane,
- sources are uniform and infinite in extent parallel to the ground plane,
- air density is constant at 1.22×10^{-3} gm/cm^3,
- air is dry (zero humidity),
- detector is isotropic and unshielded,
- ground water uniformly distributed (no variation in depth).

With these simplifying assumptions, the signal flux can be computed analytically. The calculational configuration is shown in Fig. 1 and the equations for the signal flux are shown in Table 1 and 2. The proofs for these equations are contained in the Appendices. A computer code, ABRA (Airborne Reconnaissance Analysis) was written to take user inputs and output

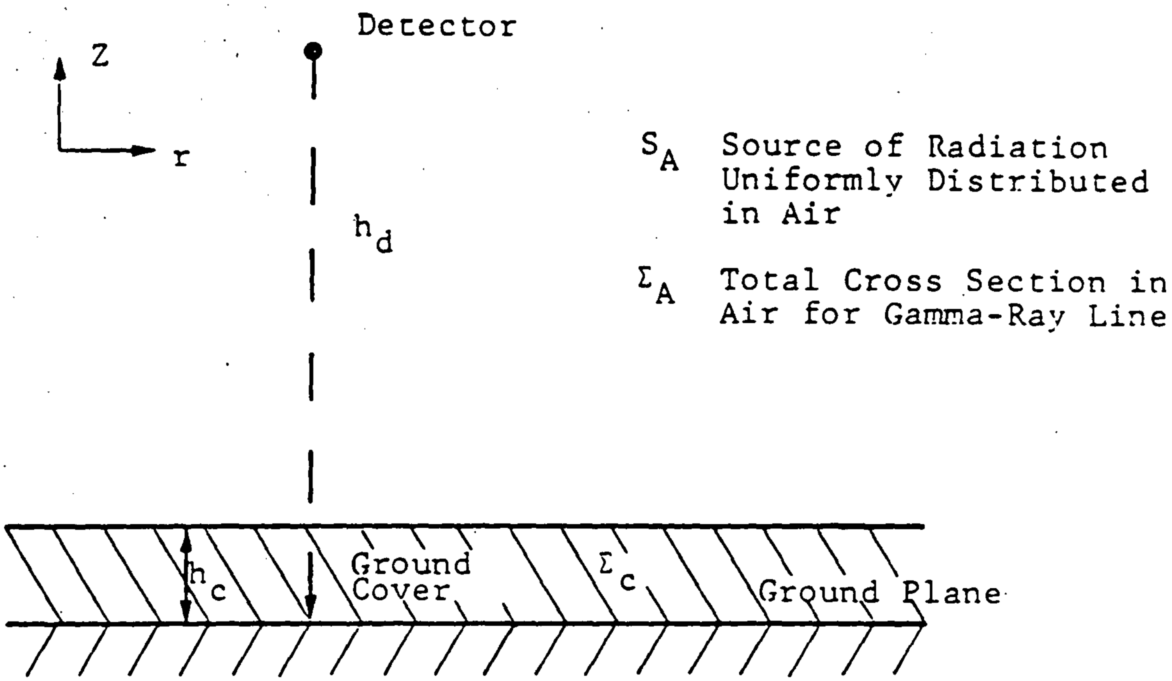

S_g Source of Radiation Uniformly Distributed in Ground

Σ_g Total Cross Section for Gamma-Ray Line in Source

Figure 1. Calculational Configuration.

Table 1. Equations for Uncollided Flux

Case	Air Source	Ground Source
No ground cover ($h_i = 0$)	$\phi_A = \frac{S_A}{2\Sigma_A}\left[2 - E_2(\Sigma_A h_d)\right]$	$\phi_g = \frac{S_g}{2\Sigma_g}\left[E_2(\Sigma_A h_d)\right]$
With ground cover	$\phi_A = \frac{S_A}{2\Sigma_A}\left[2 - E_2\left[\Sigma_A(h_d - h_c)\right]\right]$	$\phi_g = \frac{S_g}{2\Sigma_g}\left[E_2\left[\Sigma_c h_c + \Sigma_A(h_d - h_c)\right]\right]$

where $E_2(X) = \int_1^\infty \frac{e^{-Xt}}{t^2}\, dt$

Table 2. Additional Flux Equations with Ground Cover

Flux from air source above detector: $\frac{S_A}{2\Sigma_a}$

Flux from air source below detector: $\frac{S_A}{2\Sigma_a}\left[1-E_2\left[\Sigma_A(h_d-h_c)\right]\right]$

Flux from air source on plane at distance, h, from detector : $\frac{S_A}{2}\left[E_1(\Sigma_A h)\right]$

Flux from air source in band of thickness, t, at distance, h, from detector : $\frac{S_A}{2\Sigma_a}\left[E_2(\Sigma_a h) - \left(E_2\ \Sigma_a(h+t)\right)\right]$

Flux from source plane in ground a distance h_g below surface : $\frac{S_g}{2}\left[E_1\left(\Sigma_a(h_d-h_c) + \Sigma_c h_c + \Sigma_g h_g\right)\right]$

Flux from source band in ground a distance h_g below surface of thickness t :

$$\frac{S_g}{2\Sigma_g}\left[E_2\left(\Sigma_a(h_d-h_c) + \Sigma_c h_c + \Sigma_g h_g\right) - E_2\left(\Sigma_a(h_d-h_c) + \Sigma_c h_c + \Sigma_g(h_g+t)\right)\right]$$

where $E_N(X) = \int_1^{\infty} \frac{e^{-Xt}}{t^N}\, dt$

the signal flux information in an appropriate manner. Tables 3 and 4 contain a sample output from ABRA.

To study the effect of parameter variations, we need a baseline case to establish a basis for comparison. The baseline used here is not intended to be a nominal case but rather the "zero point" for many of the parameters. The baseline case is defined as:

- sandstone ground composition of zero porosity and density 2.645 gm/cm^3,
- no ground cover,
- no overburden,
- detector altitude of 400 ft.

From this base case we present a study of the effects of porosity, ground cover, overburden and flight altitude on the signal flux at the detector using results from the ABRA code. Figure 2 presents the variation in the total macroscopic cross section with energy for the three materials used in this analysis. The line energies considered in this analysis range from 0.2 MeV to 2 MeV. Specific lines corresponding to, say, the uranium series are not analyzed, but rather, a continuous variation over the energy range is presented to facilitate analysis of any line from any nuclide which falls between 0.2 and 2.0 MeV.

Figure 3 presents a study of the effect of flight altitude on the relative contribution to the total air flux from sources between the ground and detector. On the basis of our assumptions of a uniform air source, we see that a perfect 2π shield for sources above the detector still leaves more than 40% of the air flux for the 400-ft. altitude. There is not an unusually large variation with flight altitude.

Table 3. Example of ABRA Run for a Line Energy of 0.4 MeV and Flight Altitude of 200 Feet.

```
 SURVEY STUDY,DETECTOR ALTITUDE = 200 FT

**** PROBLEM DATA ****
LINE ENERGY(MEV)        0.40
AIR SOURCE              0.12E-02
GROUND SOURCE           0.26E+01
DETECTOR ALTITUDE       0.61E+04
GROUND COVER HGT        0.00E+00

CROSS SECTION DATA
 MIXTURE    ELEMENT NO       Z        ATM/(BN-CM)   COMPTON       PHOTO       TOTAL
    1           1           7.0        4.02E-05    8.92E-05    2.32E-08    8.92E-05
    1           2           8.0        1.07E-05    2.71E-05    1.18E-08    2.71E-05
    2           1           1.0        6.69E-02    2.12E-02    2.49E-09    2.12E-02
    2           2           8.0        3.34E-02    8.47E-02    3.70E-05    8.47E-02
    3           1           6.0        1.88E-03    3.48E-03    4.96E-07    3.49E-03
    3           2           8.0        5.15E-02    1.31E-01    5.71E-05    1.31E-01
    3           3          11.0        2.29E-04    7.98E-04    1.20E-06    7.99E-04
    3           4          12.0        4.66E-04    1.77E-03    3.70E-06    1.77E-03
    3           5          13.0        1.50E-03    6.15E-03    1.75E-05    6.17E-03
    3           6          14.0        2.09E-02    9.25E-02    3.48E-04    9.28E-02
    3           7          15.0        1.67E-05    7.94E-05    3.88E-07    7.98E-05
    3           8          16.0        1.39E-04    7.05E-04    4.40E-06    7.10E-04
    3           9          19.0        4.50E-04    2.70E-03    3.22E-05    2.74E-03
    3          10          20.0        1.57E-03    9.94E-03    1.43E-04    1.01E-02
    3          11          22.0        3.33E-05    2.32E-04    4.76E-06    2.37E-04
    3          12          26.0        2.82E-04    2.32E-03    8.81E-05    2.41E-03
TOTAL CROSS SECTIONS FOR AIR =  1.16E-04 , FOR GROUND COVER =  1.06E-01 , FOR GROUND =  2.52E-01, POROSITY =  0.0000

**** AIR DATA ****
MFP TO GROUND COVER          =       0.71
FLUX FROM ABOVE DETECTOR     =       5.25E+00
FLUX FROM BELOW DETECTOR     =       4.03E+00
TOTAL AIR SOURCE FLUX        =       9.28E+00
RATIO OF FLUX BELOW TO TOT   =       4.34E-01

**** GROUND DATA ****
 INTERVAL      DEPTH      MFP TO DET  NORMALZD FLUX OVERBURDEN FLUX INTEGRAL FLUX RATIO TO TOTAL  SOURCE * FLUX  SRCE* INT FLUX
     1          19.0         5.49      2.80E-04       1.12E-03       2.80E-04       6.08E-04       7.40E-04       7.40E-04
     2          18.0         5.24      3.75E-04       1.50E-03       6.54E-04       1.42E-03       9.91E-04       1.73E-03
     3          17.0         4.99      5.03E-04       2.00E-03       1.16E-03       2.52E-03       1.33E-03       3.06E-03
     4          16.0         4.74      6.76E-04       2.68E-03       1.83E-03       3.98E-03       1.79E-03       4.85E-03
     5          15.0         4.49      9.10E-04       3.59E-03       2.74E-03       5.96E-03       2.41E-03       7.25E-03
     6          14.0         4.24      1.23E-03       4.81E-03       3.97E-03       8.63E-03       3.25E-03       1.05E-02
     7          13.0         3.98      1.66E-03       6.48E-03       5.63E-03       1.22E-02       4.40E-03       1.49E-02
     8          12.0         3.73      2.26E-03       8.73E-03       7.89E-03       1.72E-02       5.97E-03       2.09E-02
     9          11.0         3.48      3.07E-03       1.18E-02       1.10E-02       2.38E-02       8.13E-03       2.90E-02
    10          10.0         3.23      4.20E-03       1.60E-02       1.52E-02       3.30E-02       1.11E-02       4.01E-02
    11           9.0         2.98      5.76E-03       2.18E-02       2.09E-02       4.55E-02       1.52E-02       5.53E-02
    12           8.0         2.72      7.94E-03       2.97E-02       2.89E-02       6.28E-02       2.10E-02       7.63E-02
    13           7.0         2.47      1.10E-02       4.07E-02       3.99E-02       8.67E-02       2.91E-02       1.05E-01
    14           6.0         2.22      1.54E-02       5.61E-02       5.52E-02       1.20E-01       4.06E-02       1.46E-01
    15           5.0         1.97      2.16E-02       7.77E-02       7.68E-02       1.67E-01       5.71E-02       2.03E-01
    16           4.0         1.72      3.07E-02       1.08E-01       1.07E-01       2.34E-01       8.11E-02       2.84E-01
    17           3.0         1.46      4.40E-02       1.52E-01       1.52E-01       3.29E-01       1.16E-01       4.01E-01
    18           2.0         1.21      6.43E-02       2.17E-01       2.16E-01       4.69E-01       1.70E-01       5.71E-01
    19           1.0         0.96      9.58E-02       3.12E-01       3.12E-01       6.78E-01       2.53E-01       8.24E-01
    20           0.0         0.71      1.47E-01       4.60E-01       4.59E-01       9.98E-01       3.90E-01       1.21E+00
*** RATIO OF AIR TO GROUND FLUX =  7.64E+00
```

Table 4. Example of ABRA Run for a Line Energy of 1.0 MeV and Flight Altitude of 800 Feet.

```
 SURVEY STUDY,DETECTOR ALTITUDE = 800 FT

**** PROBLEM DATA ****
LINE ENERGY(MEV)       1.00
AIR SOURCE             0.12E-02
GROUND SOURCE          0.26E+01
DETECTOR ALTITUDE      0.24E+05
GROUND COVER WGT       0.00E+00

CROSS SECTION DATA
  MIXTURE    ELEMENT NO       Z         ATM/(BN-CM)  COMPTON       PHOTO        TOTAL
     1           1           7.0        4.02E-05     5.95E-05     2.53E-09     5.95E-05
     1           2           8.0        1.07E-05     1.81E-05     1.29E-09     1.81E-05
     2           1           1.0        6.69E-02     1.01E-02     2.73E-10     1.01E-02
     2           2           8.0        3.34E-02     5.65E-02     4.03E-06     5.65E-02
     3           1           6.0        1.84E-03     2.33E-03     5.41E-08     2.33E-03
     3           2           8.0        5.15E-02     8.71E-02     6.21E-06     8.71E-02
     3           3          11.0        2.29E-04     5.32E-04     1.30E-07     5.32E-04
     3           4          12.0        4.66E-04     1.18E-03     4.02E-07     1.18E-03
     3           5          13.0        1.50E-03     4.10E-03     1.90E-06     4.11E-03
     3           6          14.0        2.09E-02     6.17E-02     3.79E-05     6.17E-02
     3           7          15.0        1.67E-05     5.30E-05     4.23E-08     5.30E-05
     3           8          16.0        1.39E-04     4.71E-04     4.80E-07     4.71E-04
     3           9          19.0        4.50E-04     1.80E-03     3.51E-06     1.81E-03
     3          10          20.0        1.57E-03     6.63E-03     1.56E-05     6.65E-03
     3          11          22.0        3.33E-05     1.55E-04     5.21E-07     1.55E-04
     3          12          26.0        2.82E-04     1.55E-03     9.70E-06     1.56E-03
TOTAL CROSS SECTIONS FOR AIR =  7.76E-05 , FOR GROUND COVER =  7.06E-02 , FOR GROUND =  1.68E-01, POROSITY =  0.0000

**** AIR DATA ****
MFP TO GROUND COVER          =       1.89
FLUX FROM ABOVE DETECTOR     =       7.86E+00
FLUX FROM BELOW DETECTOR     =       7.52E+00
TOTAL AIR SOURCE FLUX        =       1.54E+01
RATIO OF FLUX BELOW TO TOT =         4.89E-01

**** GROUND DATA ****
 INTERVAL       DEPTH       MFP TO DET  NORMALIZED FLUX OVERBURDEN FLUX INTEGRAL FLUX RATIO TO TOTAL  SOURCE * FLUX  SRCE* INT FLUX
     1           19.0          5.08       4.75E-04        2.72E-03        4.76E-04       3.69E-03       1.26E-03       1.26E-03
     2           18.0          4.91       5.80E-04        3.30E-03        1.06E-03       8.18E-03       1.53E-03       2.79E-03
     3           17.0          4.74       7.06E-04        4.01E-03        1.76E-03       1.37E-02       1.87E-03       4.66E-03
     4           16.0          4.57       8.61E-04        4.87E-03        2.62E-03       2.03E-02       2.28E-03       6.94E-03
     5           15.0          4.41       1.05E-03        5.92E-03        3.67E-03       2.85E-02       2.78E-03       9.72E-03
     6           14.0          4.24       1.28E-03        7.20E-03        4.96E-03       3.84E-02       3.40E-03       1.31E-02
     7           13.0          4.07       1.57E-03        8.77E-03        6.53E-03       5.06E-02       4.15E-03       1.73E-02
     8           12.0          3.90       1.92E-03        1.07E-02        8.45E-03       6.55E-02       5.09E-03       2.24E-02
     9           11.0          3.74       2.36E-03        1.31E-02        1.08E-02       8.38E-02       6.20E-03       2.86E-02
    10           10.0          3.57       2.90E-03        1.59E-02        1.37E-02       1.06E-01       7.66E-03       3.62E-02
    11            9.0          3.40       3.56E-03        1.95E-02        1.73E-02       1.34E-01       9.42E-03       4.57E-02
    12            8.0          3.23       4.39E-03        2.39E-02        2.17E-02       1.68E-01       1.16E-02       5.73E-02
    13            7.0          3.06       5.41E-03        2.93E-02        2.71E-02       2.10E-01       1.43E-02       7.16E-02
    14            6.0          2.90       6.70E-03        3.60E-02        3.38E-02       2.62E-01       1.77E-02       8.93E-02
    15            5.0          2.73       8.30E-03        4.43E-02        4.21E-02       3.26E-01       2.20E-02       1.11E-01
    16            4.0          2.56       1.03E-02        5.46E-02        5.24E-02       4.06E-01       2.73E-02       1.39E-01
    17            3.0          2.39       1.28E-02        6.75E-02        6.52E-02       5.05E-01       3.40E-02       1.73E-01
    18            2.0          2.23       1.61E-02        8.35E-02        8.13E-02       6.30E-01       4.25E-02       2.15E-01
    19            1.0          2.06       2.01E-02        1.04E-01        1.01E-01       7.86E-01       5.33E-02       2.68E-01
    20            0.0          1.89       2.54E-02        1.29E-01        1.27E-01       9.83E-01       6.71E-02       3.35E-01
*** RATIO OF AIR TO GROUND FLUX =  4.59E+01
```

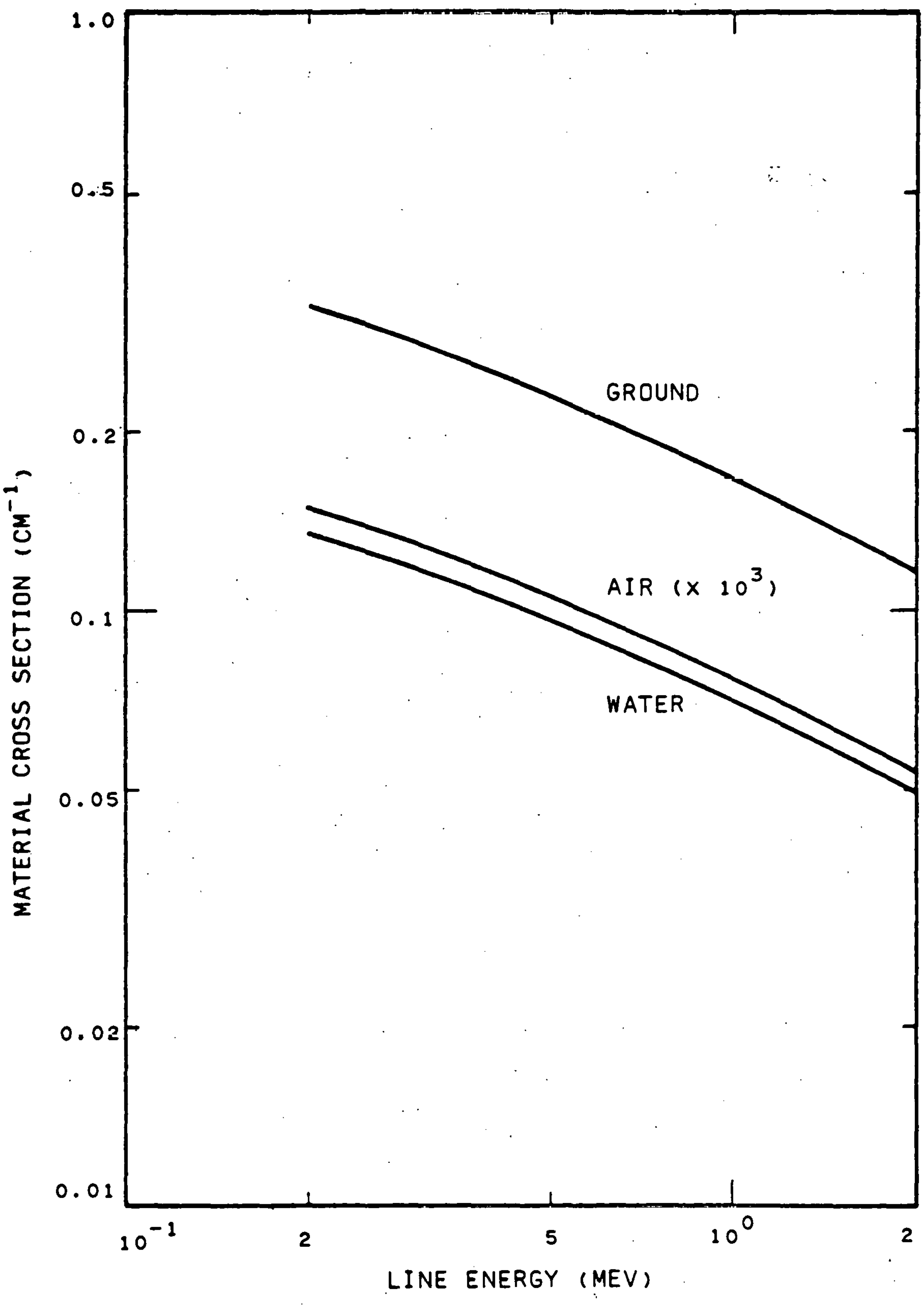

Figure 2. Macroscopic cross sections for ground, air, and water as a function of line energy.

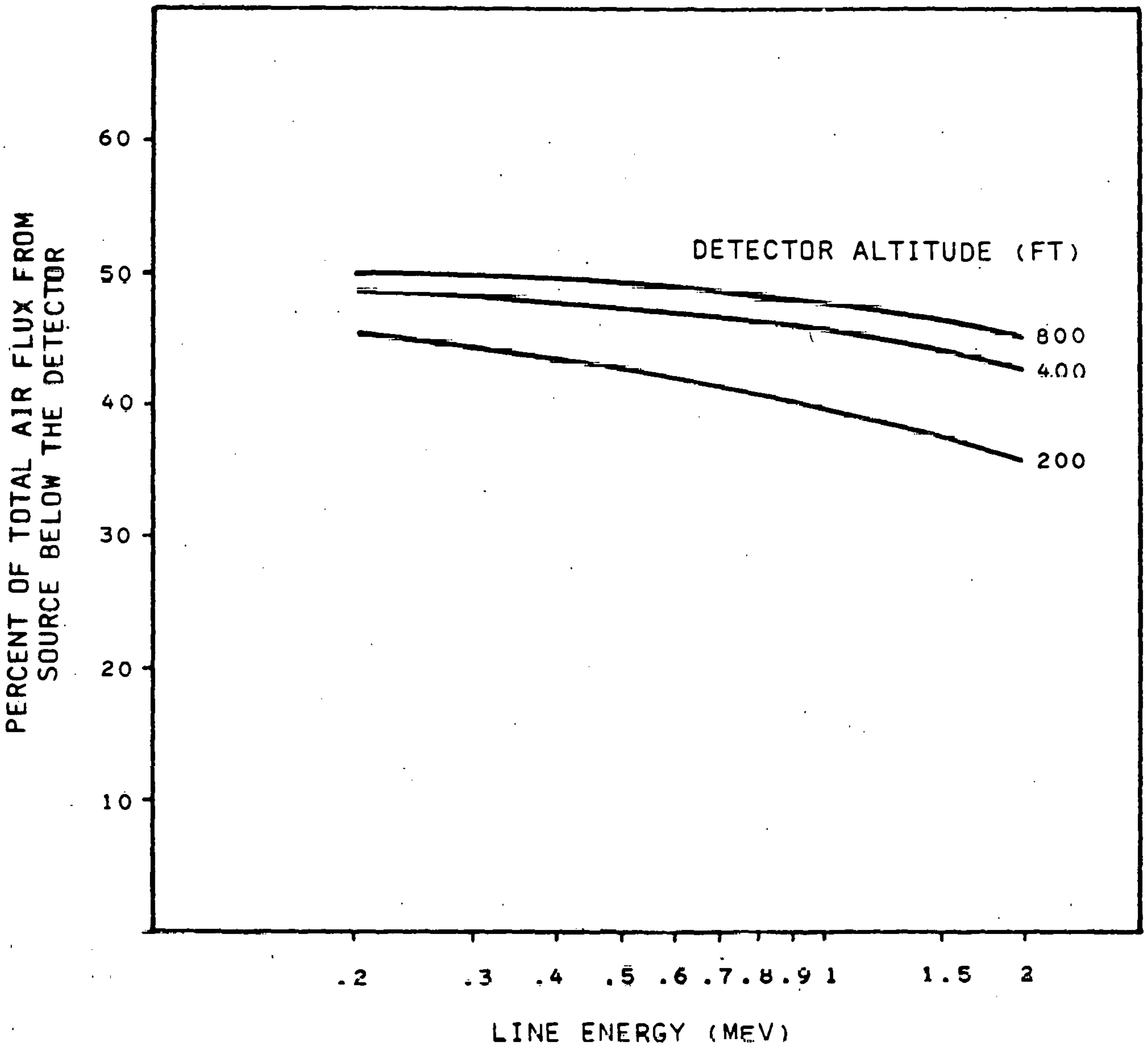

Figure 3. Percent of the total uncollided flux from air sources which comes from the air source below the detector. Assumes uniform air density and source distribution.

The relative variation in the signal as a function of depth in the soil of the source is shown in Fig. 4. There is a large variation with depth for the different energies. A 2.0-MeV line drops about a factor of 20 in 20 cm while the 0.2-MeV line drops 3 orders of magnitude. Relative intensities between several lines might be used to determine depth of an ore strata. Figure 5 presents similar results on the effect of overburden. In Fig. 5 the ore body is assumed infinite in depth below the overburden. To obtain the actual signal flux in units of photons/cm^2/sec, the ordinate is multiplied by the source strength factor in units of source photons/cm^3/sec. Note that we assume that ore is in a dilute concentration to the extent that it does not effect the total cross section of the ground. That is, we assume a linear signal with concentration. Non-linear variations could be easily incorporated in a more detailed model. The next figure (Fig. 6) presents the overburden data with the overburden thickness as the parameter instead of line energy. This is a more dramatic illustration of the relative effect of overburden for different line energies.

The next series of figures (Figs. 7-9) show the effect of porosity on the signal flux. The porous fraction is assumed to be water filled. Figure 7 indicates about a 20-30% variation with increasing porosity. With a 10-cm overburden, however, as shown in Fig. 8, the variation increases to over a factor of two at the lower energies. Figure 9 depicts the variation in ratio of air flux (from airborne sources) to ground flux as a function of line energy for the different porosities. The ratio was computed assuming the sources in the air and ground were equal on a mass basis. To compute the actual ratio for a given problem, the ordinate value should be multiplied by the ratio of the source per gram of air to the source per gram of ground.

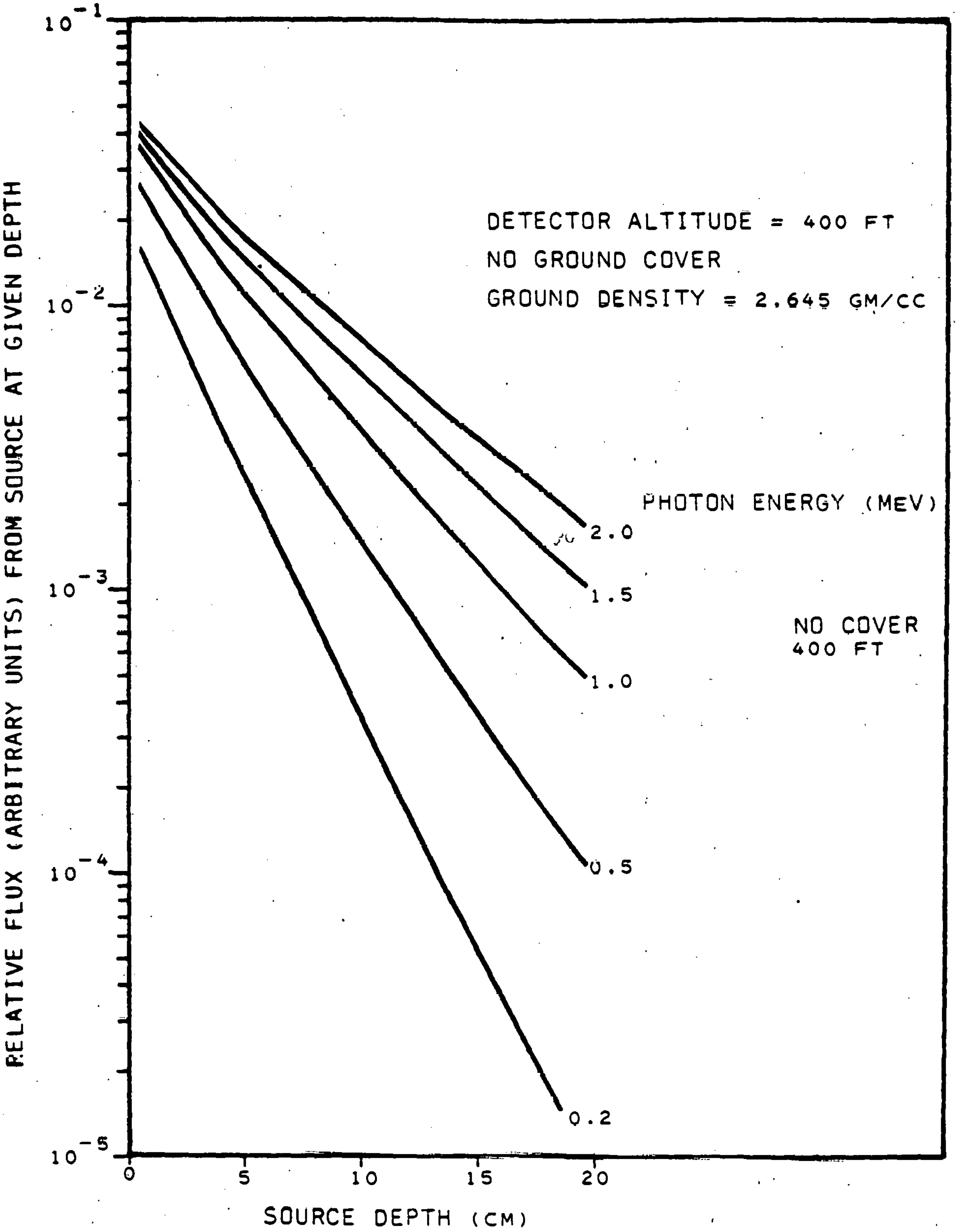

Figure 4. Variation in the signal flux as a function of depth of source in ground for line energies from 0.2 to 2.0 MeV.

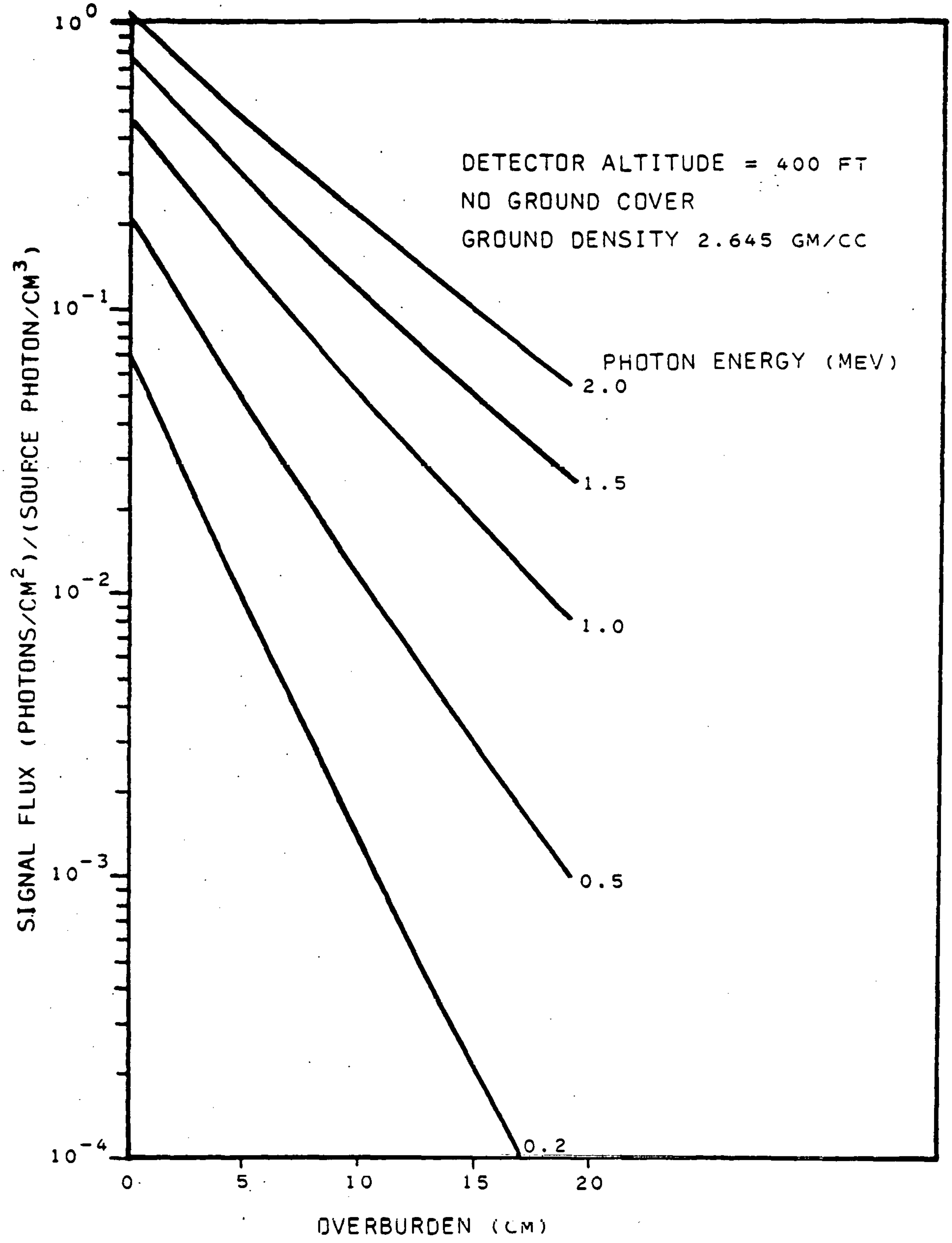

Figure 5. Signal flux as a function of overburden thickness for line energies from 0.2 to 2.0 MeV.

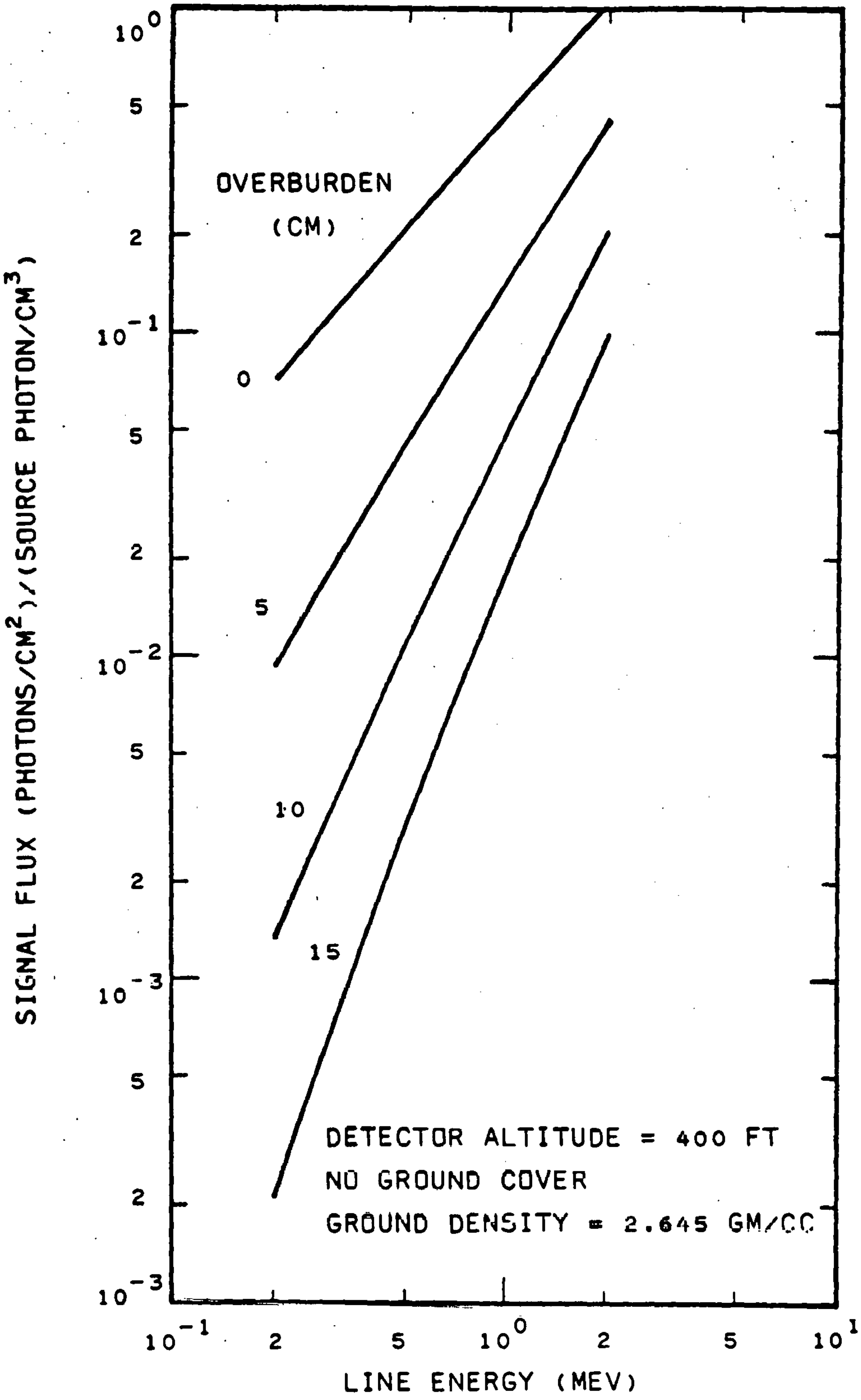

Figure 6. Signal flux as a function line energy for overburden thickness from 0 to 15 cm.

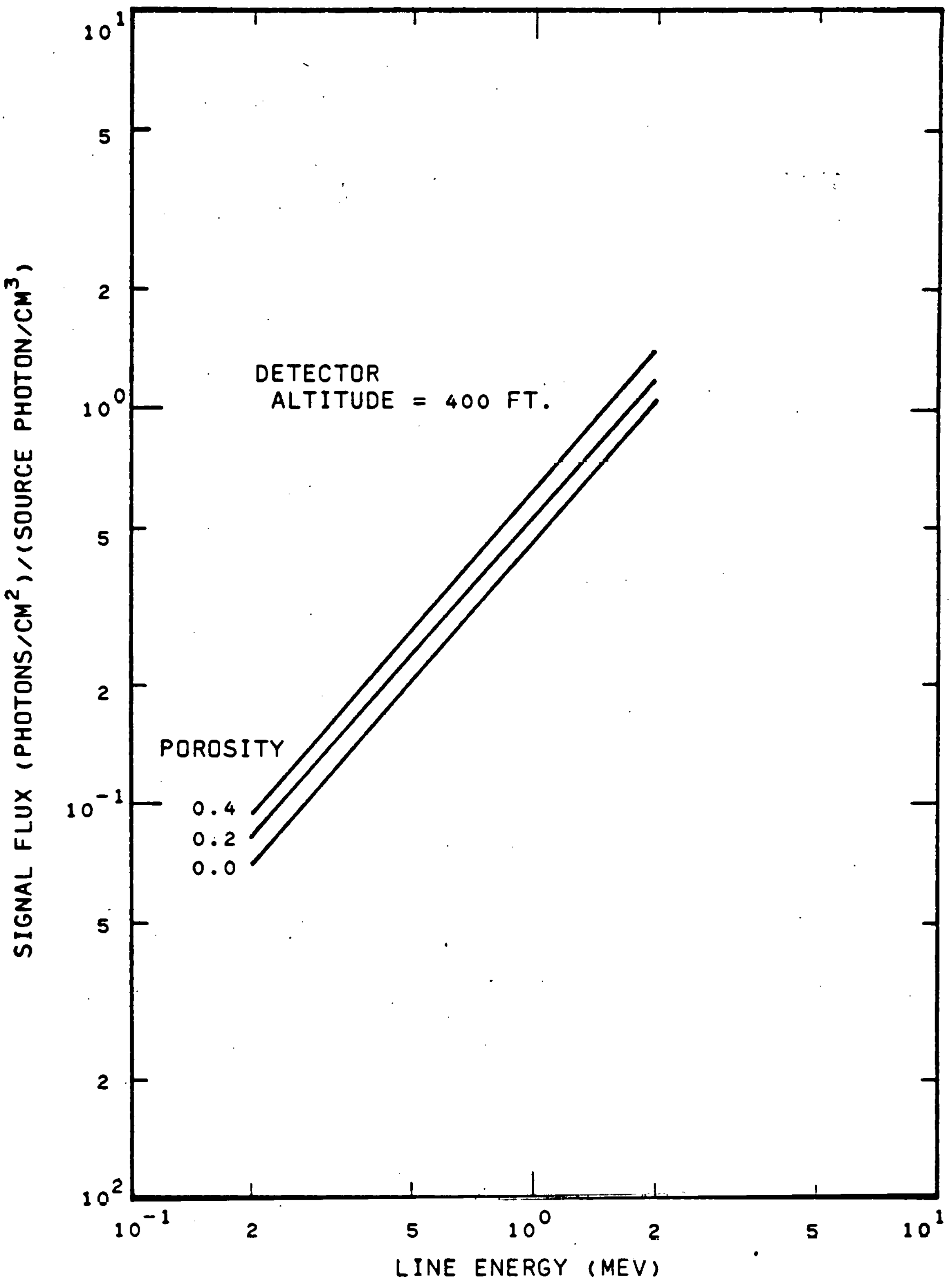

Figure 7. Signal flux as a function of line energy for water-filled porosity fractions of 0.0, 0.2 and 0.4

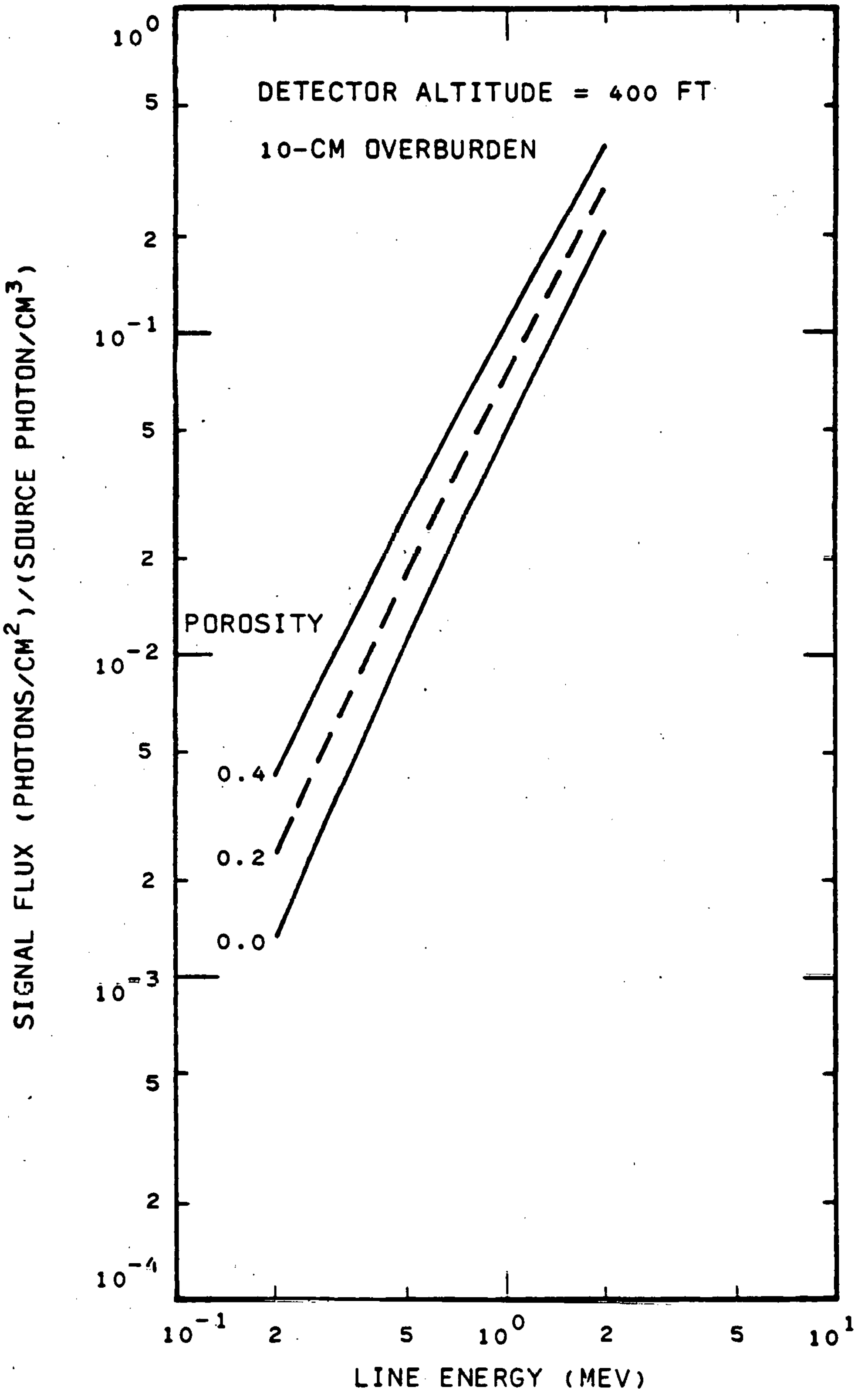

Figure 8. Signal flux as a function of line energy for a 10-cm overburden and water-filled porosity fractions of 0.0, 0.2 and 0.4.

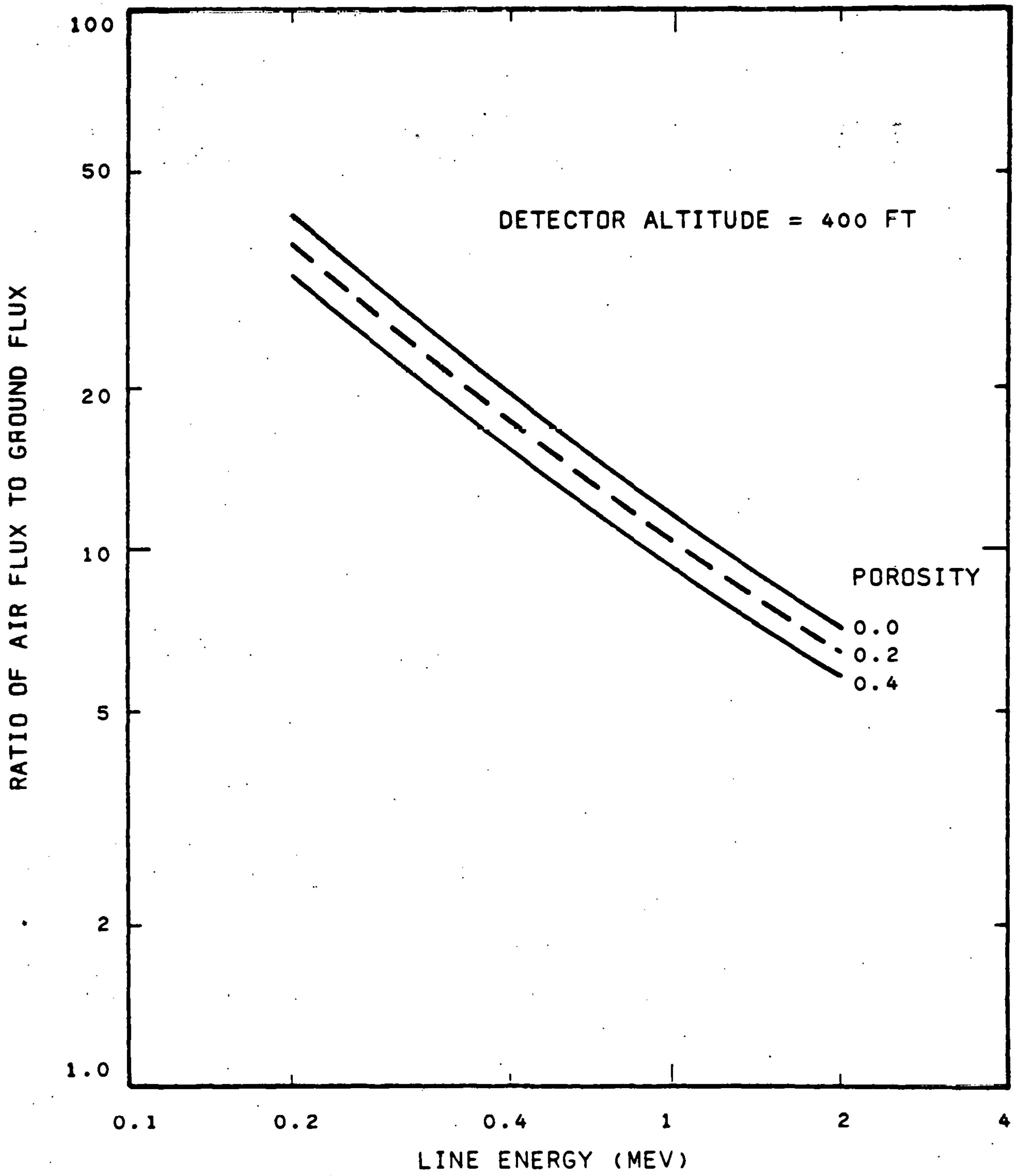

Figure 9. Ratio of the flux from air to ground as a function of line energy for water-filled porosity fractions of 0.0, 0.2 and 0.4.

The next set of figures (Figs. 10-12) analyze the effect of snow cover. Figure 10 shows the variation in the signal flux with line energy for different snow mass covers ranging from 0 to 100 gm/cm^2. The effect is quite pronounced, particularly for larger snow covers. Figure 11 shows the number of mean-free paths from the ground to the detector as a function of line energy for the snow covers studied. The last figure (Fig. 12) presents the ratio of the air flux to ground flux. The normalizations are the same as those discussed for Fig. 9. The snow cover appears to a significant parameter to consider in the airborne reconnaissance. For example, the signal is reduced by a factor of two at high energy and five at low energy for the 10 gm/cm^2 mass.

These graphical presentations illustrate examples of data which can be obtained from the ABRA code. We have not nearly exhausted all the possible results which could be obtained from ABRA. Additionally, we suggest that the accuracy and scope of ABRA be increased by the following improvements.

- Temperature, humidity, pressure and density variations of the atmosphere.
- Different ground compositions, including self-absorption effects of the high-Z ore and rock matrices.
- Variations in water content with depth in rock.
- Finite ore bodies in both radius and depth.
- Flight speed parameters.
- Terrain variations.
- Anisotropic vegetation (that is, forests).
- Angular variation in the signal flux at the detector.

Data obtained from ABRA with these improvements will greatly facilitate the understanding of calibration test runs, the comparison of detailed transport calculations with reconnaissance data and the actual interpretation of reconnaissance data. The code would be fast-running on small computers and thus permit many, many parametric investigations with modest computer expenditure.

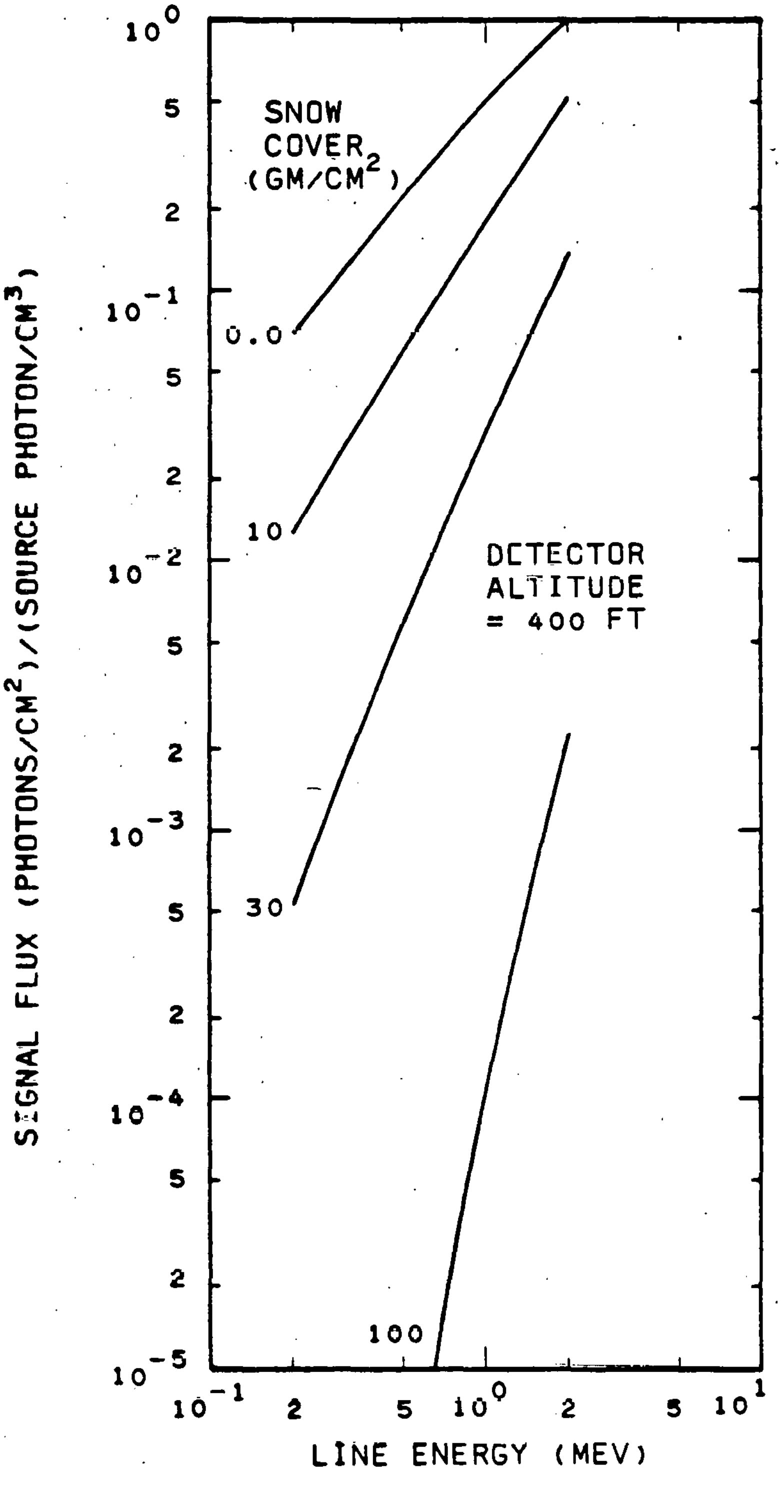

Figure 10. Signal flux as a function line energy for snow covers from 0.0 to 100 gm/cm^2.

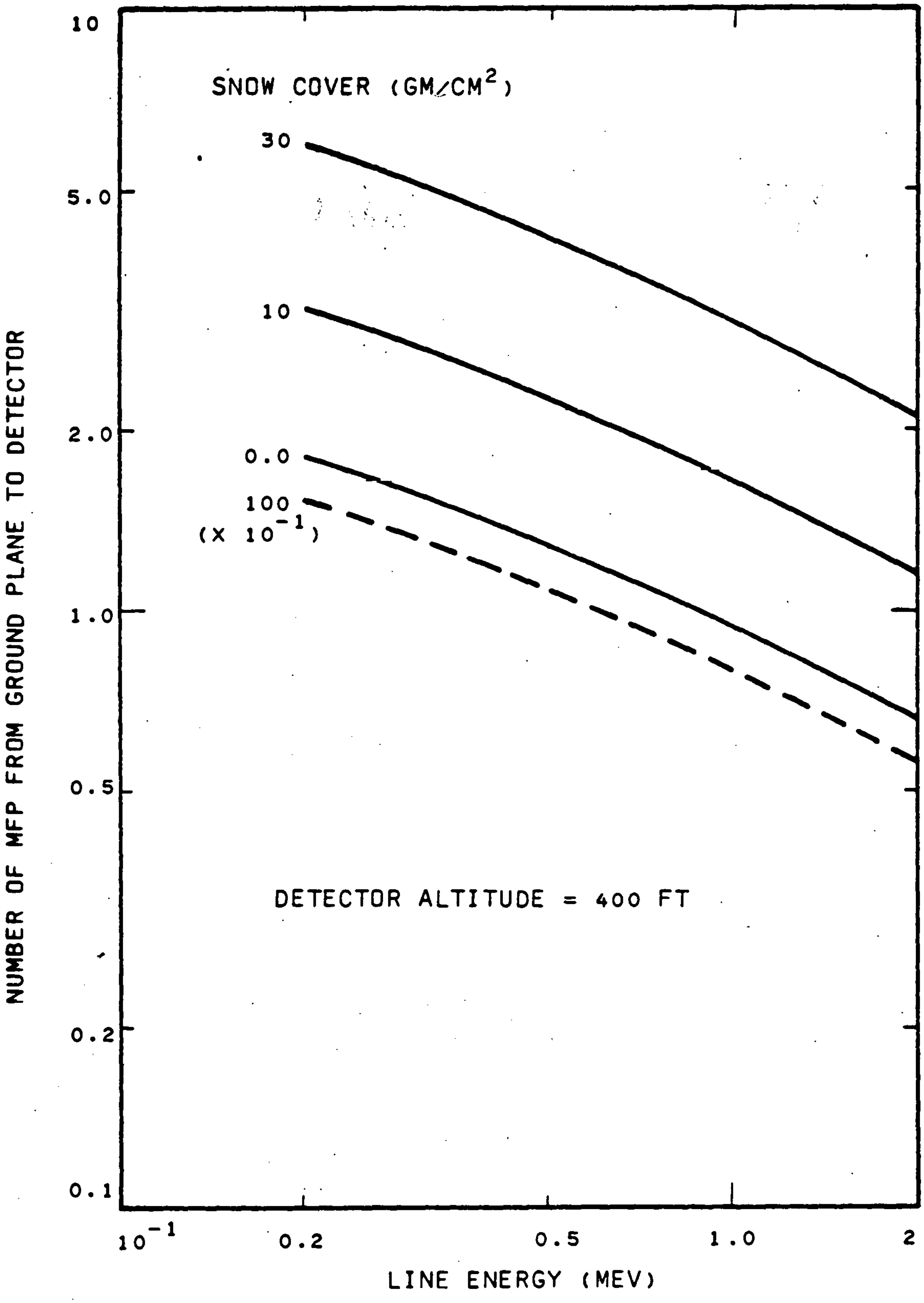

Figure 11. Number of mean-free paths (MFP) from ground plane to 400-ft. detector altitude as a function of line energy for snow covers from 0 to 100 gm/cm^2.

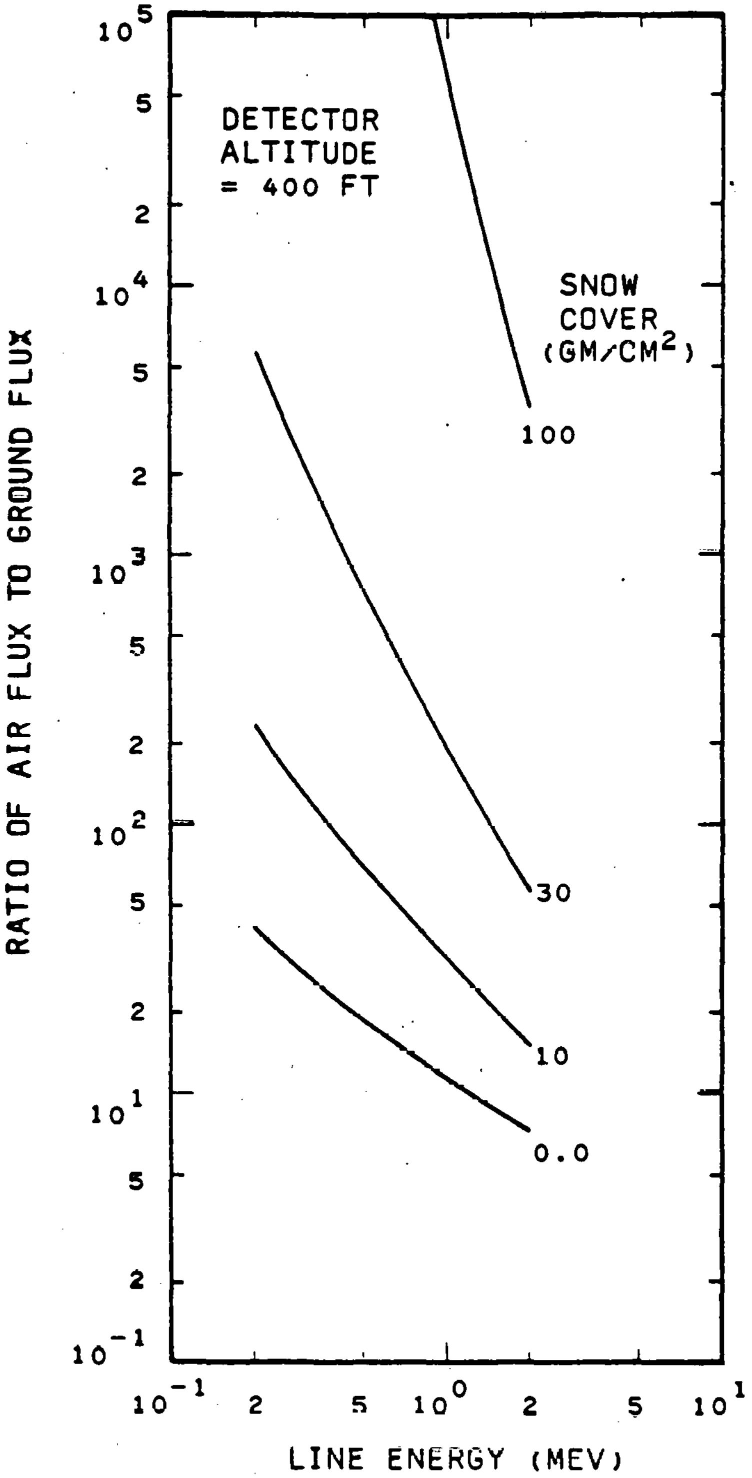

Figure 12. Ratio of air flux to ground flux as a function of line energy for snow cover from 0 to 100 gm/cm^2.

APPENDIX A

CALCULATION OF THE UNSCATTERED (SIGNAL) FLUX FOR DISCRETE GAMMA-RAY LINES FROM AIRBORNE AND GROUND SOURCES FOR AN AIRBORNE DETECTOR

W. A. Woolson

December 7, 1976

The problem addressed here is to calculate the uncollided flux or signal flux from discrete gamma-ray lines from ground and airborne sources. The model for the calculations is depicted in Figure 1. A detector is positioned at distance h_d above the ground plane. A ground cover of height, h_c, exists. Total cross sections at the energy of the gamma-ray line for air, cover and ground are Σ_A, Σ_c and Σ_g respectively. The sources of radiation are uniformly distributed in the air and ground. The uncollided flux calculations include attenuation in the air, ground cover and ground. The basic flux equations are given in Table 1. The complete, detailed derivation is presented in Appendix B. The exponential integral $E_2(X)$ in the equations can be found in many tabulations and graphical presentations. Additional calculations of interest are given in Table 2.

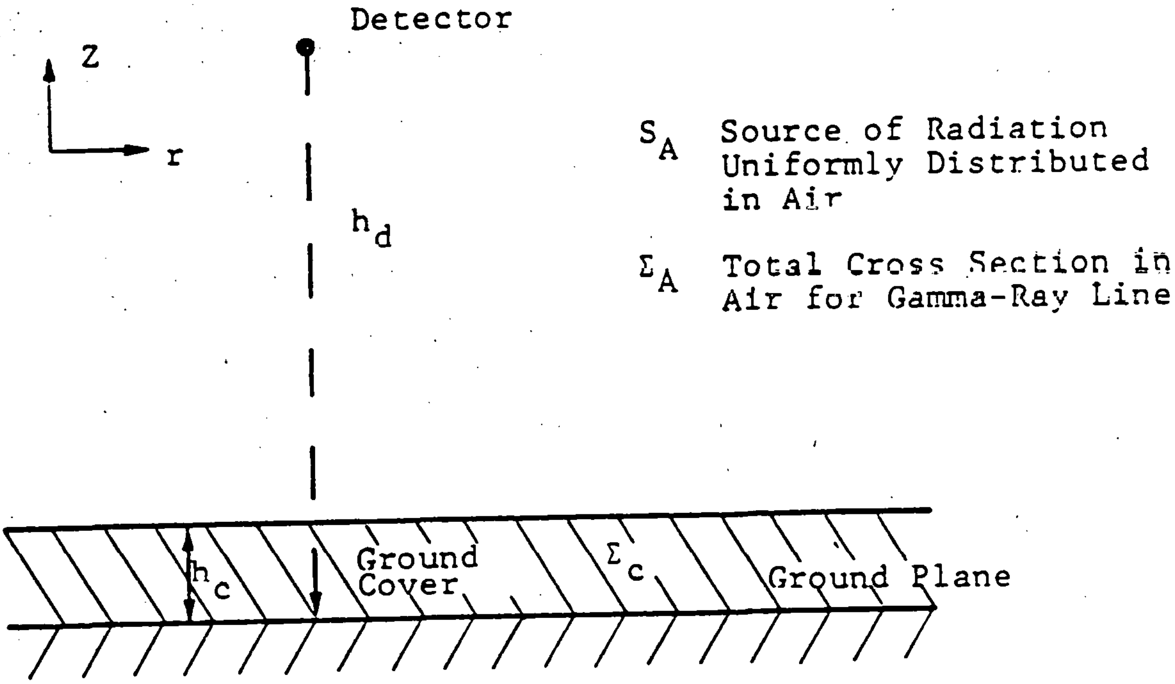

S_A Source of Radiation Uniformly Distributed in Air

Σ_A Total Cross Section in Air for Gamma-Ray Line

S_g Source of Radiation Uniformly Distributed in Ground

Σ_g Total Cross Section for Gamma-Ray Line in Source

Figure 1. Calculational Configuration.

Table 1. Equations for Uncollided Flux

Case	Air Source	Ground Source
No ground cover ($h_i = 0$)	$\phi_A = \frac{S_A}{2\Sigma_A}\left[2 - E_2(\Sigma_A h_d)\right]$	$\phi_g = \frac{S_g}{2\Sigma_g}\left[E_2(\Sigma_A h_d)\right]$
With ground cover	$\phi_A = \frac{S_A}{2\Sigma_A}\left[2 - E_2\left[\Sigma_A(h_d - h_c)\right]\right]$	$\phi_g = \frac{S_g}{2\Sigma_g}\left[E_2\left[\Sigma_c h_c + \Sigma_A(h_d - h_c)\right]\right]$

where $E_2(X) = \int_1^\infty \frac{e^{-Xt}}{t^2}\,dt$

Table 2. Additional Flux Equations with Ground Cover

Flux from air source above detector: $\frac{S_A}{2\Sigma_a}$

Flux from air source below detector: $\frac{S_A}{2\Sigma_a}\left[1-E_2\left[\Sigma_A(h_d-h_c)\right]\right]$

Flux from air source on plane at distance, h, from detector : $\frac{S_A}{2}\left[E_1(\Sigma_A h)\right]$

Flux from air source in band of thickness, t, at distance, h, from detector : $\frac{S_A}{2\Sigma_a}\left[E_2(\Sigma_a h) - \left(E_2\ \Sigma_a(h+t)\right)\right]$

Flux from source plane in ground a distance h_g below surface : $\frac{S_g}{2}\left[E_1\left(\Sigma_a(h_d-h_c) + \Sigma_c h_c + \Sigma_g h_g\right)\right]$

Flux from source band in ground a distance h_g below surface of thickness t :

$$\frac{S_g}{2\Sigma_g}\left[E_2\left(\Sigma_a(h_d-h_c) + \Sigma_c h_c + \Sigma_g h_g\right) - E_2\left(\Sigma_a(h_d-h_c) + \Sigma_c h_c + \Sigma_g(h_g+t)\right)\right]$$

where $E_N(X) = \int_1^\infty \frac{e^{-Xt}}{t^N}\,dt$

APPENDIX B

DERIVATION OF EQUATIONS FOR UNCOLLIDED FLUX

We use cylindrical coordinates with altitude corresponding to the Z coordinate. Note that the cross sections vary only with Z. The geometry for the calculation is shown in Figure 2. We also assume the source strength S (photons/sec/cm^3) varies only with Z.

The uncollided flux from differential volume element $dV = r dr d\phi dZ$ is (Fig. 2)

$$\phi(r,\phi,Z)dV = \frac{\exp\left[-\int_0^Z \Sigma(h)dh \cdot \frac{(r^2+Z^2)^{\frac{1}{2}}}{Z}\right]}{4\pi(r^2+Z^2)} S(Z) r dr d\phi dZ \ .$$

Let

$$\alpha(Z) = \frac{1}{Z}\int_0^Z \Sigma(h)dh$$

and

$$u = \alpha(Z)(r^2+Z^2)^{\frac{1}{2}} \ .$$

Now

$$du = \alpha(Z)(r^2+Z^2)^{-\frac{1}{2}} \cdot r dr \ .$$

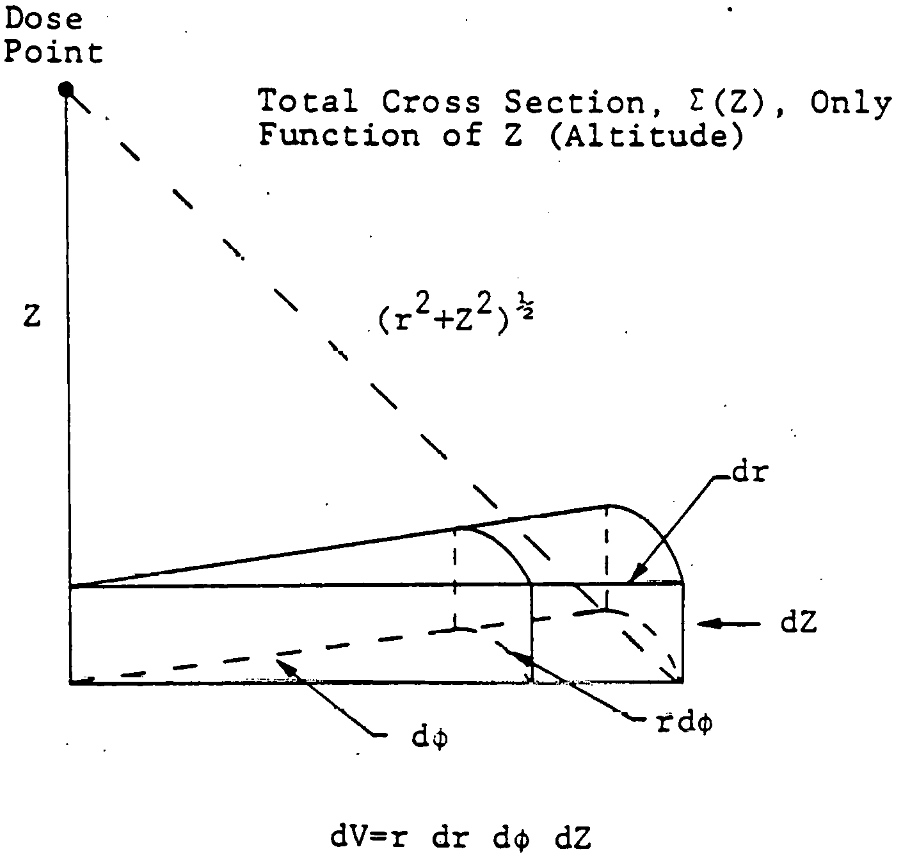

Figure 2. Uncollided Flux Calculation.

Making substitutions for $\alpha(Z)$ and u, then integrating over ϕ, then r, we get:

$$\phi(Z)dZ = \int_0^\infty rdr \int_0^{2\pi} d\phi \ \phi(r,\phi,Z)dZ$$

$$= \frac{S(Z)dZ}{2} \int_{\alpha(Z)\cdot Z}^{\infty} \frac{e^{-u}}{u} du$$

To perform the integration over "Z", we partition the integration over "Z" bands of constant cross section and source. Let one of those bands have limits from $Z = h_i$ to $Z = h_{i+1}$ with source S_i and cross section Σ_i. Define $b_i = h_{i+1} - h_i$; then

$$\alpha(Z)Z = \int_0^Z \Sigma(h)dh$$

$$= \sum_{j=1}^{i-1} \Sigma_j b_j + \Sigma_i(Z - h_i)$$

Let

$$\beta(Z) = \alpha(Z)\cdot Z \quad ,$$

then

$$d\beta(Z) = \Sigma_i dZ \ .$$

Then we have for the ith band:

$$\phi_i = \int_{h_i}^{h_{i+1}} \phi(Z)\,dZ = \frac{S_i}{2\Sigma_i} \int_{m_{i-1}}^{m_i} d\beta \int_{\beta}^{\infty} \frac{e^{-u}}{u}\,du$$

where

$$m_i = \sum_{j=1}^{i} \Sigma_j b_j \quad .$$

Now

$$\phi_i = \frac{S_i}{2\Sigma_i} \left[\int_{m_{i-1}}^{\infty} d\beta \int_{\beta}^{\infty} \frac{e^{-u}}{u}\,du - \int_{m_i}^{\infty} d\beta \int_{\beta}^{\infty} \frac{e^{-u}}{u}\,du \right]$$

To evaluate the integrals, we make one more substitution; let

$$X = u/\beta \quad .$$

Then

$$\int_{m}^{\infty} d\beta \int_{\beta}^{\infty} \frac{e^{-u}}{u}\,du = \int_{m}^{\infty} d\beta \int_{1}^{\infty} \frac{e^{-\ X}}{X}\,dX = \int_{1}^{\infty} \frac{dX}{X} \int_{m}^{\infty} d\beta e^{-\beta X}$$

$$= \int_{1}^{\infty} \frac{dX}{X^2} \cdot e^{-mX} = E_2(m) \quad .$$

Finally, then our desired result is

$$\phi_i = \frac{S_i}{2\Sigma_i}\left[E_2(m_{i-1}) - E_2(m_i)\right]$$

where $E_2(m)$ is the exponential integral:

$$E_2(m) = \int_1^\infty \frac{dX}{X^2} e^{-mX} \quad .$$

Note that

$$E_2(0) = 1$$

and

$$E_2(\infty) = 0.$$

From the equation above, all results in Table 1 can be derived. For example, the air source with no ground cover is

$$\phi_A = \frac{S_A}{2\Sigma_A}\left[E_2(0) - E_2(\Sigma_A h_d)\right] + \frac{S_A}{2\Sigma_A}\left[E_2(0) - E_2(\infty)\right]$$

$$\phi_A = \frac{S_A}{2\Sigma_A}\left[2 - E_2(\Sigma_A h_d)\right]$$

THIS PAGE
WAS INTENTIONALLY
LEFT BLANK

INTERIM REPORT
SPECTRAL ENHANCEMENT OF
11½" x 4" NaI(Tl) DATA

Submitted to

Bendix Field Engineering Corporation

May 1977

By

J. Reed
W. Bohannon
D. Shreve

THIS PAGE
WAS INTENTIONALLY
LEFT BLANK

1. INTRODUCTION

This report briefly describes the progress made in applying the unfolding code MAZE to low statistics data from an 11½" x 4" NaI(Tℓ) detector. The motivation, theory and response functions generated for this problem are described in the report "Gamma-Ray Spectrum Enhancement."(1) This report presents the results of the application of the code MAZE to data taken with low to good statistics using an 11½" x 4" NaI(Tℓ) detector. Additionally, the code performance was tested using simulated background data.

---

(1) "Gamma-Ray Spectrum Enhancement," J.H. Reed and G.M. Reynolds, SAI Report No. SAI-77-518-LJ.

THIS PAGE

WAS INTENTIONALLY

LEFT BLANK

2. EXPERIMENTAL DATA

Data were taken of ambient room background using a single 11½" x 4" NaI(Tℓ) detector. A number of spectra were obtained at each of several counting times ranging from 9-sec to 900-sec. These correspond to the approximate counting statistics found in 1-sec to 100-sec of airborne data obtained using 8 parallel 11½" x 4" detectors. Table 1 lists the number of independent measurements made for each level of counting statistics. Figures 1 through 5 show samples of the data obtained at five (5) different statistical levels ranging from the equivalent of 20-sec to 1-sec of airborne data. Calibration spectra using point sources of ^{137}Cs, ^{88}Y, ^{60}Co, ^{113}Sn, ^{65}Zn and ^{228}Th were measured before and after the series of background measurements to establish the gain of the system and the resolution of the photopeak as a function of gamma-ray energy. Details of the detector operation and performance are described in the report "Gamma-Ray Spectrum Enhancement."(1)

Table 1. Background Gamma-Ray Spectra Obtained With 11½" x 4" NaI(Tℓ)

Equivantent Airborne Counting Time (sec)	Number of Spectra per Statistical Level
100	1
20	2
10	3
5	5
2	8
1	10

Figure 6 shows a high resolution Ge(Li) spectrum of the room background which establishes which gamma-rays are actually present in the spectrum.

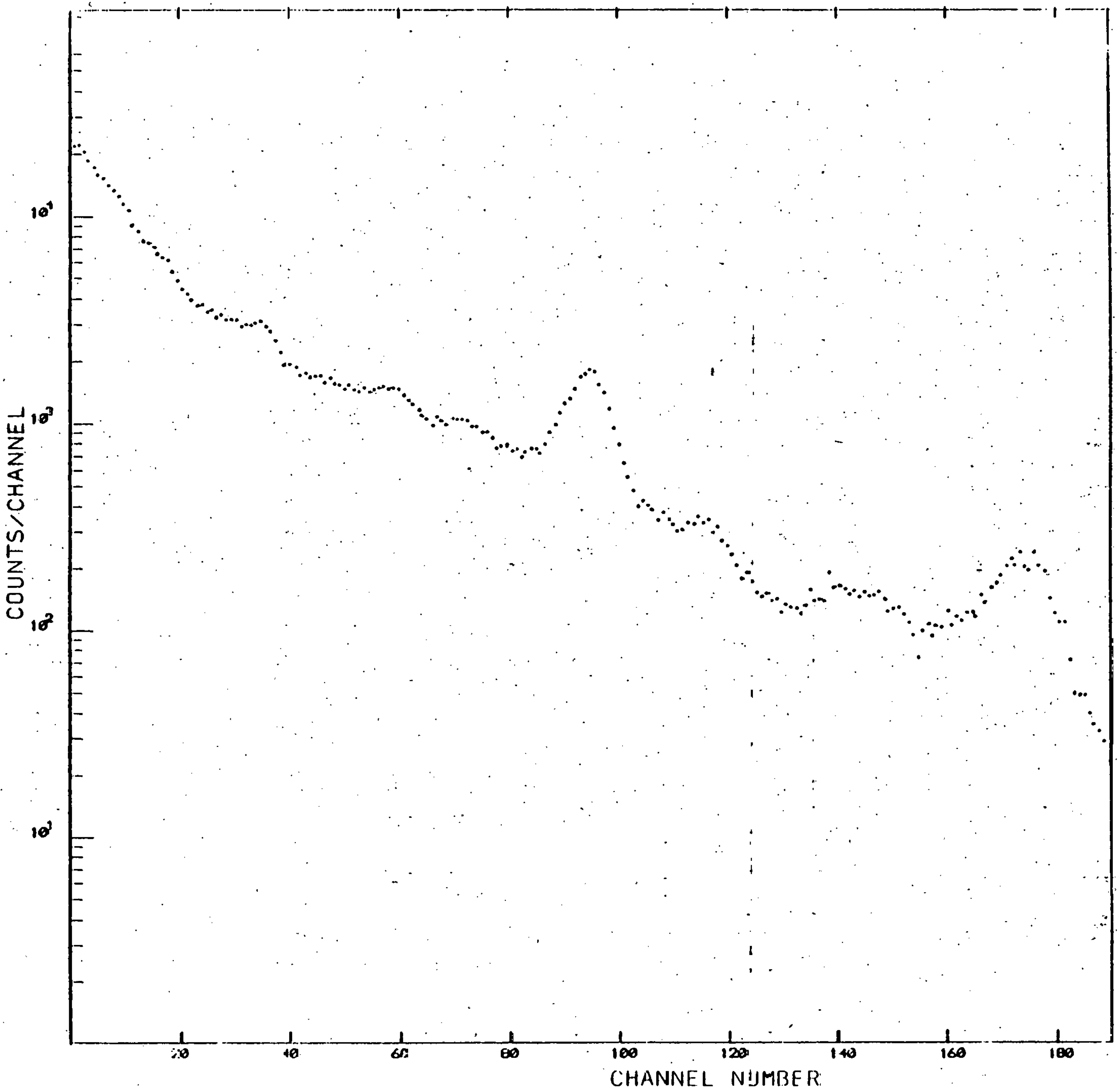

Figure 1. 11½" x 4" Data - Equivalent to "20-sec" Airborne Data

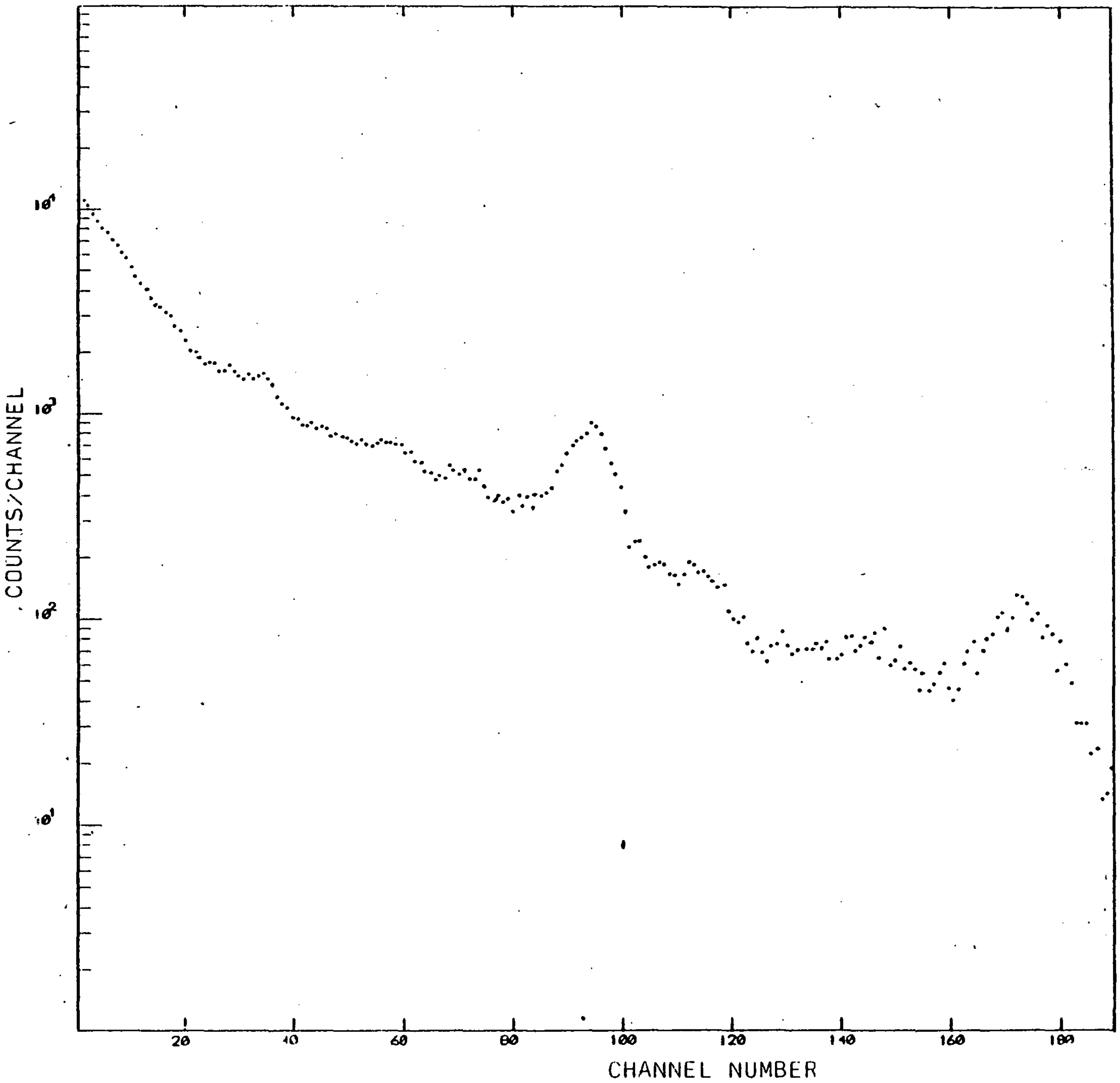

Figure 2. 11½" x 4" Data - Equivalent to "10-sec" Airborne Data

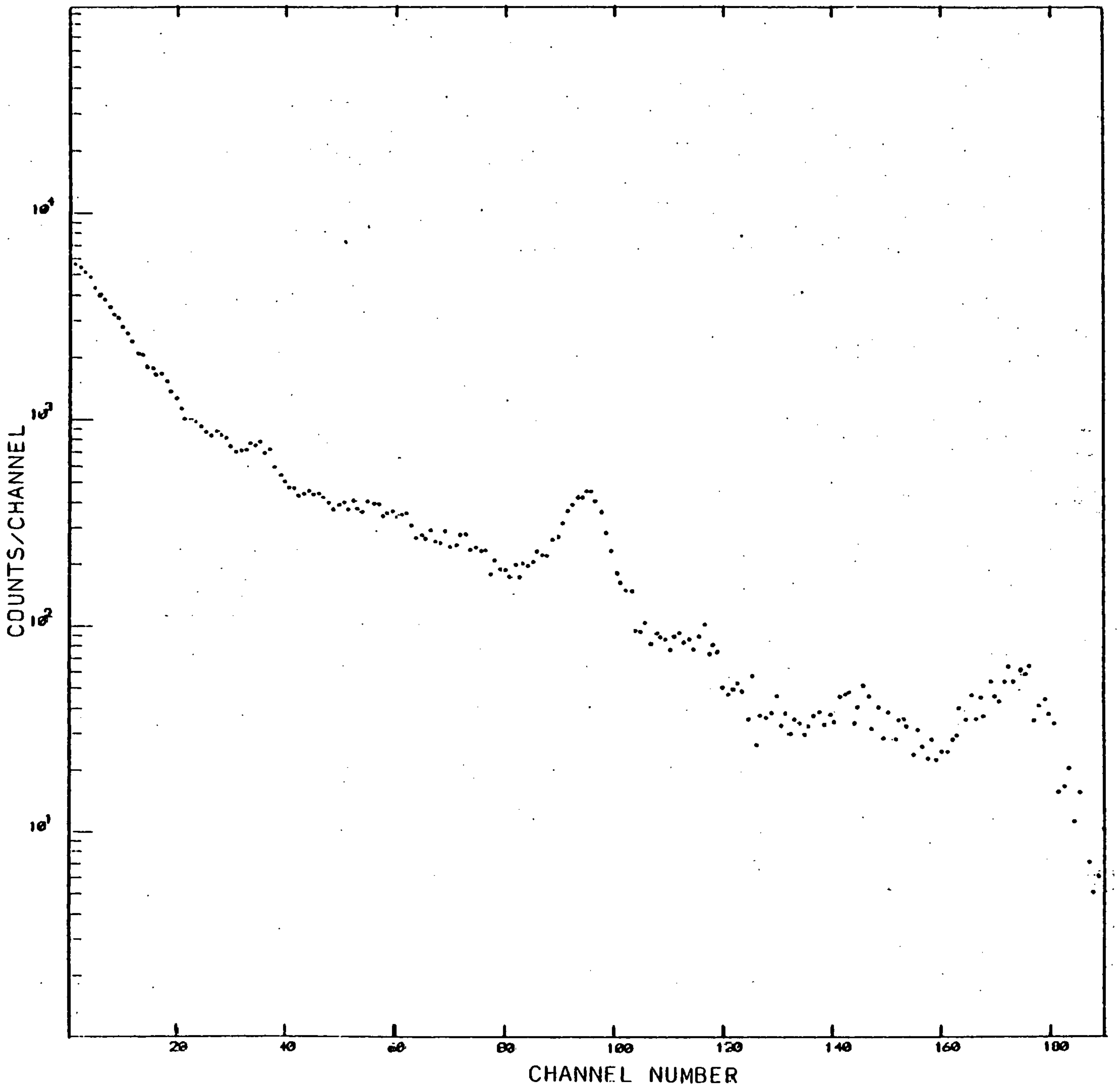

Figure 3. 11½" x 4" Data - Equivalent to "5-sec" Airborne Data

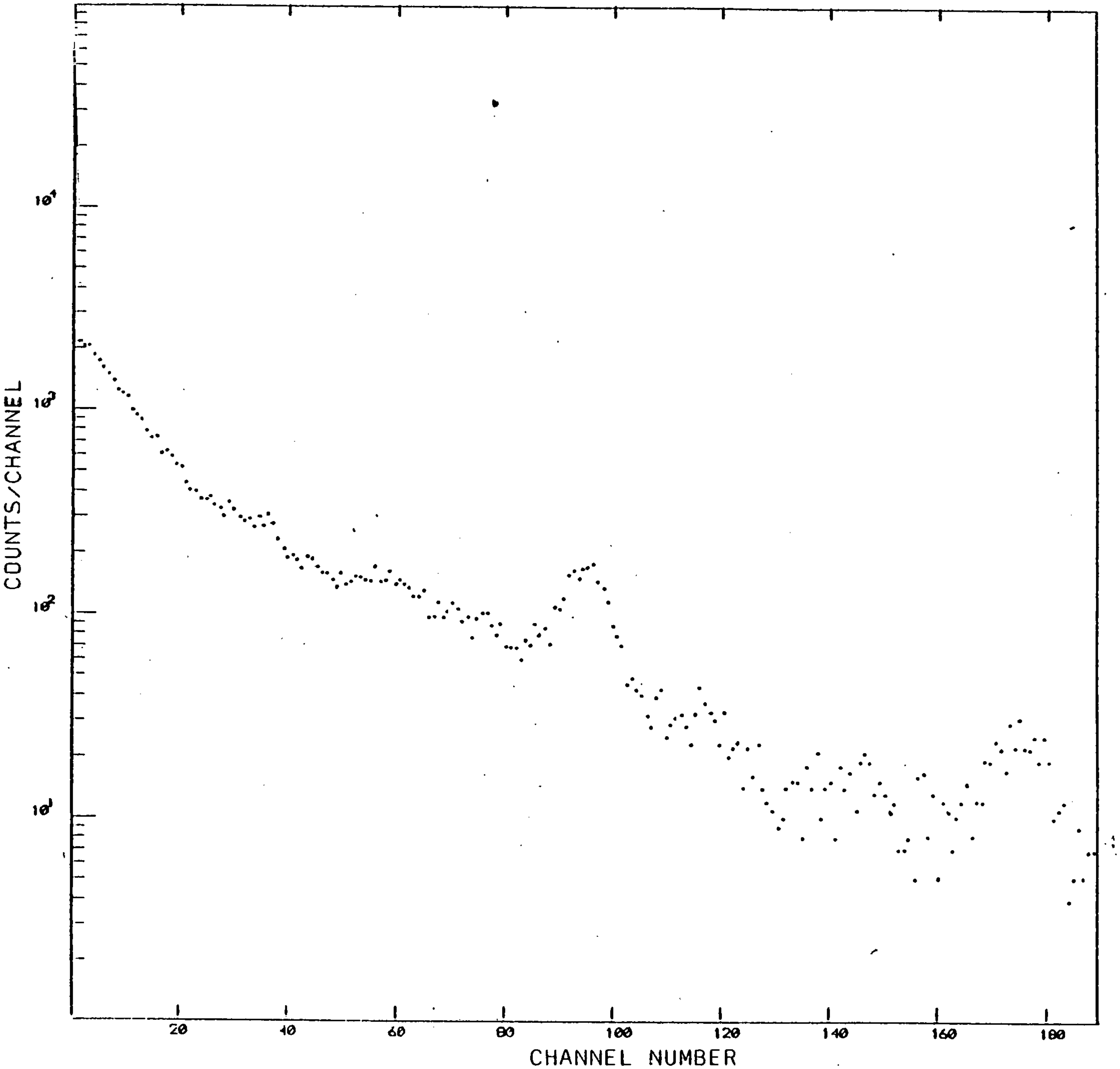

Figure 4. 11½" x 4" Data - Equivalent to "2-sec" Airborne Data

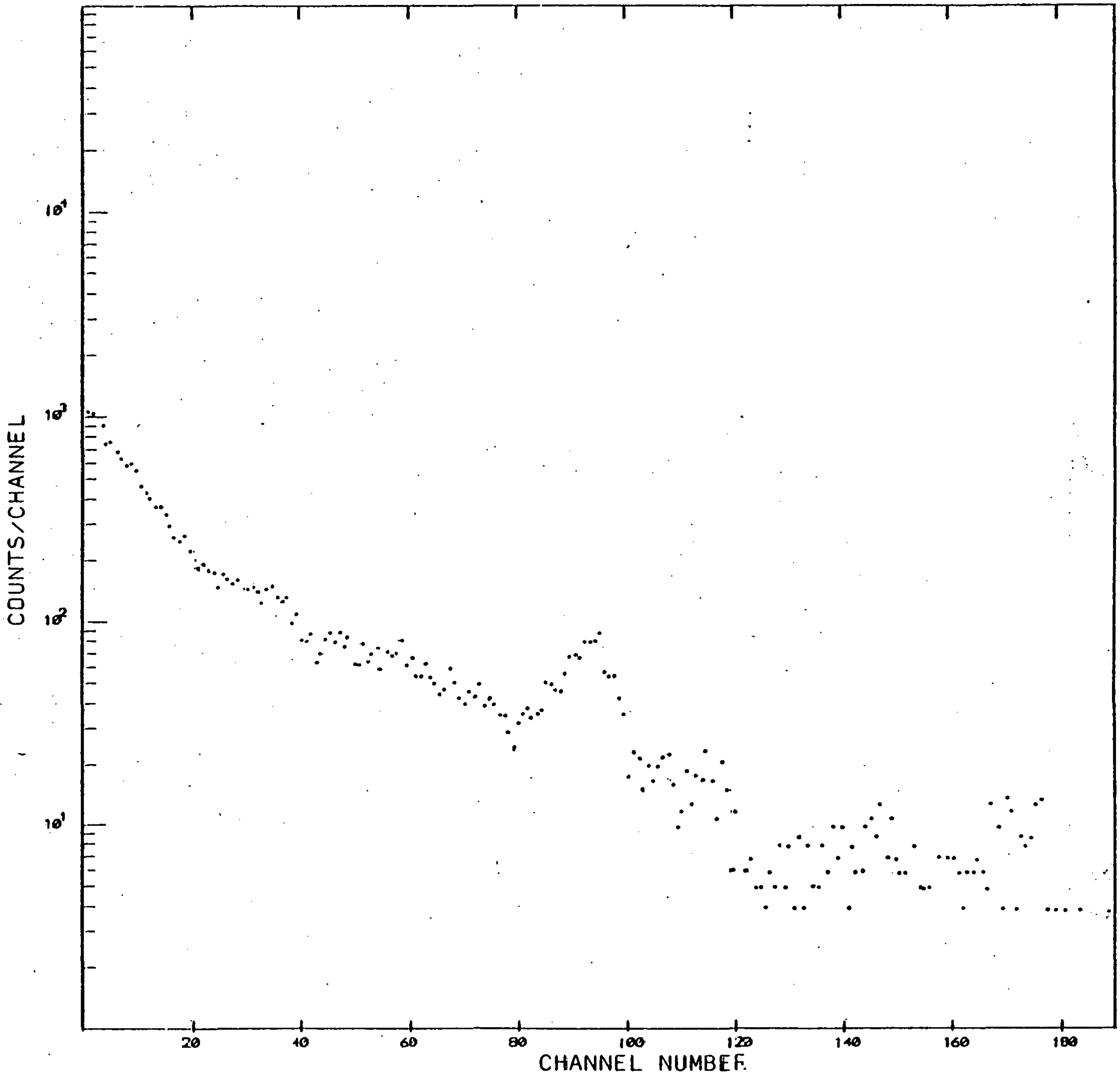

Figure 5. 11½" x 4" Data - Equivalent to "1-sec" Airborne Data

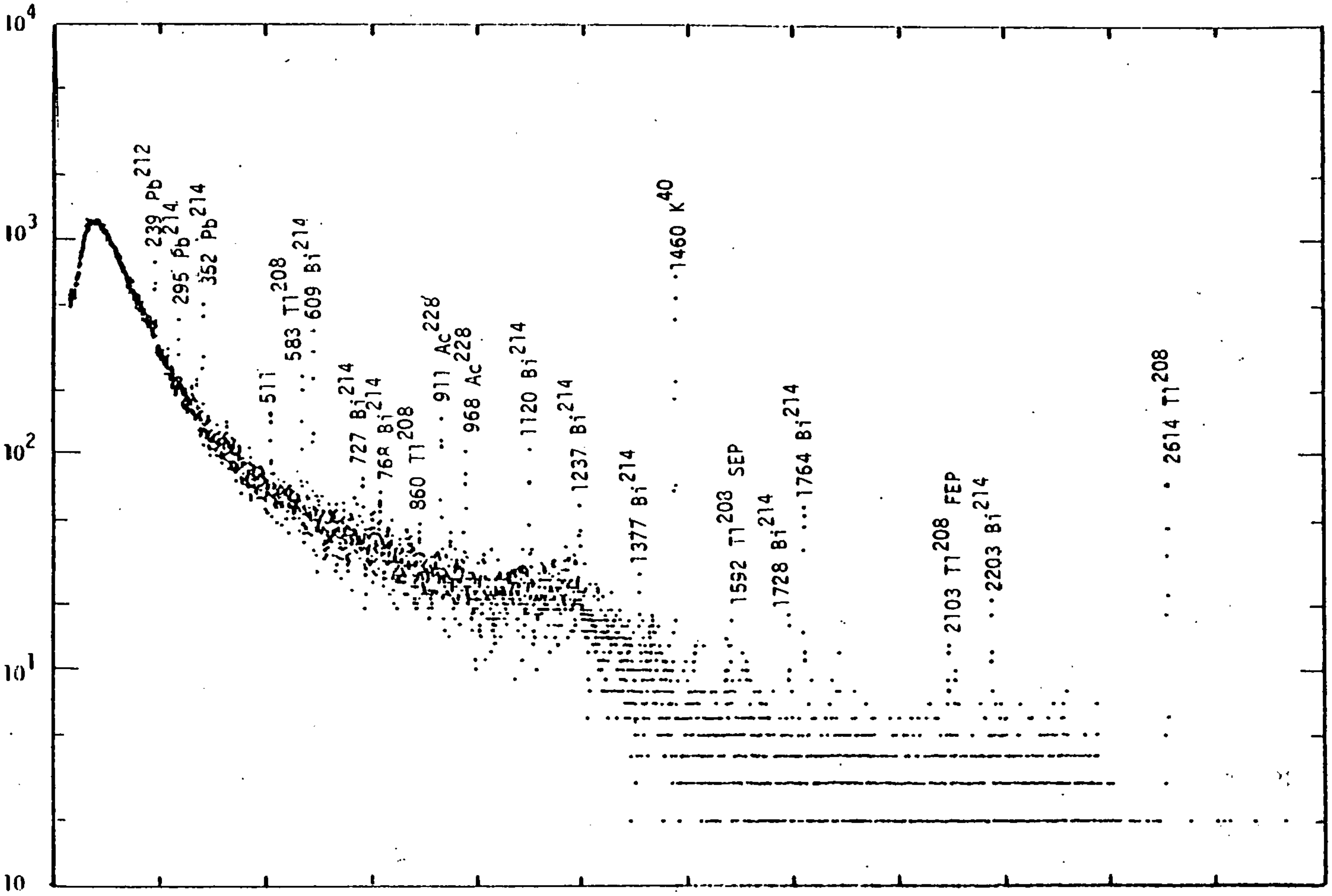

FIGURE 6. 2400 Seconds Background Ge(Li)

THIS PAGE

WAS INTENTIONALLY

LEFT BLANK

3. SIMULATED DATA

The present study is being carried out to test the use of the unfolding code MAZE on low resolution NaI(Nℓ) data. Preliminary unfolding of data from a 11½" x 4" NaI detector seemed to indicate some problems.

There are several sources of uncertainties in unfolding actual data and it was not known which might be causing the problem. In particular, uncertainties could come from

- the calculated response functions
- the code itself

Further, the actual gamma-ray spectrum incident on the detector was not known. The discrete part had been measured using a Ge(Li) detector but the continuum portion was unknown. (The Compton response of the Ge(Li) detector would have to be removed to obtain the continuum from the Ge(Li) data.) In order to remove the uncertainties introduced by the response function and to know the magnitude and shape of the continuum a test spectrum was generated.

This test spectrum was designed to be similar to the room background spectra which were to be analyzed. Figure 7 shows the assumed input gamma-ray spectrum and simulated data. The gamma-ray intensities and energies were determined from the Ge(Li) data (see Figure 6). The log of the continuum was assumed to be given by a sum of Legendre polynomials (up to P_4) which gave an approximate fit to an assumed continuum seen in the Ge(Li) data.

This test gamma-ray spectrum was then folded with the calculated 11½" x 4" NaI detector response function to produce an error free data spectrum. Statistical errors were simulated using a random number generator with a normal distribution for numbers greater than 20 and a Poisson distribution for numbers less than 20. The simulated data shown in Figure 7 correspond to a total of 10^5 counts.

4. DATA ANALYSIS

4.1 ANALYSIS OF TEST SPECTRUM

The test spectrum was analyzed using MAZE. The first results were disappointing. The code gave a continuum that was considerably lower than the true continuum at low energies and introduced spurious peaks. Figure 8 shows an example of the unfolded spectrum using the older version of the code. Careful analysis of coding uncovered an error in the continuum generation part of the code. Correction of this error improved the performance of the code somewhat but the continuum was still being under estimated at the low energies. Further work uncovered no other errors but suggested that the constraints in the code on the shape of the continuum were too severe. These constraints were relaxed and the code was able to produce an accurate representation of the shape of the input continuum. Figure 9 shows the results of unfolding the test spectrum using the modified version of the code. The continuum is seen to be a good representation of the input continuum (see Figure 7). The unfolded peaks are also in good agreement with the input lines. The numbers above the peaks give the ratio of the area of the unfolded peaks relative to the input intensity. The areas are seen in most cases to be within 10% of the input data. There are cases where doublets are not separated in the unfolded spectra (e.g., the unfolded peak at about 900 keV corresponds to three input lines) and the ratio of the area of this peak to the sum of the three input intensities is about 30% low.

The above analysis seems to indicate that if the actual input gamma-ray spectrum corresponds approximately to the constraints contained in the code (that is that the actual continuum can be approximated as a low order Legendre polynomial in log space) and if the detector response functions are known then the modified code will do a good job of extracting both peak and continuum information.

4.2 UNFOLDING OF 11½" x 4" NaI(Tℓ) DATA

The modified (and corrected) MAZNAI code has been applied to all 29 spectra listed in Table 1 in an effort to evaluate the effectiveness and reliability of the code in processing poor statistical data. A few of the MAZNAI processed spectra are presented in Figures 10 through 15.

Figure 10 shows the enhanced "20-sec" data. The curve marked "total" is the gamma-ray spectrum incident on the detector as calculated by MAZNAI (total of discrete plus continuum) and the smooth curve is the calculation continuum. In Figure 11 the "discrete" and "continuum" are plotted separately for this same spectrum. The prominent lines in the processed spectrum include the peaks that are of general interest, namely the 600 keV line (^{208}Tℓ + ^{214}Bi), the 1461 keV line (^{40}K), the 1.76 MeV line (^{214}Bi) and the 2.614 MeV line (^{208}Tℓ). Examples of the processed data at each of the poorer statistical levels are given in Figures 12 through 15. The major peaks are detectable even at the poorest statistical level. The energies assigned to the peaks in these figures is as determined by the MAZNAI code.

Now the question arises about the reliability of the peaks found by MAZNAI. As we see from the figures, at high statistical levels the unfolded peaks are very well defined. As the counting time is shortened the smaller peaks cannot be reliably extracted and the prominent peaks become less well defined. As we will see later the area of the 2.61 MeV line is often underestimated at the very poor statistical level. This may be due to an inaccurate estimate of the continuum (see Figure 15).

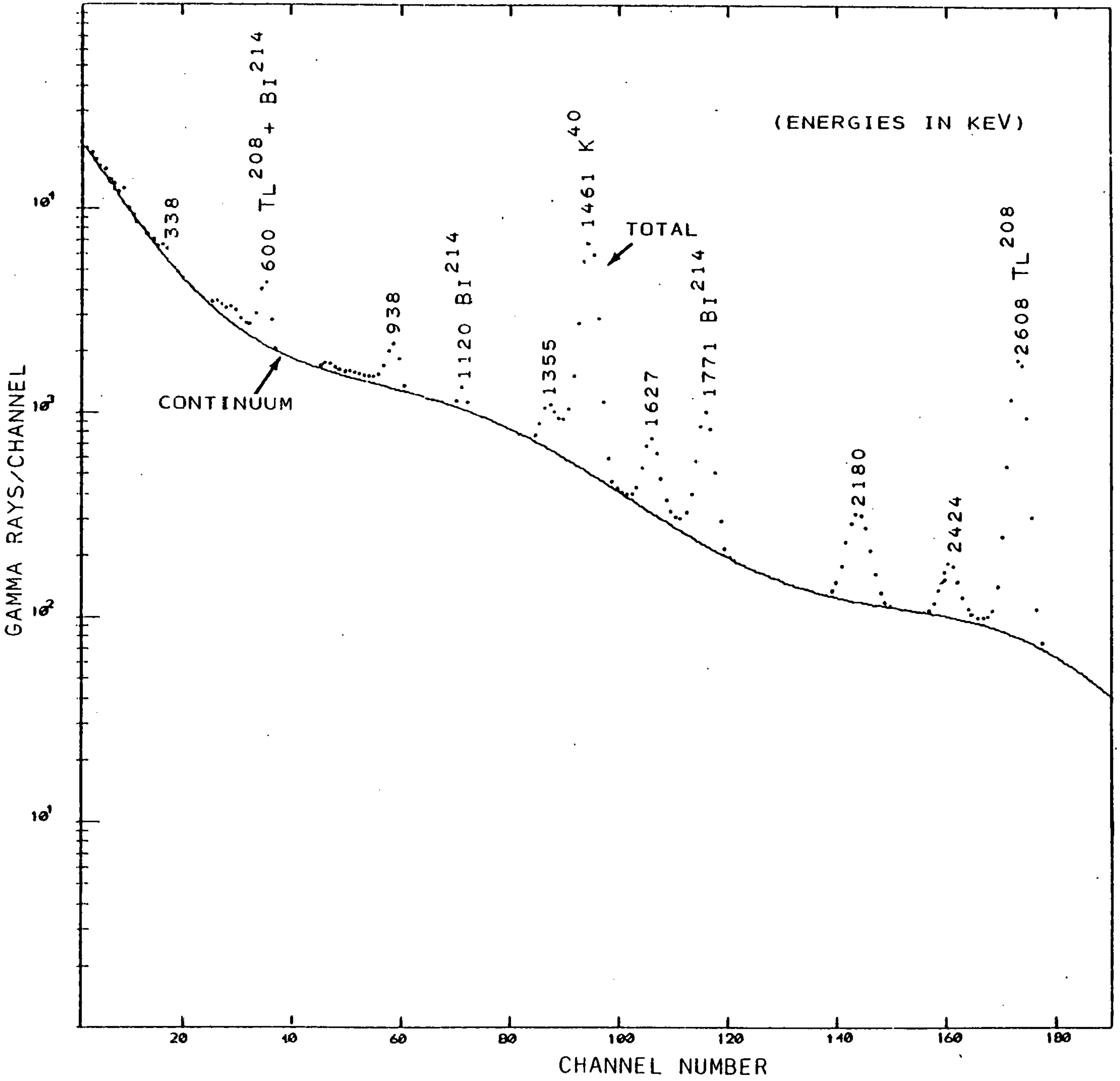

Figure 10. 11½" x 4" Enhanced Data - Equivalent to "20-sec" Airborne Data

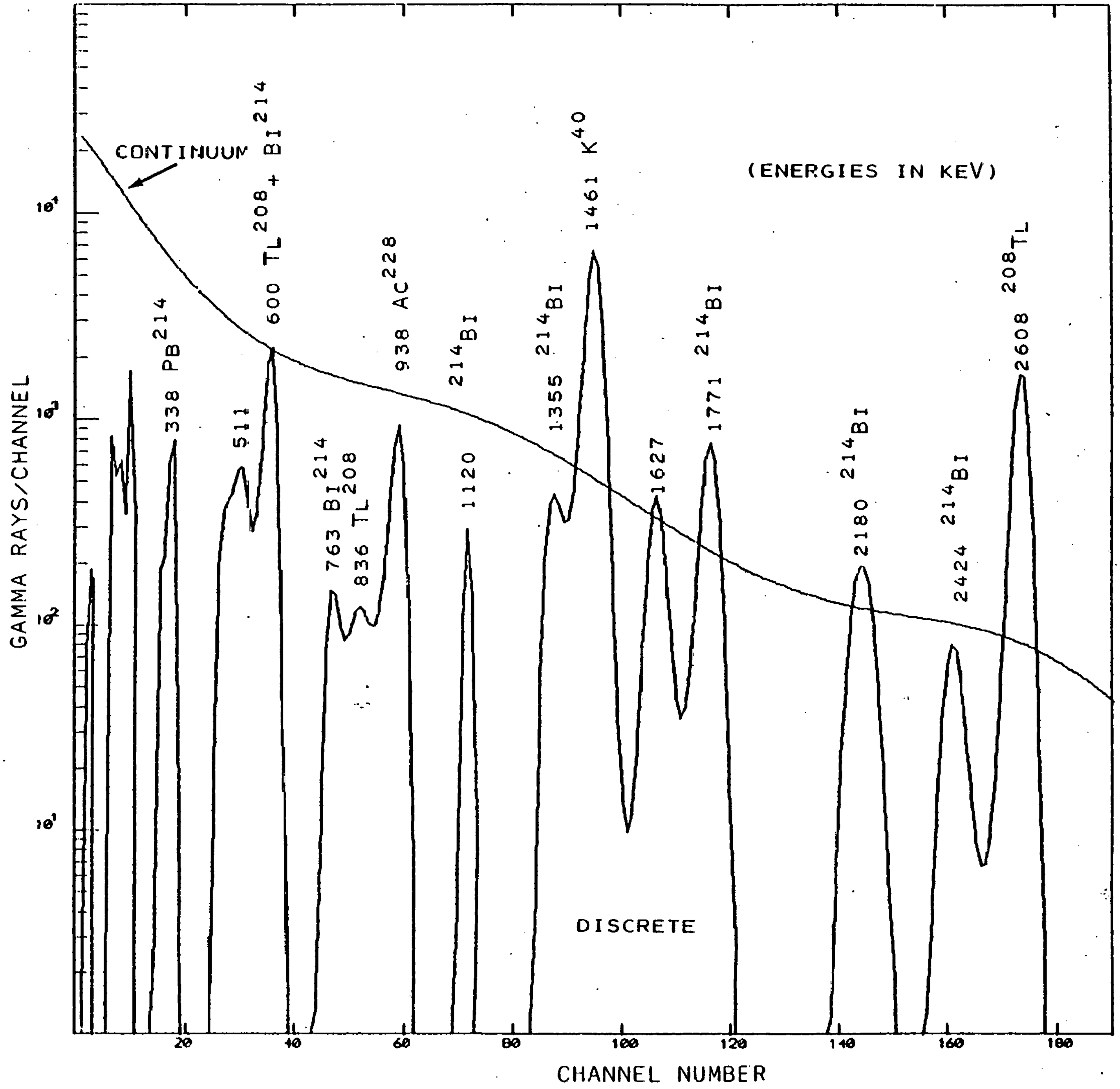

Figure 11. 11½" x 4" Enhanced Data - Discrete and Continuum - Equivalent to "20-sec" Airborne Data

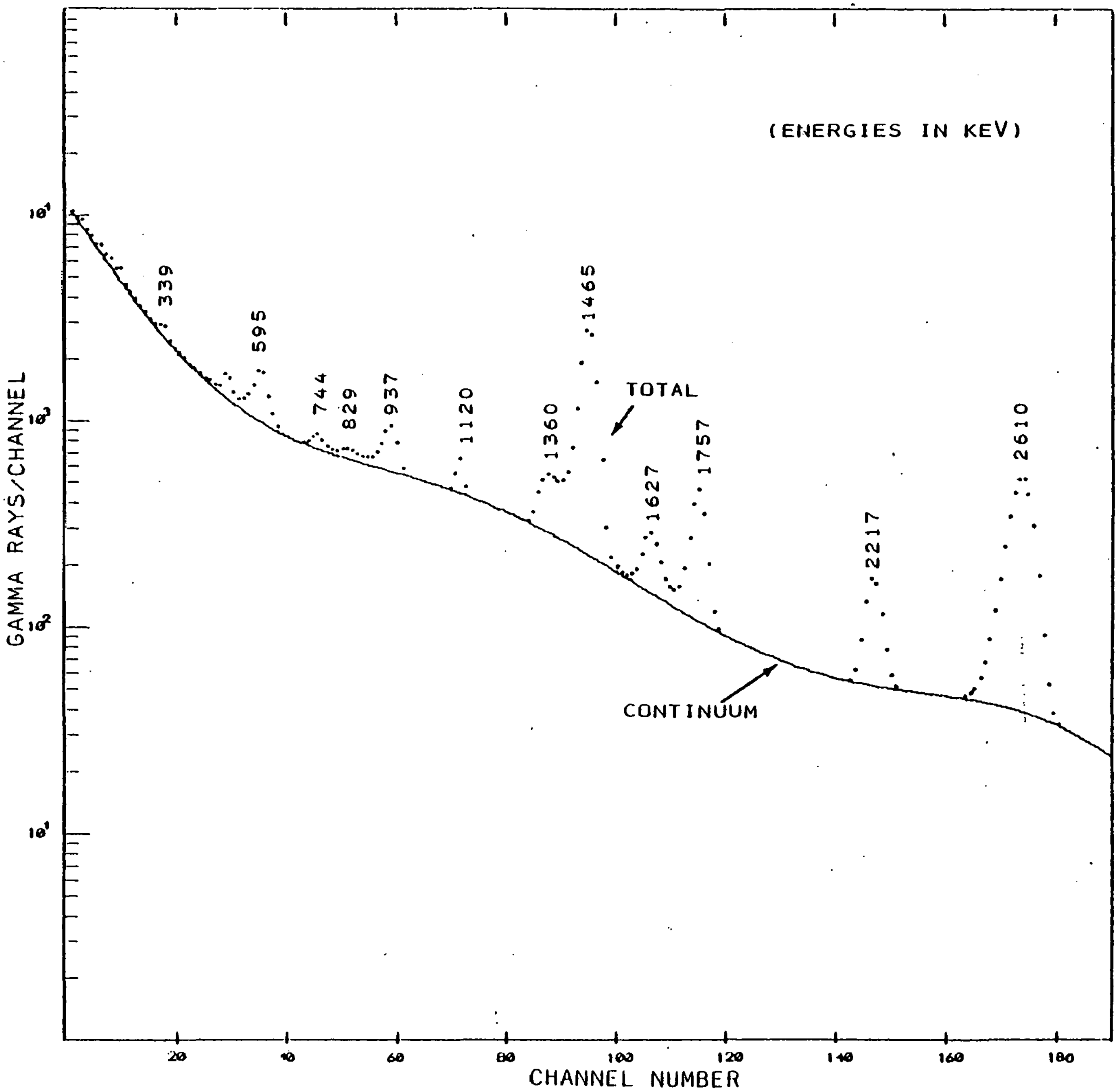

Figure 12. 11½" x 4" Enhanced Data - Equivalent to "10-sec" Airborne Data

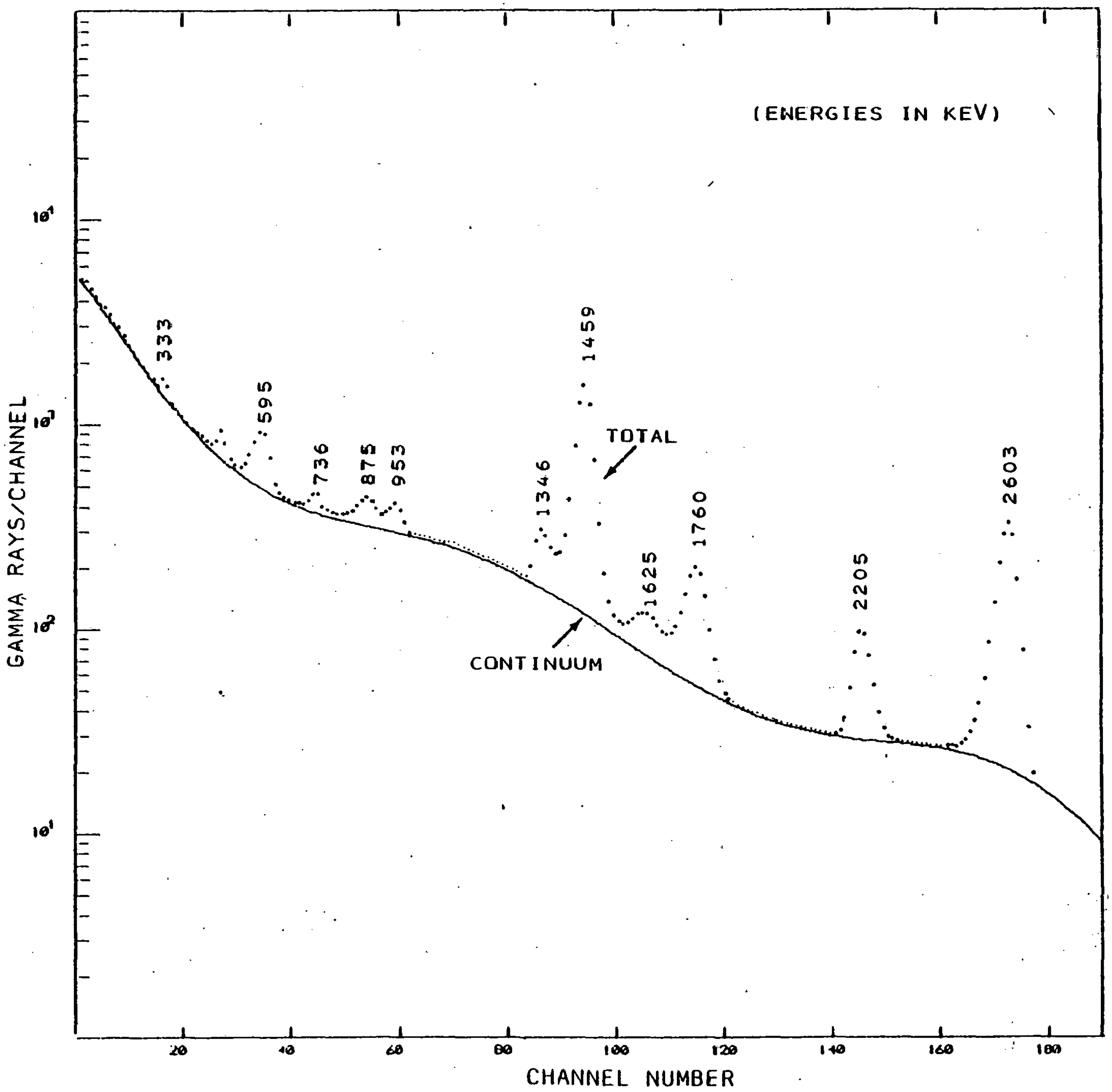

Figure 13. 11½" x 4" Enhanced Data - Equivalent to "5-sec" Airborne Data

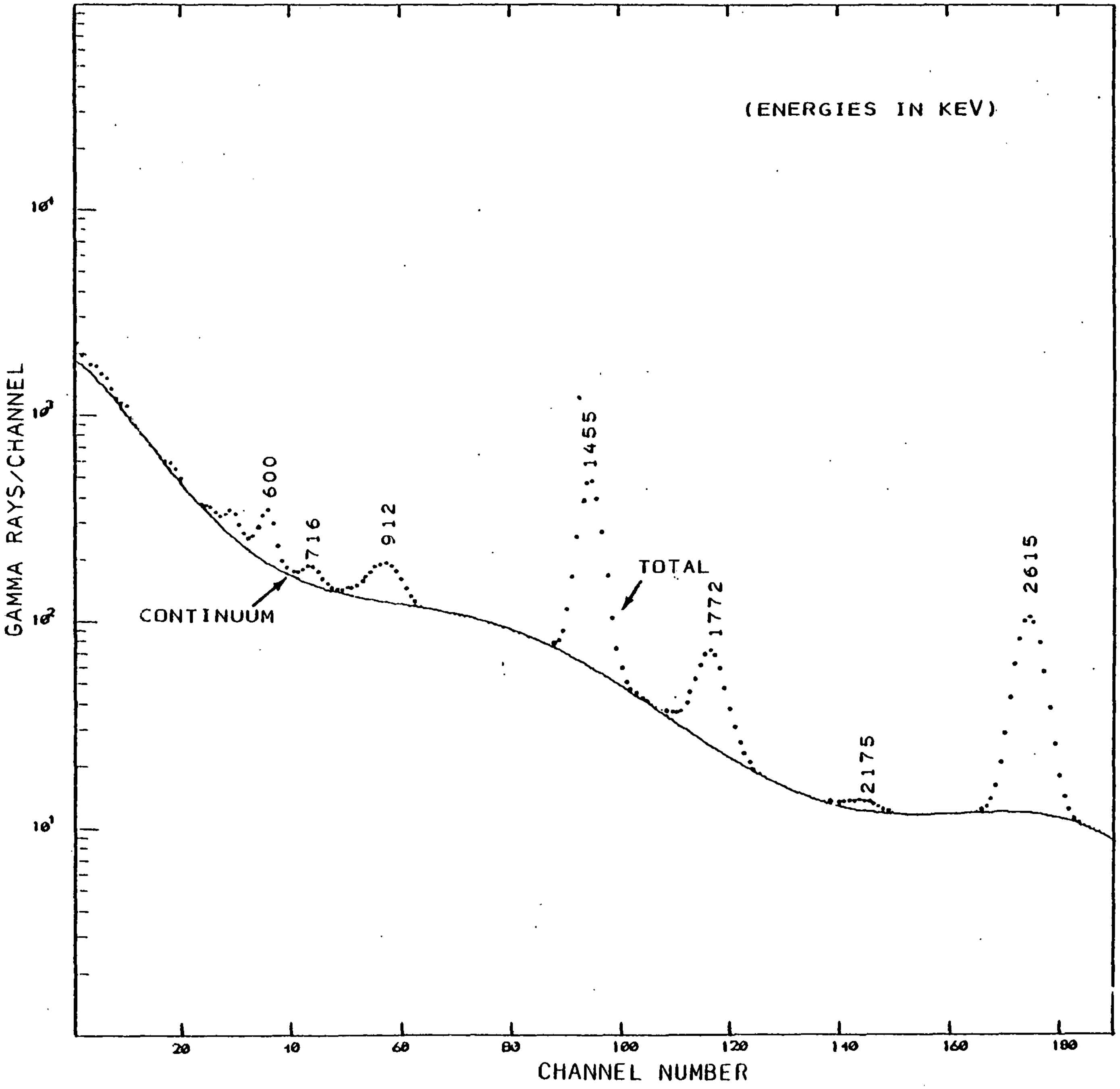

Figure 14. 11½" x 4" Enhanced Data - Equivalent to "2-sec" Airborne Data

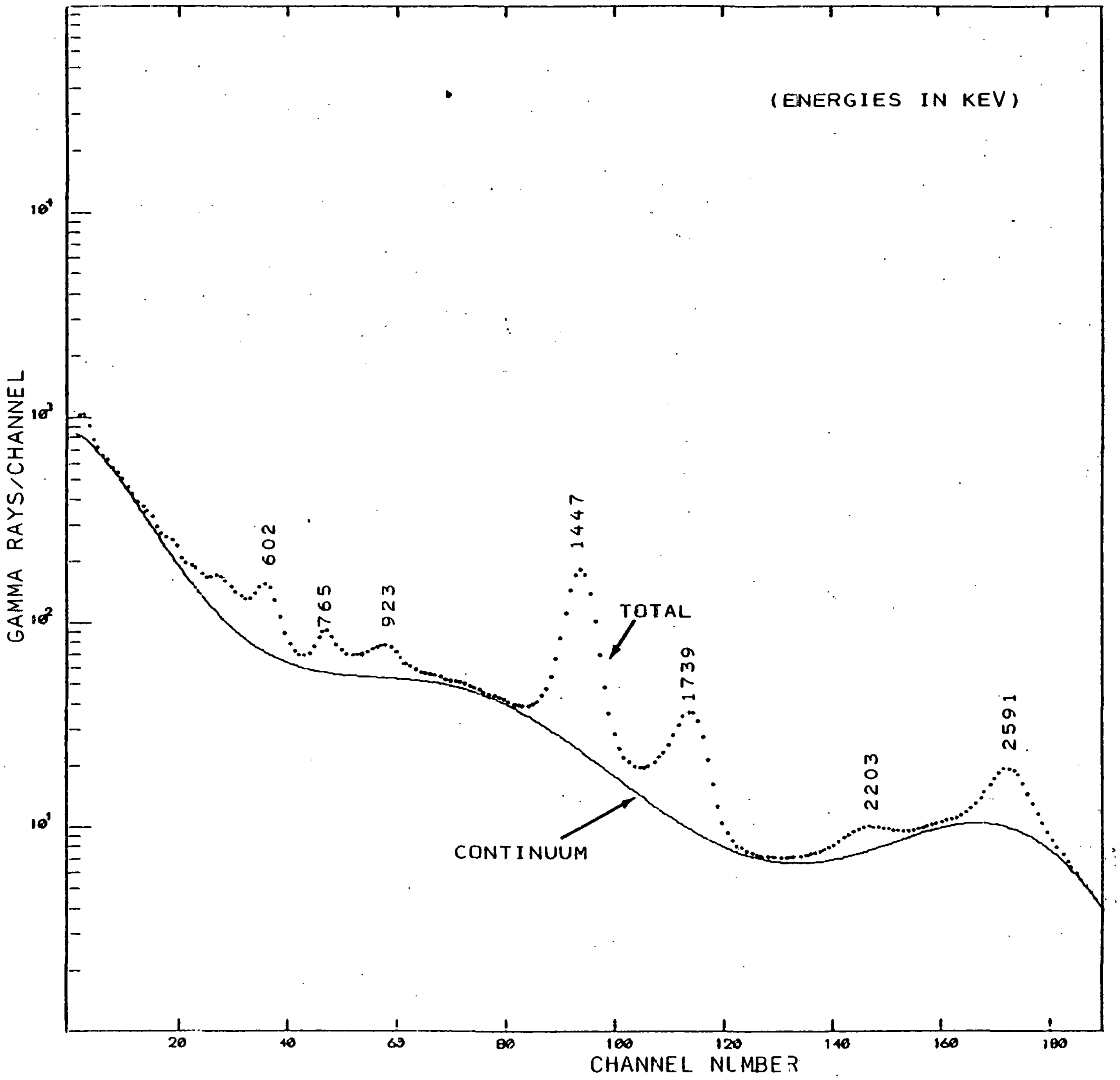

Figure 15. 11½" x 4" Enhanced Data - Equivalent to "1-sec" Airborne Data

Peak areas were extracted for the 0.600, 0.911, 1.461, 1.765, 2.20, and the 2.614 MeV peaks from the processed spectra. The areas are based on the discrete portion of the spectrum as calculated by the code. Figures 16, 17, and 18 show the results of this analysis which gives the ratio of the number of counts in the peak to the total number of counts in the spectrum. The peak area uncertainties were estimated using the expression

$$\mathrm{ERR}(\%) = 100 * \frac{\sqrt{\mathrm{CTS}+2\mathrm{BG}}}{\mathrm{CTS}}$$

where CTS is the number of peak counts (based on the discrete estimate) and BG is the number of counts in the continuum beneath the peak (based on the continuum estimate).

In the case of the 0.600 and 0.911 MeV peaks (Figure 16) fixed windows are used on the discrete spectrum to obtain the areas since these lines are not completely resolved from adjoining peaks. As the counting times become shorter and the peaks become more poorly defined, adjacent lines begin to contribute to the area in the "window," resulting in an apparent increase in area. In Figure 17, the area of the 1.46 MeV line is found to be very consistent even in the "1-sec" spectra. The 1.76 MeV peak is also found to be very consistent, in only three of the ten "1-sec" spectra is the 1.76 MeV peak significantly low. In Figure 18, the area of the 2.20 MeV peak is found to be consistent down through the "5-sec" data, and then is nearly lost in the "1" and "2-sec" spectra. The 2.61 MeV peak is reliably estimated down through the "2-sec" data but, as indicated above, it is underestimated in the "1-sec" spectra.

In addition to establishing the stability of peak areas as a function of counting statistics, we have also considered the stability of peak positions in each of the 29

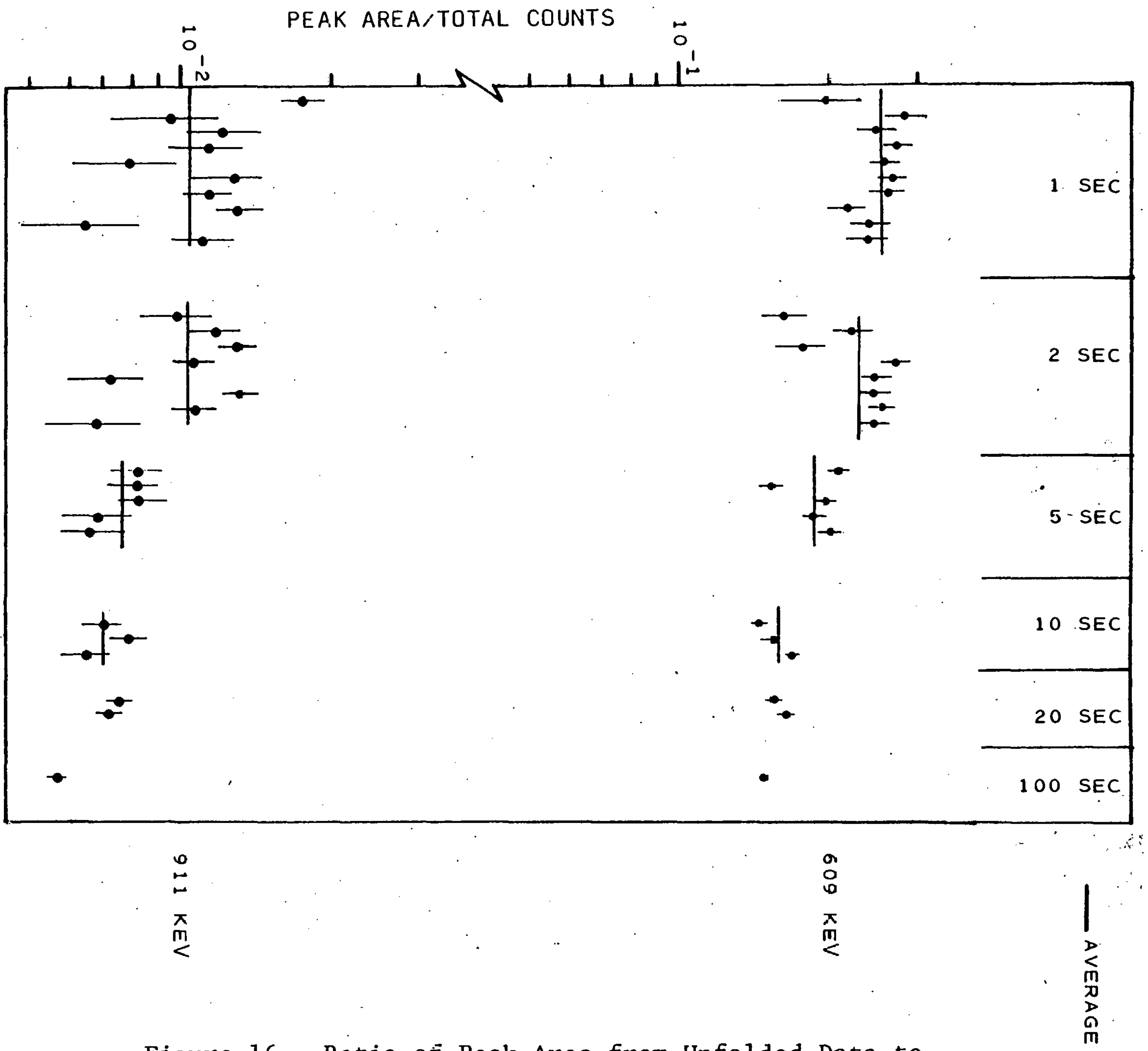

Figure 16. Ratio of Peak Area from Unfolded Data to Total Counts

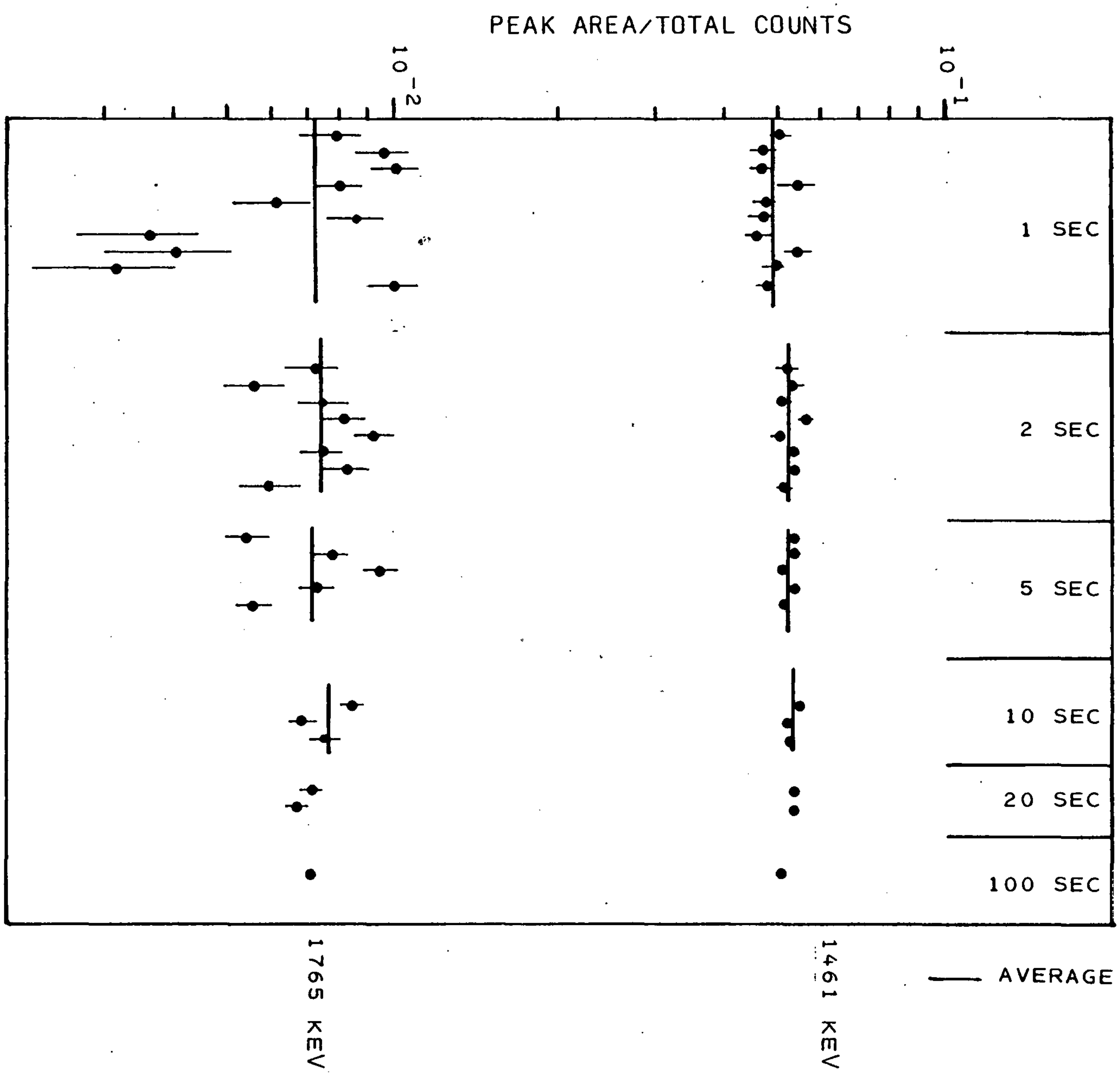

Figure 17. Ratio of Peak Areas from Unfolded Data to Total

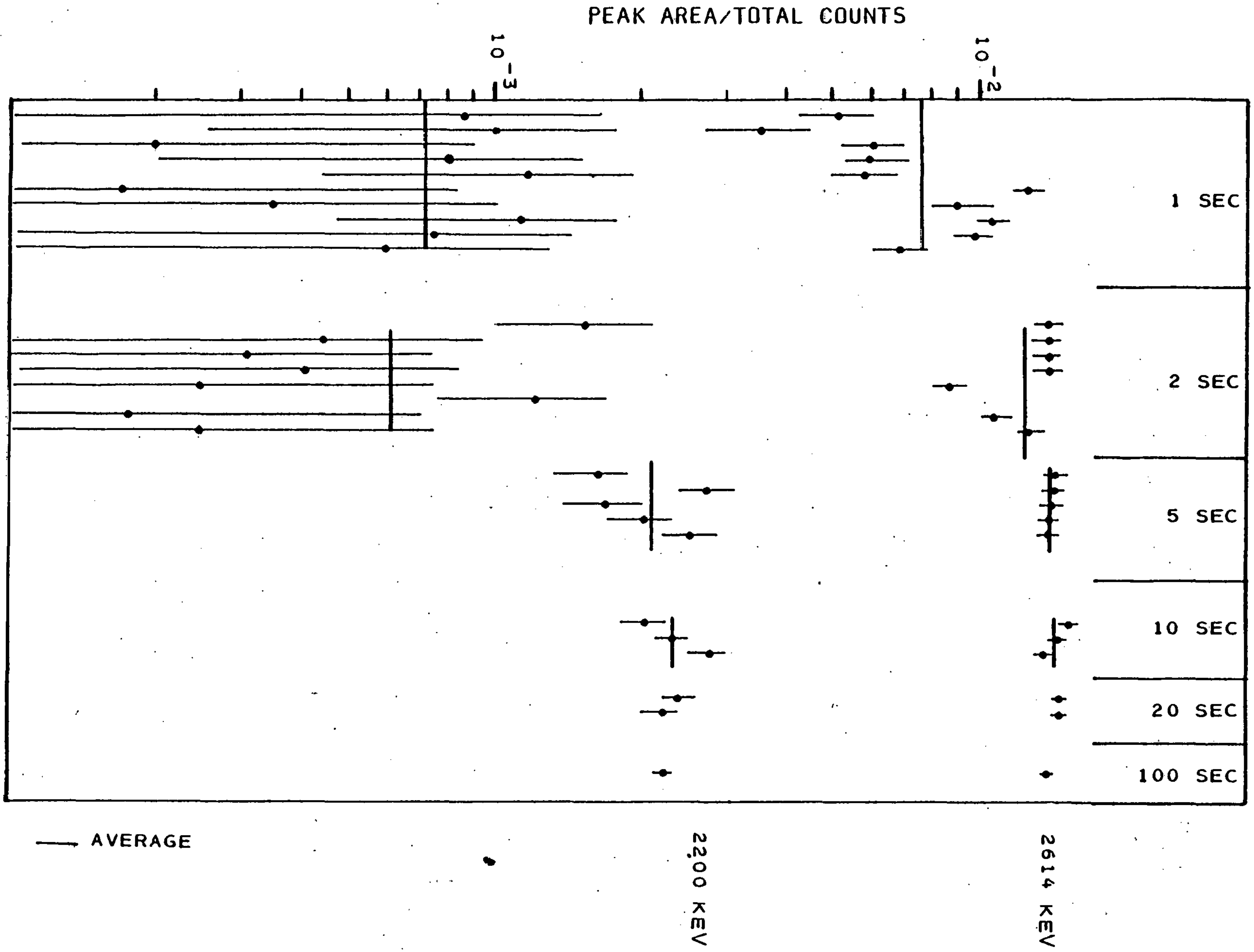

Figure 18. Ratio of Peak Areas from Unfolded Data to Total Counts

processed spectra. Figure 19 shows the position of the peaks in all of the unfolded spectra. The vertical lines give the energies of the gamma-rays observed in the Ge(Li) spectrum, while a series of dots along a given horizontal line give the positions of the peaks in a particular unfolded spectrum. The data are grouped according to the statistical accuracy of the data with the bottom set corresponding to 1 sec of airborne data while the top set corresponds to 100 sec of airborne data. Several points should be made about this graph. First, the unfolded peaks at 2614, 1765, 1460, 900 and 600 keV appear at fairly consistent locations for all of the spectra. Second, the position of the 2.20 MeV peak varies considerably for the lower statistics data and is not observed in some unfolded spectra. Third, some peaks, such as the 1377 and 1620 keV peaks, only show up in the better statistical data. Finally, the positions of the peaks below 600 keV seem to have considerable scatter in the low statistics data although for the good statistics data there appears to be a much more regular pattern of peak positions.

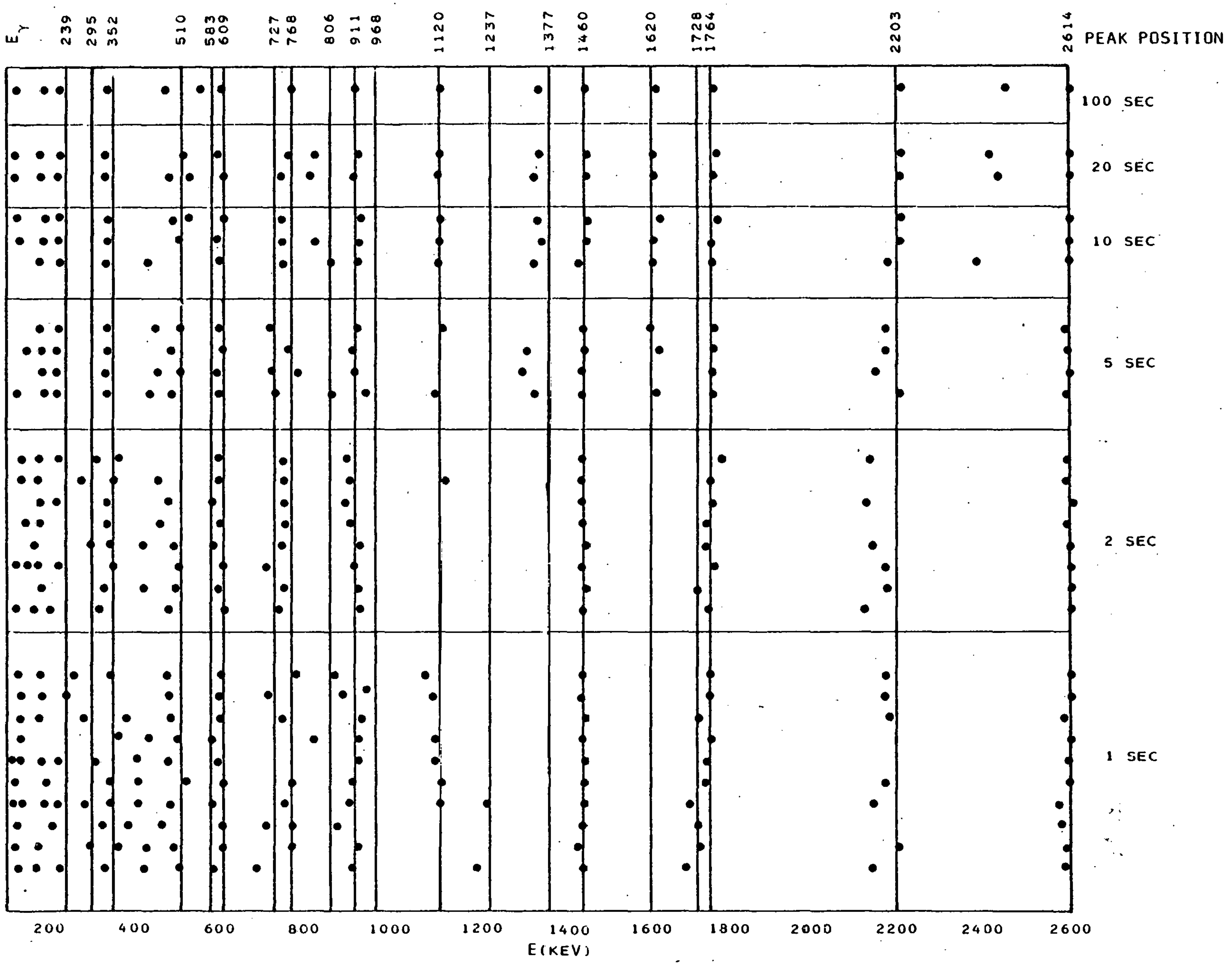

Figure 19. Positions of Peaks in Unfolded Data. The Vertical Lines Indicate the Energies of Gamma Ray Seen in the Ge(Li) Data

5. FUTURE WORK

The present analysis has been carried out using a modified version of MAZE where some of the constraints on how the continuum is changed at each iteration have been relaxed. Unfolding of other gamma-ray spectra indicate that there seems to have been too much relaxation and oscillations in the continuum appear. It is felt that these oscillations are not physical and that either the constraints should be put back into the code in a modified form or that the entire set of continuum constraints be put on a more sound physical basis. It is clear that advances have been made but that some further work in this area is necessary.

THIS PAGE

WAS INTENTIONALLY

LEFT BLANK

NONLINEAR EFFECTS
IN
NaI(Tl) DETECTORS

THIS PAGE
WAS INTENTIONALLY
LEFT BLANK

1. INTRODUCTION

The computer codes MAZNAI and MAZAS both employ calculated response functions for NaI(Tl) detectors. The amount of information these codes can extract from experimental data depends to a considerable extent on how well the calculated response functions reproduce the actual response of NaI(Tl) detectors to monoenergetic gamma rays. The degree to which one must know the response functions depends somewhat on the type of data one is dealing with. For poor statistics data the scatter in the data will dominate the problem and relatively poor response functions can be employed with little loss in information extracted. For good statistics data one must have good response functions. The goal of a number of studies SAI has conducted has been to calculate response functions for various size NaI(Tl) detectors for incorporation into the codes MAZNAI and MAZAS. One of the problems that has been encountered in these studies has been the nonlinear response of NaI(Tl) detectors to gamma radiation.

THIS PAGE
WAS INTENTIONALLY
LEFT BLANK

2. EXPERIMENTAL STUDIES OF NONLINEARITY

The nonlinear response in crystal light output for energy deposited in the crystal is a phenomenon that has been discussed for as long as people have been using NaI crystals for scintillators. R. W. Pringle and S. Standil(1) first reported this nonlinearity. Although they felt that their combination of photomultipliers and amplifiers were introducing the observed discrepancies, they conjectured that the crystal was also contributing to the phenomenon. D. Englekemeir(2) showed that the observed nonlinearity between pulse height or recorded light output and energy deposited in the crystal did not originate with the electronics but came instead from the crystal. Englekemeir did not suggest an exact mechanism for his observations but felt that the nonlinearity could be explained through a variation of fluorescence efficiency of NaI(Tl) with gamma-ray energy.

The study of the nonlinearity has not gone much beyond the 1956 paper by Englekemeir. Heath(3) has compiled much data using a 3" x 3" NaI(Tl) detector, supporting and confirming the earlier work and has constructed an empirical formula for computing the pulse height for a given incident energy (Fig. 1) and for computing the full energy peak energy in terms of the spectrum channel number (ch):

$$E_o = 0.01389 + 0.0103\ \text{ch} - 5.439\ \text{E-06}\ \text{ch}^2 + 8.35\ \text{E-08}\ \text{ch}^3 - 3.701\ \text{E-10}\ \text{ch}^4 + 5.10\ \text{E-13}\ \text{ch}^5,$$

where E_o is given in MeV and one channel corresponds to 10 keV of pulse height.

With the advent of Ge(Li) detectors, the popularity of NaI(Tl) has waned, and there are no recent publications regarding the nonlinearities and their mechanisms.

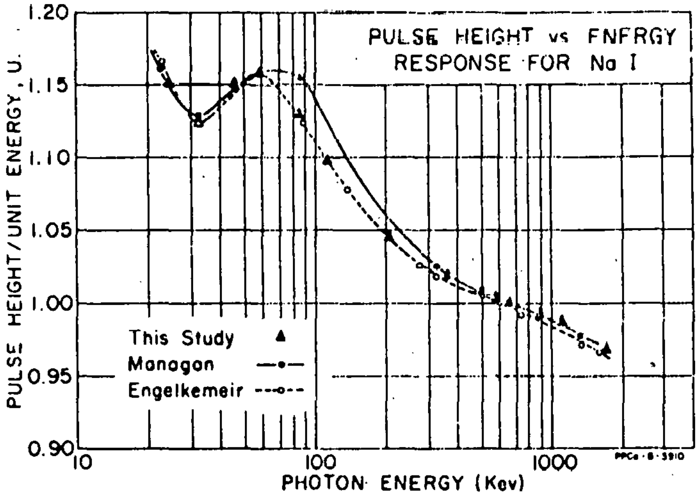

Figure 1. Pulse-height vs. gamma-ray energy response of 3" x 3" NaI detector. To correspond with the energy scale adopted, all data are normalized to unit light output at 0.66162 MeV (Cs^{137}). Ref. 8

3. INCORPORATION OF NONLINEAR EFFECTS INTO MAZNAI

The nonlinearities studied by Englekemeir and by Heath only concern the position of photo peaks in the pulse height spectra. These nonlinearities can easily be incorporated into MAZNAI in the initial setting up of the response function matrix and the final conversion of enhanced peak height to gamma-ray energy. As such, they really do not complicate the problem of response function generation. A more serious problem in terms of response function generation was encountered when measured NaI(Tl) data were compared with the caluclated response functions. Figures 2 and 3 show comparisons of data and the results of ETRAN(5,6) calculated response functions for a 3" x 3" NaI(Tl) detector. Figure 2 shows a comparison of the results for the 661 keV gamma rays from ^{137}Cs. It is seen that the calculated response function in the region of the Compton edge is at too high a pulse height compared to the data. It was speculated that this difference in shape might be caused by nonlinear effects since the pulses in the region of the Compton edge arise mainly from single events in the crystal which deposit fairly large amounts of energy while the photo peak arises primarily at this energy from multiple interactions. Since higher energy photons produce relatively smaller pulse heights than lower energy photons (see Fig. 1), this would tend to lower the pulse heights of the large Compton pulses, giving rise to the shift in pulse height of the Compton edge relative to the photo peak.

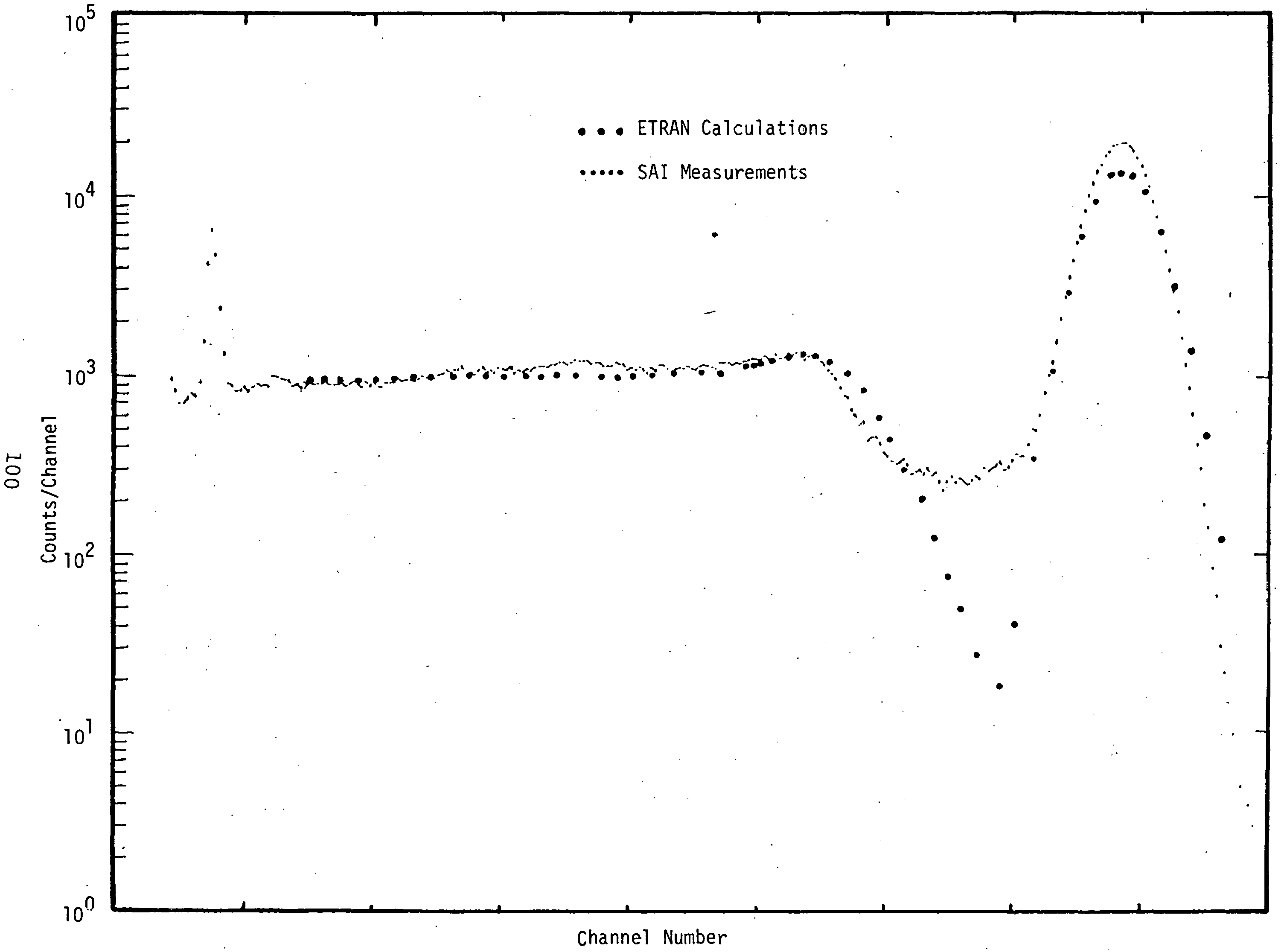

Figure 2. Comparison of Present Experimental Data for 0.662 MeV with ETRAN Calculations.

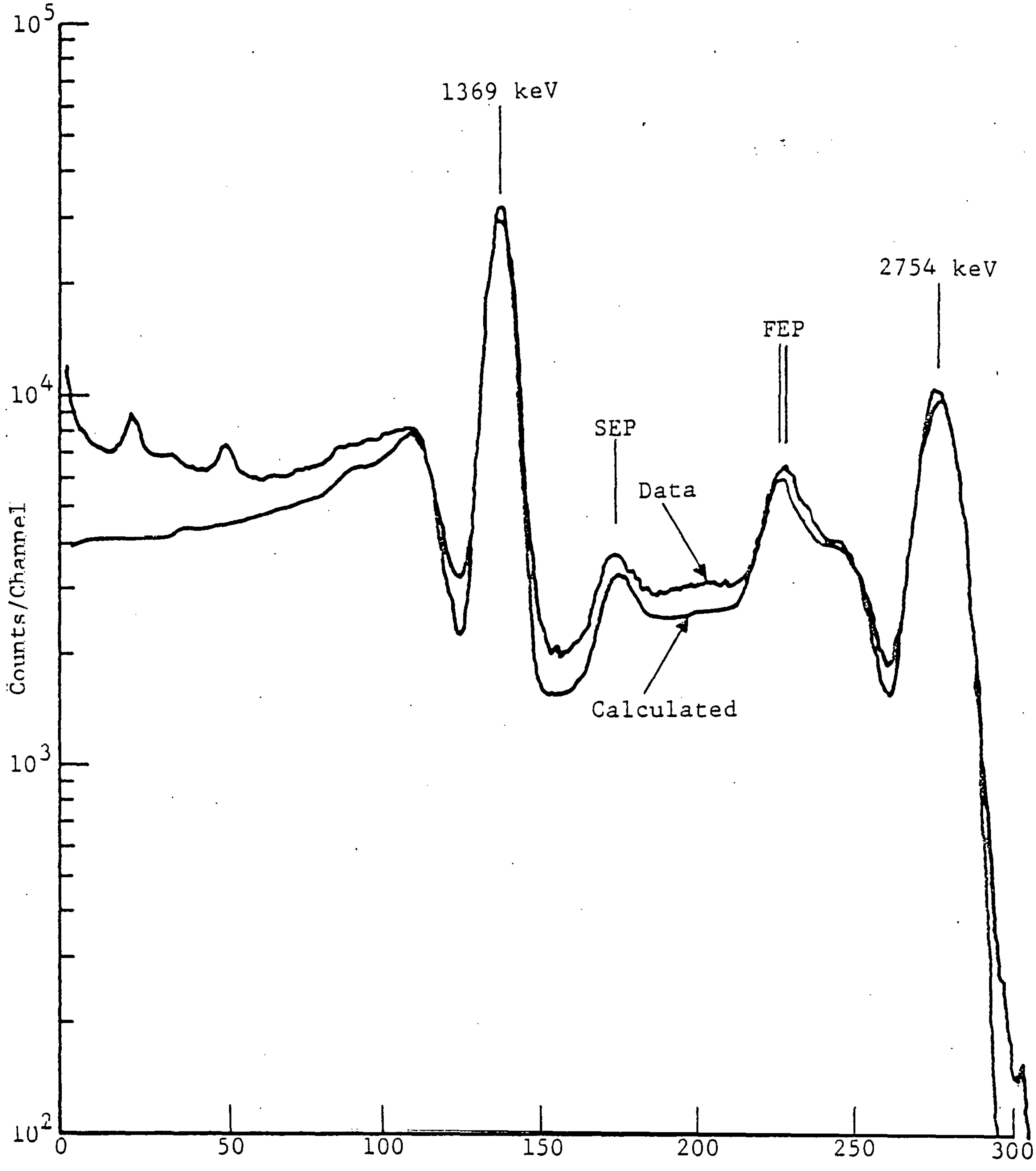

Figure 3. Heath's Na^{24} Data Overlayed with Calculated Response Function - Nonlinearity of First Escape Peak Position.

Another effect was noticed in the high energy data. Figure 3 shows the response function calculated for ^{24}Na using ETRAN and the measured data. It is seen that the position of the single escape peak (labeled FEP in the figure) is not calculated correctly. It was found that this effect was present in the NaI(Tl) data for all single escape peaks. The apparent difference in energy (deduced from a pulse height spectrum) between the single escape peak and the full energy peak was approximately 20 - 30 keV less than the known difference in energy deposited of 511 keV. The difference in apparent energy between the full energy peak and double escape peak was correctly calculated by the code.

It appears obvious that this displacement of the single escape peak is due to nonlinear effects. The exact shape of the calculated Compton distribution depends on the transport code used to calculate the energy deposition. The position of the single escape peak is not nearly so dependent on the details of the transport code and must be due to some physical effect not taken into account in the calculations.

It was speculated that the nonlinear effects noticed in the pulse heights of the full energy peaks could affect different portions of the pulse height spectrum in different ways, since different physical processes give rise to these different features.

The double escape peak, for example, corresponds to the absorption of all of the energy of the electron-positron pair with both of the annihilation photons escaping from the detector. The single escape peak corresponds to the absorption of the electron-positron pair plus the absorption of one of the annihilation photons. The pulse height of the single escape peak should, therefore, fall at the sum of the pulse heights of the double escape peak plus the 0.511 MeV photo peak. Since there is a nonlinear relationship between pulse height and energy, the sum of the pulse heights of the double escape peak plus the pulse height for a 0.511 MeV photon will be larger than that for a single photon of energy equal to E - 0.511 MeV.

To test this hypothesis a simple numerical experiment was carried out using the 3" x 3" NaI energy deposition functions of Berger and Seltzer(6) and the conversion between energy and pulse height given by Heath(4).

These energy deposition functions were converted to a pulse height scale by assuming for the simple Compton part

$$Ph(E_d) = Ph(E_o) - Ph(E_0 - E_d)$$

where E_d is the energy deposited, E_o is the incident energy, and Ph(E) is the pulse height from Heath's conversion from energy to pulse height. For the distribution following pair production the conversion to pulse height was assumed to be given by

$$Ph(E_d) = Ph(E_o - 1.022) + Ph(E_d - E_o + 1.022).$$

Figure 4 compares the energy deposition functions on a pulse height scale obtained using the above prescription for 3 MeV photons and that obtained using Heath's conversion directly. Figure 5 shows another example for 600 keV photons. Several things should be noticed in these graphs. First, for the high energy response the single escape peak is moved upward in pulse height by about 20 keV which is close to that observed experimentally. Second, the peak in the Compton distribution is shifted downward about 20 keV which also is close to that

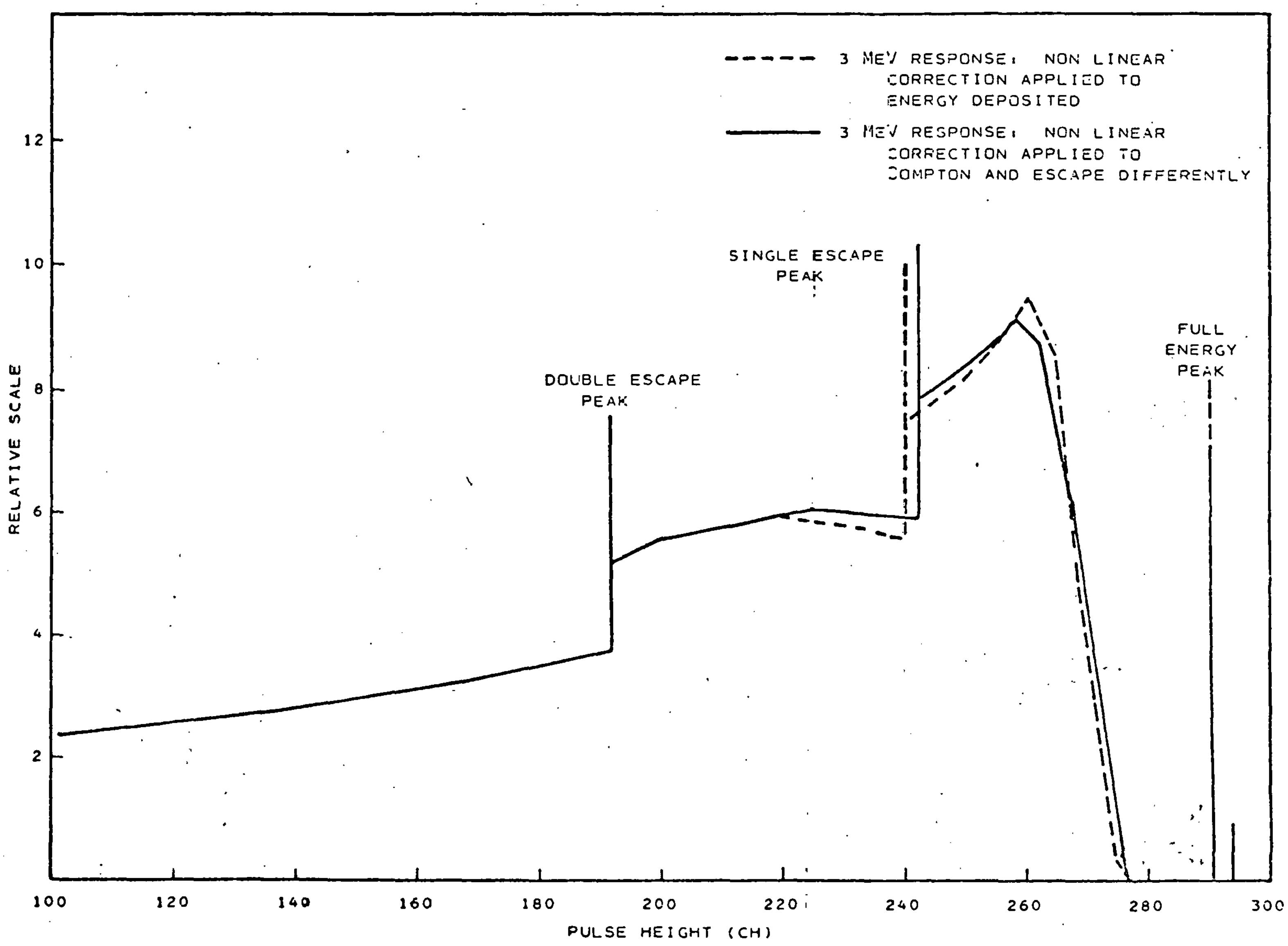

Figure 4. Modified Energy Deposition Spectra.

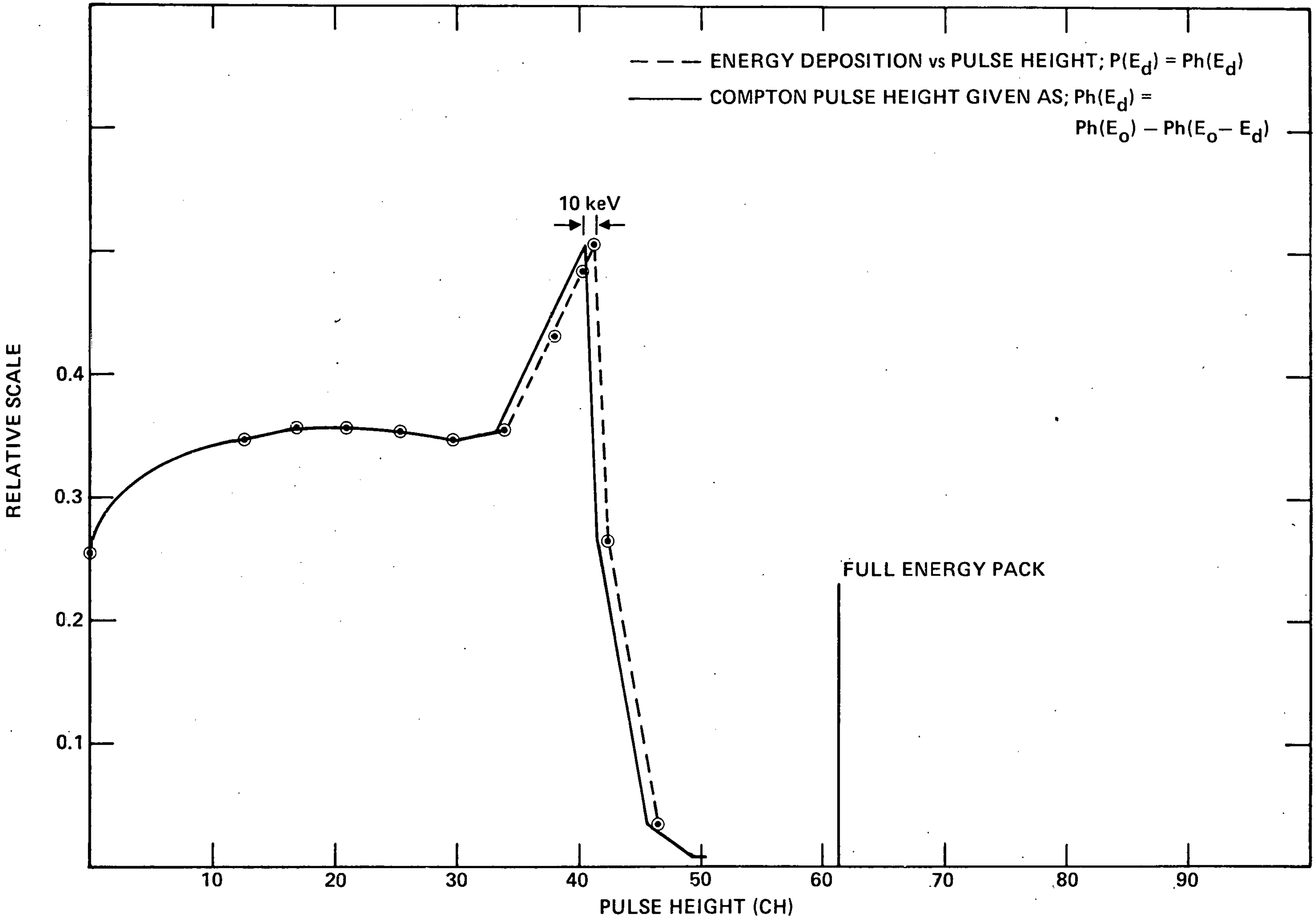

Figure 5. Modified Energy Deposition Spectra (0.6 MeV)

observed experimentally. Third, there is a small peak corresponding to the absorption of both annihilation photons at a pulse height above the full energy peak. This might help explain some of the high energy non-Gaussian behavior seen in photo peaks. For the 600 keV response, the main effect is to shift the Compton distribution to a lower pulse height. As was mentioned, the ETRAN calculations had shown a disagreement between the shape of the calculated and experimental Compton edges. Recent gamma-ray calculations using the GAMRES(7) transport code, which includes the Heath prescription for converting energy to pulse height, have largely eliminated this discrepancy. Figure 6 shows a comparison of the calculated and measured response functions for the 661 keV gamma ray from ^{137}Cs. The shapes of the measured and calculated Compton edges are in good agreement.

The position of the single escape peak is empirically corrected in the MAZNAI subroutines based on the experimental positions of the single escape peaks measured by Heath. Figure 7 shows a comparison of the experimental and parameterized corrections for the position of the single escape peak.

It seems obvious that these nonlinear effects should be studied in more detail. The corrections applied the code MAZNAI are now based on the response of a 3" x 3" NaI detector. It would seem that, if the corrections are due to the differences between the detector response to single and multiple interactions, that the corrections should be related to detector geometry. If this is the case, then the cause of the nonlinearities should be understood so that it can be incorporated directly into the gamma-ray transport codes used to calculate the detector responses.

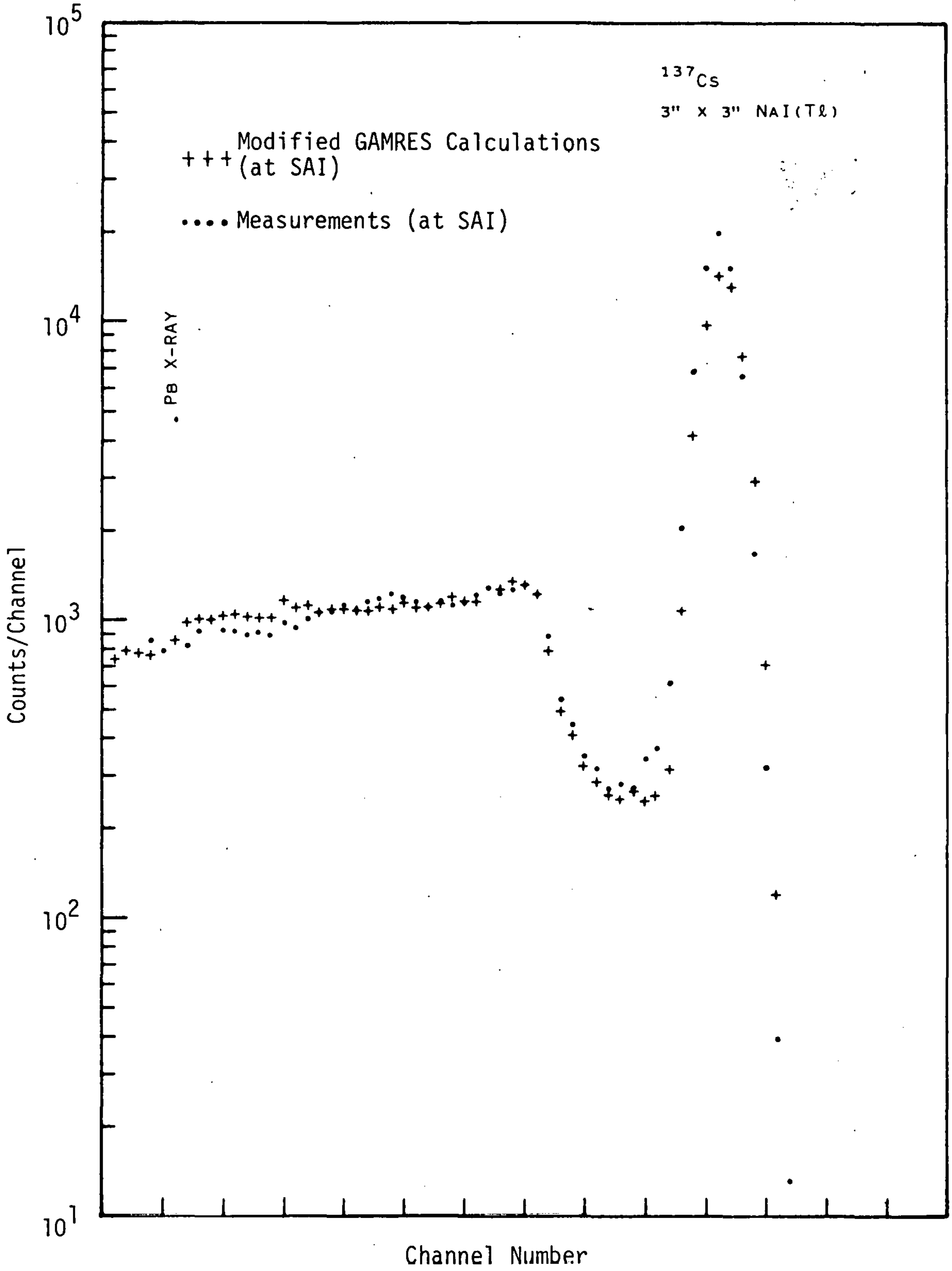

Figure 6. Comparison of Measured and Calculated Response of 3" x 3" NaI.

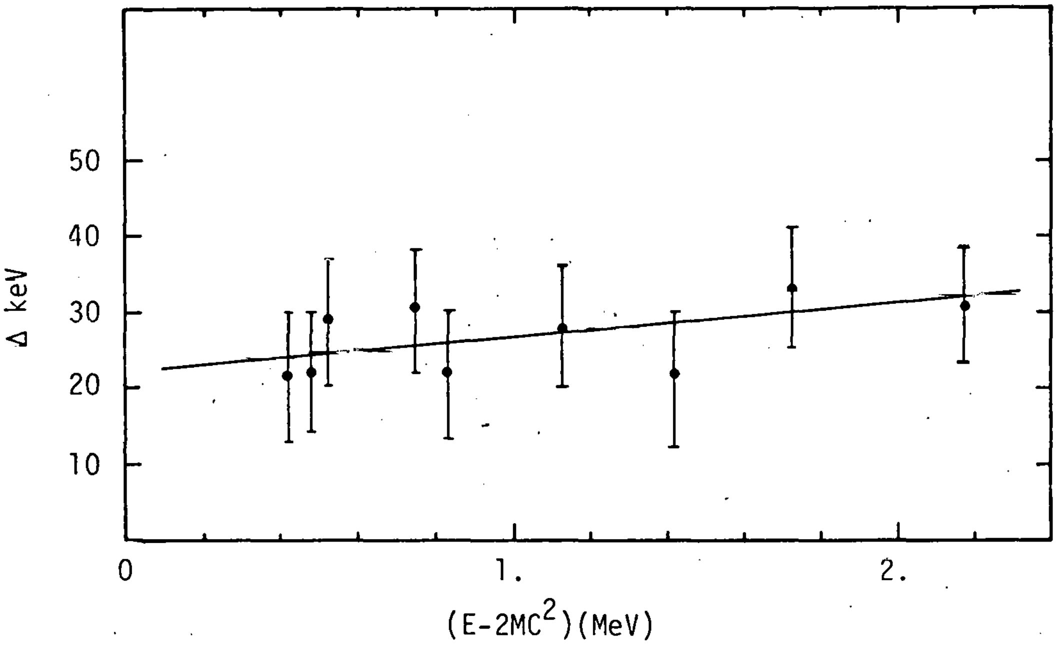

Figure 7. Experimental Differences Between the Spacing of the Full Energy Peak and the Single Escape Peak and the Expected Spacing and Parameterization. Data from Ref. 4.

4. REFERENCES

1. R. W. Pringle and S. Standil, Phys. Rev. 80, p. 762 (1950).
2. D. Englekemeir, Rev. of Sc. Inst. 27, p. 589 (1956).
3. R. L. Heath, Nucl. Inst. and Meth. 47, p. 281-304 (1967).
4. R. L. Heath, "Scintillation Spectrometry, Gamma-Ray Spectrum Catalogue," 2nd Edition IDO-16880-1 and 2, Aug. 1964.
5. M. J. Berger and J. M. Seltzer, "Electron and Photon Transport Programs," NBS Report 9836 and NBA Report 9837.
6. M. J. Berger and J. M. Seltzer, Nucl. Inst. and Meth. 104, p. 317-332 (1972).
7. LASL Progress Report LA-6996-PR (Oct. 1977).